UNIVERSITY OF COPENHAGEN
FACULTY OF SCIENCE

Master Thesis

Study of Elastic Proton-Proton scattering at the LHC

Jon Raunkjær Søndergaard

Supervisor: Jørgen Beck Hansen

Abstract

This thesis is a study of elastic proton-proton scattering measured by the ALFA detectors at the LHC. During a special physics run the protons were collided at a center-of-mass energy of 900 GeV and $\beta^* = 100\,\mathrm{m}$, allowing the ALFA detector to measure the small scattering angles of the colliding protons.

To get a complete understanding of the elastic signal measured in ALFA a Monte Carlo simulation was developed. The analysis of the simulated signal yielded a smearing of the signal in x due to the width of the beam, and a smearing of the signal in y due to the divergence of the beam particles arising from betatron oscillations.

A new maximum log-likelihood fit routine was developed and tested on simulated data. The fit parameters from theory are ρ, the ratio of the real and imaginary part of the forward scattering amplitude, σ_{tot}, the total pp cross-section, and B, the nuclear modulus. On simulated data, with no background, generated with $\rho = 0.1$, $\sigma_{\mathrm{tot}} = 68\,\mathrm{mb}$, and $B = 16\,\mathrm{GeV}^{-2}$, the new fit routine was able to obtain the results of: $\rho = 0.1063 \pm 0.0042$, $\sigma_{\mathrm{tot}} = 67.99 \pm 0.11\,\mathrm{mb}$, and $B = 16.00 \pm 0.17\,\mathrm{GeV}^{-2}$.

Contents

Introduction

The Standard Model is possibly the most fundamental theory there is and it explains a large variety of phenomenons in our every day life. The Standard Model is the basis of the universe describing all fundamental particles and forces apart from gravity. This has led to particle physics being one of the main research topics of the physics world.

The Standard Model may seem complete by the discovery of the Higgs boson in 2012, from the experiments conducted at the Large Hadron Collider (LHC) at the European Organization for Nuclear Research (CERN), but this is far from true. Even though the Higgs boson explains how particles have mass, and the other gauge bosons describe the fundamental forces of electromagnetism and the strong and weak force, the Standard Model still has no explanation of why there is much more matter than anti-matter, and it also lack a description of dark matter. So it is safe to say that there is still some unanswered questions concerning the Standard Model. Some of the questions are researched by looking at the most simple form of interaction between two particles, namely elastic scattering.

Elastic scattering is studied by the Absolute Luminosity For ATLAS (ALFA) experiment, which is a sub-detector of ATLAS, the largest detector in the LHC complex. ALFA measures elastically scattered protons interacting at very high energies and scattering at very small angles. Elastic scattering is mediated by the electromagnetic force and the strong force. In elastic scattering no quantum numbers are exchanged, only energy is exchanged between the two particles, making one particle leave the interaction point at the same angle as the other due to energy conservation.

Although it is the simplest form of an interaction, elastic scattering still offers interesting insights worth studying. Just now there has been a discovery of a particle called the Odderon, proposed in 1973, as a result of research

of elastic scattered protons.

The study of elastic scattering in ALFA is important for estimating the probability of two protons interacting, in the LHC, called the pp total cross-section, and the parameter ρ which is the ratio between the real and imaginary part of the forward scattering amplitude. ALFA is furthermore designed to provide a measure of the luminosity, the total number of collisions in the LHC, which are also crucial for many other analyses concerning particle collisions at the LHC.

This thesis focuses on the 900 GeV elastics physics run for the ALFA experiment. First of there will be a description of the theory relevant for elastic scattering of protons at 900 GeV. Then follows a brief description of the LHC and ATLAS together with a thorough presentation of the experimental setup and data taking for ALFA. The last part of the thesis covers the data analysis, where the simulation and study of the elastic signal is the main focus.

1 Theory

This section provides a description of the theory of particle physics studied in the experiment of elastic proton-proton collisions at 900 GeV carried out by the ALFA collaboration. It will contain an introduction to the Standard Model and an explanation of the forces related to elastic proton-proton collisions, namely the electromagnetic force and the strong nuclear force. This is followed by a description of the kinematics of elastic scattering and in the end a theoretical model for the elastic cross section is presented.

1.1 The Standard Model

The Standard Model of particle physics describes the elementary particles and the fundamental forces of nature, which make up our entire universe. The forces of the Standard Model describe the interactions between particles and thereby lay the foundation for all fundamental phenomenons such as matter, atoms, electricity, light etc. [1].

The Standard Model is presented in fig. 1 and is divided into matter and force carriers. The three fundamental forces of the Standard Model are mediated by the gauge bosons, depicted in red on fig. 1. All gauge bosons have spin of $S = 1$. The strong force is mediated by eight gluons, which are all massless. The charge of the strong force is called colour, hence all particles carrying colour charge is subject to the strong force. Gluons carry colour charge themselves and this has some interesting consequences, such as gluon self-interaction, which enables elastic scattering through the strong force that is described later on. The electromagnetic force is mediated by the photon. The photon is massless and has no charge, and can therefore not interact with itself. The weak force is mediated by the neutral Z-boson and the electrically charged $W^{+/-}$-boson and both the Z-boson and the $W^{+/-}$-boson are massive. There are two charges associated with the weak force called isospin and hypercharge [1].

There are three generations of matter and they all consist of two quarks

and two leptons all with spin $S = 1/2$. All quarks and leptons have an associated anti-particle, usually indicated with a bar, e.g. a quark and anti-quark is denoted by q and $\bar{q}$ respectively. The quarks are all electrically charged, massive, and carry colour charge. They are therefore subject to all the fundamental forces of the Standard Model. The quarks come in doublets, up and down quarks from the first generation, charm and strange for the second generation, and top and bottom for the third generation. The up, charm, and top have electrical charge of $2/3e$, where e is the elementary charge of the electron and the down, strange, and bottom have charge of $-1/3e$. Their mass hierarchy is $m_{up} < m_{charm} < m_{top}$ and $m_{down} < m_{strange} < m_{bottom}$, thus rising as we go to higher generations [1].

The charged leptons, the electron, the muon, and the tau, are each associated with a nearly massless and electrically neutral neutrino. The three charged leptons and their corresponding neutrinos makes up the three lepton doublets. The electron, the muon, and the tau all have electric charge of -1. The mass hierarchy of the charged leptons is $m_e < m_\mu < m_\tau$, whereas the absolute mass and mass hierarchy for the neutrinos are not determined yet. The only way to distinguish between the three generations are by mass [1].

All matter is made up from particles of the first generation, as this is the only stable matter. All atoms of the periodic table are made from the up and down quarks, which make up the protons and neutrons in the nucleus, and electrons which orbit the nucleus [1].

The proton and neutron are called baryons as they consist of three quarks. The proton consist of two up and one down quark, making it charged by $1e$, and the neutron consist of two down and one up quark making it neutral. Particles consisting of multiple quarks held together by gluons and the strong force are called hadrons [1].

1.2 Quantum Electrodynamics

Quantum electrodynamics (QED) is the theory of the electromagnetic interaction between particles. Particles subject to the electromagnetic interaction

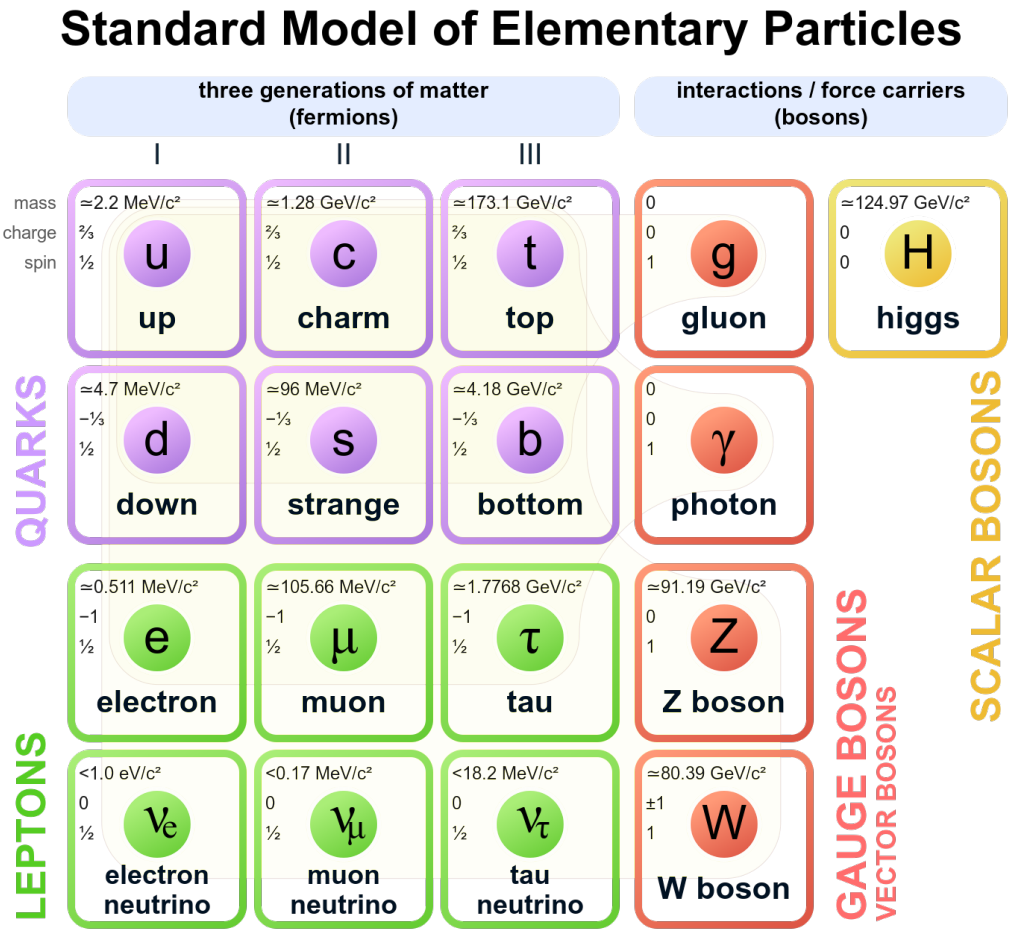

Figure 1: The Standard Model of particle physics. [2]

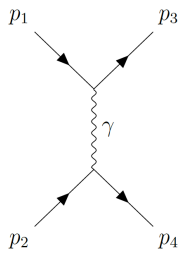

Figure 2: QED proton-proton interaction.

are electrically charged particles, such as the electrons, quarks, or even protons seen as whole particles. The underlying symmetry of QED is U(1). The U(1) symmetry group has one generator, which corresponds to a massless gauge boson, e.i. the photon. Every interaction in QED corresponds to an exchange of a virtual photon between the charged particles, an example of this is seen in fig. 2 [1].

1.3 Quantum Chromodynamics

Quantum Chromodynamics (QCD) is the theory of the strong nuclear force. The symmetry of QCD is the SU(3) symmetry group, as the strong force is invariant under SU(3) local phase transformations. This gives rise to eight generators of the SU(3) symmetry group. These eight generators gives rise to eight new gauge fields called gluons. The charge of the strong force is called colour charge and it is in the transformation of these colour charges the local gauge invariance of the strong force lies. The SU(3) group is non-Abelian, which means that the generators of the SU(3) do not commute. This gives rise to a self-interacting term in the Dirac-equation for the strong force, which means that the gluons must carry colour charge. The gauge transformation does not give rise to a mass term, thus the gluons are left massless. The interactions of QCD is shown in fig. 3, where the self-interaction vertices is shown in the middle and to the right. [1].

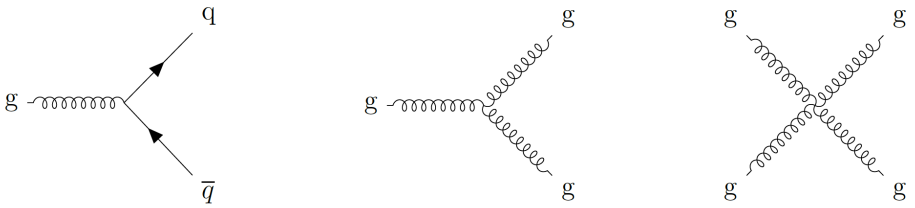

Figure 3: QCD vertices.

Particles carrying color charge have never been observed as free particles. This is due to colour confinement that states that there are no free particles with colour charge. Quarks and gluons are therefore always bound with other quarks, or gluons, in colourless states [1].

1.3.1 The Running of coupling constants

A coupling constant is a measure of the strength of an interaction. However, the coupling constants of QED (α) and QCD, α_s vary as functions of energy transfer, q, and are thereby not constant.

The running of the QED coupling constant is given by:

$$\alpha(q^2) = \frac{\alpha(\mu^2)}{1 - \alpha(\mu^2)\frac{1}{3\pi}\ln\left(\frac{q^2}{\mu^2}\right)} \tag{1}$$

Where $\alpha(\mu^2)$ is a known value of α at some given energy transfer μ. The running of the constants are calculated by renormalising with higher order Feynmann loop diagrams [1]. The running of the coupling constant can be explained by the screening of charge by virtual particles of opposite charge. This phenomenon is called vacuum polarization, and it happens as charged particles are surrounded by virtual photons and short lived virtual electron-positron pairs. A charged particle attracts the virtual particles of opposite charge. As a result the charge of the particle is screened by the virtual particles and the effective charge becomes smaller at larger distances, making the QED coupling stronger at small distances, i.e. for large energy transfers [3]. Measurements of α reveals $\alpha(q^2 \approx 0) \approx 1/137$, and $\alpha(q^2 = m_Z^2) \approx 1/129$,

which verifies the running of the QED coupling constant [4]. As the coupling constant only depends weakly on the center-of-mass energy, and ALFA are looking at elastic events with very small energy transfers, the coupling constant is small and perturbative QED is applicable.

The running of the QCD coupling constant, α_s, is given by:

$$\alpha_s(q^2) = \frac{\alpha_s(\mu^2)}{1 + B\alpha_s(\mu^2)\frac{1}{3\pi}\ln\left(\frac{q^2}{\mu^2}\right)} \quad \text{, with} \quad B = \frac{11N_C - 2N_f}{12\pi} \tag{2}$$

With $N_C = 3$ being the number of colours and $N_f = 6$ the number of quarks. The expression differs from the one for QED as the gluons can self-interact, thus given rise to a larger number of higher order Feynman loop diagrams for QCD [1]. As B is positive, α_s grows as the energy transfer becomes small. This can be explained by anti-screening. A colour charged test particle will be surrounded by virtual quarks and gluons all carrying colour charge. The virtual quarks and gluons draws the color charge away from the test particle, making the test color charge weaker, by spreading the colour charge out onto a larger volume. Thus moving further away one will see more colour charge making the strong coupling stronger at larger distances, e.i. for low energy transfers [3]. Measurements of α_s reveals $\alpha_s(q \sim 1\,\text{GeV}) \sim 1$ and $\alpha_s(q^2 = m_Z^2) \approx 0.1$ [1].

In the low energy regime, of 900 GeV, one cannot use perturbative QCD as the coupling constant becomes to large to treat it as a perturbation.

1.3.2 Regge Theory

The ALFA experiment measures very small scattering angles and therefore very small energy transfers, this means that ALFA measures elastic events in the non-perturbative regime of QCD [5].

Regge theory is a non-perturbative theory for QCD. When quarks are bound in hadronic states they are colourless, due to colour confinement, but they are allowed to have spin and angular momentum, which combined is

denoted by $J = L + S$. The total spin and mass are linearly related in what is called Regge trajectories. The linear relation between spin and mass is given by:

$$J = \alpha_0 + \alpha' M^2(J) \tag{3}$$

With M being the mass. Each allowed combination of quarks into hadrons has this linear relation between mass and spin. For each integer or half integer of spin J, depending on the initial value of S, there is another hadron [6].

These particles are called Reggeons, and can exist as propagating particles when two protons interact through the strong force as they are colourless.

1.3.2.1 Reggeons as propagators

A particle interaction is governed by the strength of the coupling in the vertices and the energy transfer. For the strong force the coupling is $\alpha_s(q)$. Using Reggeons as propagators we are able to determine the transition resonances by finding the Regge poles, on the Regge trajectories. The Regge trajectories has a Regge pole for each integer and half integer spin. These poles corresponds to Reggeons. By finding the Regge poles the resonances can be calculated by the linear relation of the spin of the Regge poles to the mass of the Reggeons. The total transition amplitude for two proton interacting elastically through the strong force is given by adding the contributions from all possible Regge poles together [7]. By having these colourless Reggeons we are able to describe the interaction between protons due to the strong force, as seen in fig. 4.

However, at large energies the total cross section starts to increase. This is assured by the introduction of the so called Pomeron trajectory, named after Pomeranchuk. He proved that at large energies the cross sections of proton-proton and proton-antiproton becomes equal. A solution to this behavior are the so called glue balls. A collection of gluons carrying the quantum numbers of vacuum and being colourless [8]. Research have shown that Pomerons are not sufficient to describe the pp cross section, thus a colorless glue ball of

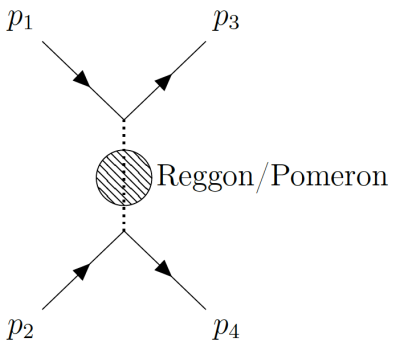

Figure 4: QCD proton-proton interaction.

odd charge parity called the Odderon was introduced to make up for the sufficiency of the existing theories. The existence of the Odderon was first predicted in 1973 and measurements by the TOTEM and D0 collaboration and have just proven the existence of the Odderon in 2020 [9]. The Reggeons, Pomerons, and Odderons are the possible propagators of elastic scattering mediated by the strong force, and from these interactions the elastic nuclear scattering amplitude is calculated. However, for this thesis the nuclear interaction amplitude is approximated by a phenomenological model. This is presented later in section 1.4.2.

1.4 Elastic Scattering

Elastic scattering is characterized by no quantum number being exchanged between the interacting particles and small energy transfers. As the energy transfer is small we are in the non-perturbative regime of QCD as explained in section 1.3.1, thus we turn to phenomenological models to describe the nuclear scattering amplitude. Whereas perturbative QED is sufficient to describe the QED processes of elastic pp scattering.

This section includes a description of the kinematics used in elastic proton-proton scattering with small momentum transfers and a thorough description of the elastic scattering amplitude, which includes a Coulomb scattering amplitude, a nuclear scattering amplitude, and an interference term.

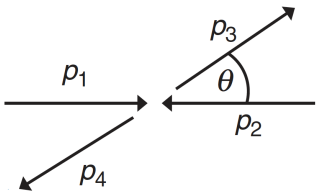

Figure 5: Two protons scattering with angle θ

1.4.1 Kinematics

For elastic proton-proton scattering at the LHC, the two initial particles are known to have the same energy and momentum in opposite directions. A small drawing of pp scattering is shown in fig. 5. Here proton 1 and 2 scatters into proton 3 and 4. The scattering angle is the same for proton 3 and 4 due to momentum conservation.

The center-of-mass energy squared is given by the Mandelstam variable s which is defined as $s = (p_1 + p_2)^2$, with p_1 and p_2 as the four momentum of the incoming protons [1]. As the incoming protons has equal but opposite momentum s can be written as

$$s = (p_1 + p_2)^2 = (E_1 + E_2)^2 - (\mathbf{p_1} + \mathbf{p_2})^2 = E_1^2 + E_2^2 + 2E_1E_2 \tag{4}$$

As $\mathbf{p_1} = -\mathbf{p_2}$ the last term is 0, and as $E_1 = E_2$, s can be written in terms of the proton mass, m_p, and the momentum, $p = |\mathbf{p_1}|$.

$$s = 4(m_p^2 + p^2) \tag{5}$$

The exchange of momentum between the incoming proton is given by the Mandelstam variable $t = (p_1 - p_3)^2 = (p_2 - p_4)^2$. This can be written as

$$t = (p_1 - p_3)^2 = (E_1 - E_3)^2 - (\mathbf{p_1} - \mathbf{p_3})^2 = \tag{6}$$

$$= E_1^2 + E_3^2 - 2E_1E_3 - \mathbf{p_1}^2 - \mathbf{p_3}^2 + 2\mathbf{p_1}\mathbf{p_3} \tag{7}$$

For elastic scattering $\mathbf{p_1}^2 = \mathbf{p_3}^2 = p^2$, thus we have

$$t = 2m_p^2 + 2p^2 - 2(m_p^2 + p^2) - 2p^2 + 2p^2\cos\theta \tag{8}$$

$$= -2p^2 + 2p^2\cos\theta \tag{9}$$

As we are dealing with very small angles this can be approximated to

$$t = -2p^2 + 2p^2\cos\theta \simeq -2p^2 + 2p^2\left(1 - \frac{\theta^2}{2}\right) \Leftrightarrow \tag{10}$$

$$t = -(p\theta)^2 \tag{11}$$

The ALFA experiment is designed on the basis of the relation between momentum transfer t and scattering angle, θ. This relation is therefore of great importance.

1.4.2 Elastic Cross section

Since protons are electrically charged and they consist of quarks they interact through the electromagnetic force and the strong nuclear force. Because of this the elastic cross-section for proton-proton scattering is comprised of a Coulomb term, due to Coulomb interactions, a nuclear interaction term, due to strong force interactions, and an interference term of the two forces [10].

The total elastic differential cross section is given by

$$\frac{d\sigma}{dt} = |F_C e^{i\alpha\phi(t)} + F_N|^2 \tag{12}$$

With F_C and F_N being the Coulomb and Nuclear term respectively, and $\phi(t)$ being the interference term between the two types of interactions.

Coulomb Interaction Amplitude

The Coulomb interaction term arises from the electromagnetic interactions between the protons. For small energy transfers the QED coupling constant is

small and perturbation theory is therefore sufficient to describe the Coulomb interaction cf. section 1.3.1. The dominating Feynman diagram for the Coulomb interaction is shown in fig. 2. For small energy transfers the virtual photon has a large wavelength and thus sees the proton as a whole charge [1]. The form factor of the proton is therefore needed. A simple form factor is the dipole parametrization given as

$$G(t) = \left(\frac{\Lambda}{\Lambda + |t|}\right)^2 \tag{13}$$

with $\Lambda = 0.71\,\mathrm{GeV}^2$ [11]. Another slightly more complicated model is the double dipole model given by

$$G_{\text{double dipole}}(t) = a_0 \left(\frac{\Lambda_0}{\Lambda_0 + |t|}\right)^2 + (1 - a_0)\left(\frac{\Lambda_1}{\Lambda_1 + |t|}\right)^2 \tag{14}$$

with $a_0 = 0.976$, $\Lambda_0 = 0.66$, and $\Lambda_1 = 0.60$ [11]. For small scattering angles the forward scattering amplitude for the Coulomb scattering is given by

$$F_C = \frac{-2\sqrt{\pi}\alpha G^2(t)}{|t|} \tag{15}$$

Where $G(t)$ can be any form factor dependent on t [10].

Nuclear Interaction Amplitude

The nuclear interaction comes from strong force interactions between the protons described by QCD. Because of the running of constants perturbative QCD cannot be used and therefore a phenomenological model determined from experiment which is sufficient for small values of t, is used instead [10]. This is given by

$$\frac{d\sigma_N}{dt} = \left.\frac{d\sigma_N}{dt}\right|_{t=0} e^{-\Omega(t)} \tag{16}$$

The optical theorem, derived in appendix B, describes the relation between the forward scattering amplitude and the total cross section given by

$$\sigma_{\rm tot} = 4\sqrt{\pi}{\rm Im}(F(t=0)) \tag{17}$$

With the phenomenological model we now write

$$\frac{d\sigma_N}{dt} = \left.\frac{d\sigma_N}{dt}\right|_{t=0} e^{-\Omega(t)} = |F(s,t=0)|^2 e^{-\Omega(t)} \tag{18}$$

$$= |{\rm Re}(F_N(t=0)) + i{\rm Im}(F_N(t=0))|^2 e^{-\Omega(t)} \tag{19}$$

$$= \left|\left(\frac{{\rm Re}(F_N(t=0))}{{\rm Im}(F_N(t=0))} + i\right){\rm Im}(F_N(t=0))\right|^2 e^{-\Omega(t)} \tag{20}$$

Now inserting the optical theorem and defining $\rho = {\rm Re}(F_N(t=0))/{\rm Im}(F_N(t=0))$ we arrive at

$$\frac{d\sigma_N}{dt} = \left|(\rho+i)\frac{\sigma_{\rm tot}}{4\sqrt{\pi}}e^{-\Omega(t)/2}\right|^2 \tag{21}$$

The nuclear modulus $\Omega(t)$ can be expressed in different forms, for instance three types of polynomials

$$\Omega(t) = \sum_{n=1}^{N_B} B_n t \tag{22}$$

with $N_B = 1, 2, 3$ [12]. The nuclear modulus can also be describes as in [13] where it is given by

$$\Omega(t) = Bt - C(\sqrt{4\mu + t} - 2\mu) \tag{23}$$

with $\mu = .0135\,{\rm GeV}$ and C being a parameter to be determined.

Coulomb and Nuclear Interference

The Coulomb and Nuclear interference term describes the interference between the Coulomb and nuclear interactions. The interference term is described by the phase $\phi(t)$, in eq. (12). Currently the phase can be expressed in two different forms presented below

$$\phi(t) = -\gamma_E - \ln\left(\frac{\Omega(t)}{2}\right) \tag{24}$$

$$\phi(t) = -\left[\gamma_E + \ln\left(\frac{\Omega(t)}{2}\right) + \ln\left(1 + \frac{8}{B\Lambda}\right)\right] + \frac{4|t|}{\Lambda}\ln\left(\frac{\Lambda}{4|t|}\right) - \frac{2|t|}{\Lambda} \tag{25}$$

with $\gamma_E \simeq 0.577$ being Euler's constant, $\Omega(t)$ being the nuclear modulus, B coming from the nuclear modulus, and Λ coming from the form factor. The West and Yennie interference phase, in eq. (24), is also used in earlier ALFA and TOTEM analyses [5] [12], and eq. (25) is the phase derived by Cahn [14].

Total Elastic Differential Cross Section

By combining the Coulomb and Nuclear interaction terms with the interference terms we get a theoretical formula for the total elastic differential cross section given by:

$$\frac{d\sigma}{dt} = \left|F_C e^{i\alpha\phi(t)} + F_N\right|^2 = \left|\frac{-2\sqrt{\pi}\alpha G^2(t)}{|t|} e^{i\alpha\phi(t)} + (\rho + i)\frac{\sigma_{\text{tot}}}{4\sqrt{\pi}} e^{-\Omega(t)/2}\right|^2 \tag{26}$$

$$= \frac{4\pi\alpha^2 G(t)^4}{t^2} - \frac{\sigma_{\text{tot}}\alpha G(t)^2}{|t|}[\rho\cos(\alpha\phi(t)) + \sin(\alpha\phi(t))]e^{\frac{-Bt}{2}} \tag{27}$$

$$+ (\rho^2 + 1)\frac{\sigma_{\text{tot}}^2}{16\pi} e^{-Bt} \tag{28}$$

The first term is the Coloumb term, the second term is the Coulomb and Nuclear interaction term, and the last term is the nuclear term. The contributions of the different terms and the total elastic differential cross section is shown in fig. 6. The parameters to be eastimated by the ALFA experiment are ρ, σ_{tot}, and the nuclear slope B. From theory fitted to earlier measurement the approximate values of the parameters at 900 GeV is $\rho = 0.1$, $\sigma_{\text{tot}} = 68\,\text{mb}$, and $B = 16\,\text{GeV}^2$ [15]. These are also the parameters with which the theory function in fig. 6 is plotted.

In ALFA the differential cross-section is estimated by measuring the scattering angles of the events, translating this value into a value of $|t|$ by using

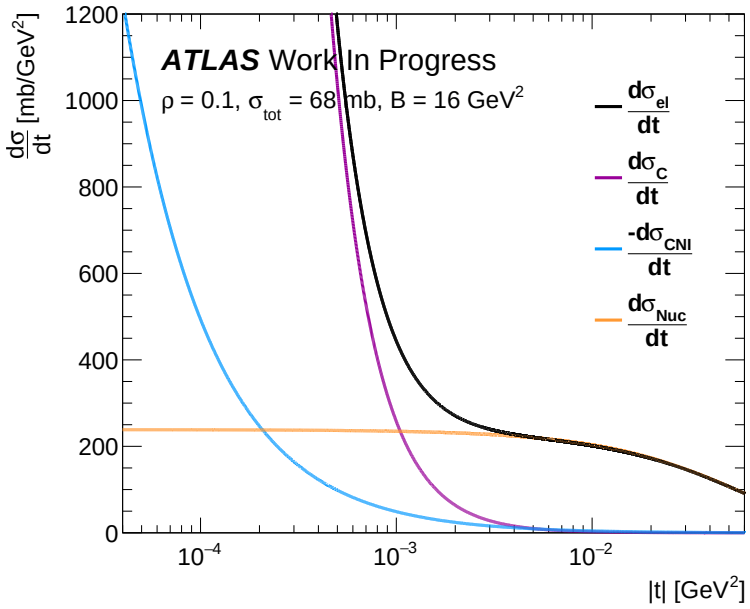

Figure 6: The theory function of the differential elastic cross section presented in eq. (28). The parameters are set to $\rho = 0.1$, $\sigma_{\text{tot}} = 68\,\text{mb}$, $B = 16\,\text{GeV}^2$. Note that the signed is flipped for the CNI term.

eq. (11), and then counting the number of events as a function of $|t|$. This distribution is then fitted with the theoretical formula in eq. (28).

Measurements of the total cross section is presented in fig. 7, where we see the rise for high energy collisions, at high values of $\sqrt{s}$. The rise of σ_{tot} is restricted by unitarity. When protons collide there are a certain number of outcomes. The probability of this finite number of outcomes should all add up to 1. Thus, σ_{tot} has to be bound in some way for high $\sqrt{s}$ in order to converge. This bound, proven through unitarity, is known as the Froissart-Martin bound and is given by:

$$\sigma_{\text{tot}}(s) =\leq \ln^2\left(\frac{s}{s_0}\right) \tag{29}$$

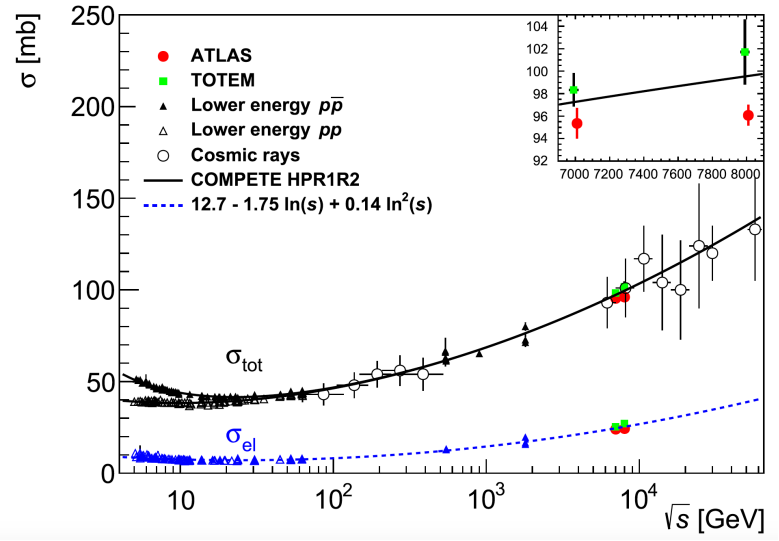

Figure 7: Measurements of the total cross section and the elastic cross section as functions of center-of-mass energy, $\sqrt{s}$ [16].

2 Experimental Setup

The following section will cover the experimental setup of the ALFA experiment. There will be a presentation of the Large Hadron Collider (LHC), including a description of the beam properties and dynamics. Then the ATLAS experiment will be explained briefly, followed by a thorough description of the ALFA experiment, and in end the data taking procedure is described.

2.1 The Large Hadron Collider

The Large Hadron Collider (LHC) is the largest particle accelerator in the world. Originally build for the Large Electron-Positron Collider (LEP) in the 1980's, the circular tunnel with a circumference of roughly 27 km now contains the LHC where protons are collided instead of electrons and positron. In the LHC protons are accelerated to velocities close to the speed of light and collided at large center-of-mass energies of up to 14 TeV [8].

The LHC is a part of the CERN complex, shown in fig. 8, underground on the border between France and Switzerland near Geneva. The LHC makes use of some of the other accelerators in the CERN accelerator complex to accelerate the protons making them ready for injection in the LHC-ring. The protons are obtained by removing the electrons of hydrogen in an electric field and after that the protons are accelerated for the first time in the linear accelerator LINAC2. The next stage of acceleration happens in the Proton Synchrotron Booster from there the protons are led into the Proton Synchrotron (PS) and then they are led into the Super Proton Synchroton (SPS) from where it is injected into the LHC ring. In the LHC the protons are accelerated further to energies up to 14 TeV [8].

2.1.1 LHC Design

The LHC is divided into eight octants as shown in fig. 9. Each octant consists of a straight section of about 500 m and is utilized for different purposes.

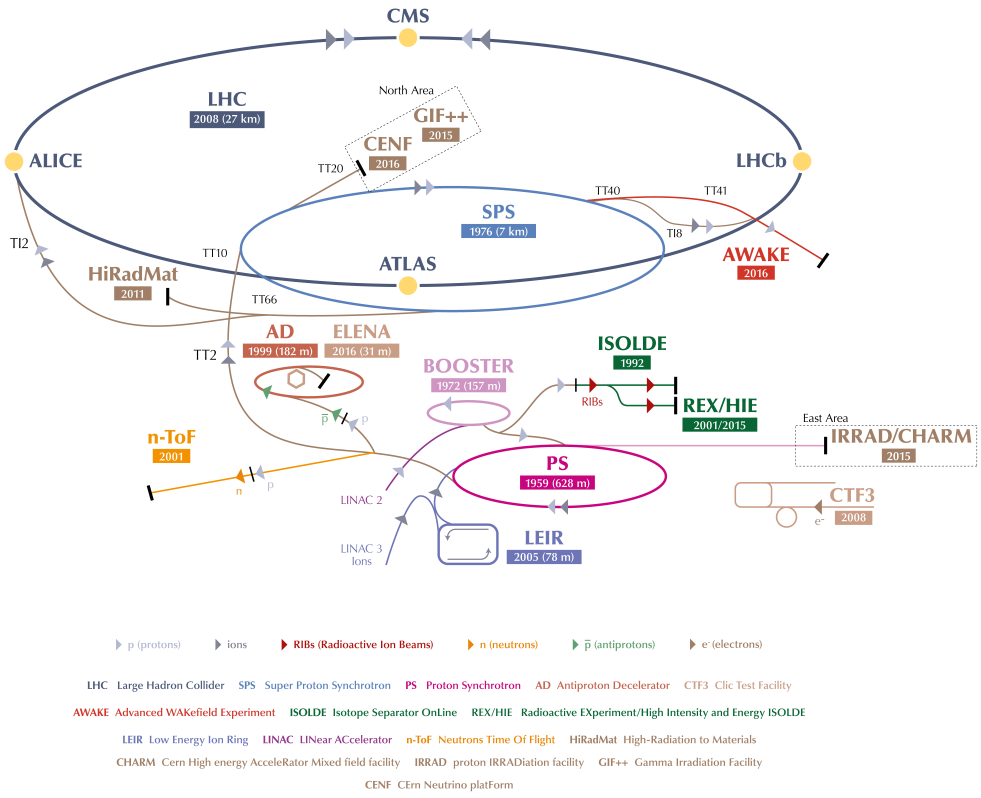

Figure 8: The CERN Accelerator complex [17]

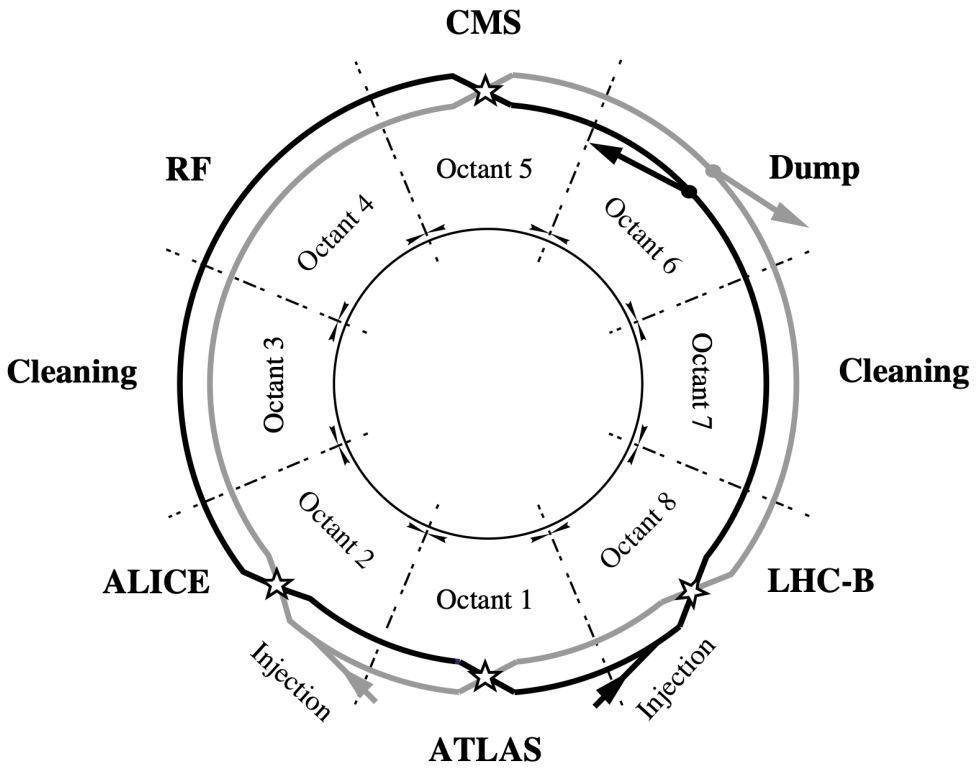

Figure 9: Schematic overview of the LHC divided into octants [18]

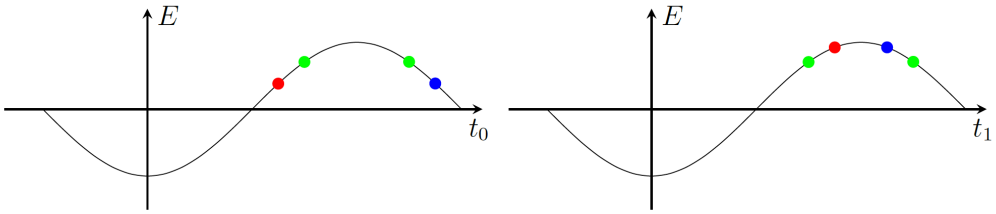

Figure 10: The principle behind the phase stability of the proton bunches [19]

The four big experiments at the LHC, ATLAS, ALICE, CMS, and LHC-B, are placed in the octants 1, 2, 5, and 8, respectively. The cleaning of the beam happens in octant 3 and 8, where the beam is collimated. A technique designed to reduce the width of the beam, by scraping off off-orbit protons that could possibly harm the accelerator machinery. The off-orbit protons are known as the beam halo particles [18]. In octant 6 the beam is dumped in the end of runs or if there is a problem. Here the beam is lead down into tunnels and dumped into absorbers [18].

In octant 4 the beam is accelerated by Radio Frequency (RF) cavities. The RF cavities uses an alternating electric field to accelerate the proton bunches to up to 14 TeV [8]. The RF cavities makes use of the Lorentz force to accelerate the charge protons. The Lorentz force is given by

$$\boldsymbol{F} = q(\boldsymbol{E} + \boldsymbol{v} \times \boldsymbol{B}) \tag{30}$$

Where q is the charge of the particle, $\boldsymbol{E}$ the electrical field, $\boldsymbol{v}$ the velocity of the particle, and $\boldsymbol{B}$ the magnetic field. The RF cavity uses an oscillating electric field in the direction of the beam to accelerate the protons. The oscillating fields of the RF cavities help maintain the proton bunches. Protons with high energies arrive to the RF cavities earlier than the protons with nominal energy, indicated by the green dot in fig. 10, and the protons with larger energies are thus given a smaller kick. Protons with lower energies than the nominal are given a larger kick. This is depicted on the rising side

of the electric RF field indicated by the red dot in fig. 10. When the protons become relativistic, larger energy will just result in larger radii of the particle trajectories, so relativistic protons with high energy will arrive later and get a smaller kick, whereas relativistic protons with low energy arrives early and get a large kick , as we see for the blue dot on the falling side of the RF cavity in fig. 10 [20]. As a result the particles in the bunches are tuned by the RF cavities to have close to nominal energy all the time, keeping the bunches together.

In the LHC there are 9300 magnets guiding the beam through the 27 km long tunnel [21]. Dipole magnets bend the beam along the circular design of the LHC, whereas the quadrupole and higher order magnets are used to focus and defocus the beam [20]. The magnets of the LHC are cooled down to 1.7 K by superfluid helium in order to make them superconductive. Operating with a current of about 12 kA they are able to achieve a magnetic field of about 8 T [8].

2.1.2 The Beam

This section covers the motion of the beam through the LHC, and the motion of elastically scattered protons from the interaction point in the center of ATLAS all the way to the detectors of ALFA placed on either side. The motion of the beam is described by so called beam optics. The term arises as the magnets of the LHC can be described very similar to optical lenses. Dipole magnets bend the beam while the higher order magnets focus and defocus the beam. This is crucial in order to control the beam and keeping it from from blowing up which would result in a beam loss, and to optimize data taking.

The coordinate system used to describe the motion of the beam in LHC is given by (x, y, s), x pointing towards the center of the LHC ring, y being the vertical coordinate, and s moving with the beam in the counterclockwise

direction. Thus, a proton in the beam center moving in a perfect trajectory around the LHC ring has the coordinates $(x, y, s) = (0, 0, s)$ [22]. The transverse motion of the beam in a ring of length L, is given by the Hill's equation:

$$\frac{d^2u(s)}{ds^2} + K(s)u = 0 \quad , \quad K(s+L) = K(s) \tag{31}$$

Where the last condition says that when travelling around the ring one time the particle should arrive at the same coordinate from where it started [20].

The real part of the solution to eq. (31) is given by

$$u(s) = \sqrt{\epsilon\beta(s)}\cos(\psi(s) - \psi(0)) \quad , \quad \psi(s) = \int_0^s \frac{ds}{\beta(s)} \tag{32}$$

$\psi(s)$ being the phase advance of the beam, ϵ is the emittance, and $\beta(s) = p^2(s)$ is the function which describes what is called the betatron oscillations. The betatron oscillations are fully described by $\beta(s)$ as it decides both the amplitude and the phase advance oscillations, ψ. It is important that the number of oscillations per turn, called the tune, is not an integer or half integer as this would amplify every small imperfection in the apparatus for each turn and in the end result in a beam loss [20].

Looking at the derivative of eq. (32) we get the divergence of the beam, i.e. the local angle of a particles in the beam with respect to the direction of the beam.

$$u'(s) = -\sqrt{\frac{\epsilon}{\beta(s)}}(\sin(\psi(s) - \psi(0)) - \alpha\cos(\psi(s) - \psi(0))) \quad , \quad \alpha = -\frac{\beta'(s)}{2} \tag{33}$$

When measuring the small scattering angles of elastic scattered protons, the divergence is important to take into account, as the divergence means that we cannot be certain of the incoming angle of the scattered protons. The

divergence therefore results in larger uncertainties on the measured scattering angles.

Taking energy loss and momentum dispersion into account the solution to the Hill's equations can be written as

$$\begin{bmatrix} u(s) \\ u'(s) \\ \Delta p/p \end{bmatrix} = M \begin{bmatrix} u^*(s) \\ u'^*(s) \\ \Delta p^*/p \end{bmatrix} \tag{34}$$

$$M = \begin{bmatrix} \sqrt{\beta/\beta^*}(\cos\psi + \alpha^* \sin\psi) & \sqrt{\beta\beta^*}\sin\psi & D_u \\ \frac{(\alpha^* - \alpha\cos\psi - (1+\alpha^*\alpha\sin\psi))}{\sqrt{\beta/\beta^*}} & \sqrt{\beta/\beta^*}(\cos\psi - \alpha\sin\psi) & D'_u \\ 0 & 0 & 1 \end{bmatrix} \tag{35}$$

Where $u(0) = u^*$, $u'(0) = u'^*$, $\beta(0) = \beta^*$, $\alpha(0) = \alpha^*$, $\alpha(s) = \alpha$, $\beta(s) = \beta$, $\psi(s) = \psi$, $M(s) = M$ being the transport matrix, and $s = 0$ is taken to be the exact center of the beam crossing. For elastic scattering the energy loss Δp can be neglected [23]. This simplifies the equations to

$$\begin{bmatrix} u(s) \\ u'(s) \end{bmatrix} = \mathbf{M} \begin{bmatrix} u^*(s) \\ u'^*(s) \end{bmatrix} \tag{36}$$

$$\mathbf{M} = \begin{bmatrix} \sqrt{\beta/\beta^*}(\cos\psi + \alpha^* \sin\psi) & \sqrt{\beta\beta^*}\sin\psi \\ \frac{(\alpha^* - \alpha\cos\psi - (1+\alpha^*\alpha\sin\psi))}{\sqrt{\beta/\beta^*}} & \sqrt{\beta/\beta^*}(\cos\psi - \alpha\sin\psi) \end{bmatrix} = \begin{bmatrix} M_{11} & M_{11} \\ M_{21} & M_{22} \end{bmatrix} \tag{37}$$

The matrix M is known from the beam optics of the LHC, meaning the position of the protons at ALFA can be expressed by

$$u(s) = M_{11}u^* + M_{12}u'^* \tag{38}$$

For elastic proton scattering the interaction point for the two protons are identical, and the scattering angles are equally large with opposite signs. This gives us

$$u_L - u_R = M_{11}u^* + M_{12}u'^* - (M_{11}u^* - M_{12}u'^*) = 2M_{12}u'^* \tag{39}$$

$$\Leftrightarrow u'^* = \theta_u^* = \frac{u_L - u_R}{M_{12}} = \frac{u_L - u_R}{\sqrt{\beta\beta^*}\sin\psi} \tag{40}$$

Where u_L and u_R denotes the measured coordinates of the left and the right side of the interaction point (IP), and θ_u^* is the u-component of the scattering angle.

During the 900 GeV elastic campaign the optics of ALFA is designed such that $\psi = \pi/2$ and $\beta^* = 50$ in the x-plane and $\beta^* = 100$ in the y-plane. $\psi = \pi/2$ maximises the effective lever arm $L_{\text{eff}} = \sqrt{\beta\beta^*}\sin\psi$, which maximises the precision on the measurement of the angle, as is seen in eq. (40). During the elastic campaign ALFA is optimized such that $\alpha \simeq 0$ making the measured coordinates in the y-plane in ALFA independent of the position of the interaction point. This optics setup is called parallel-to-point optics and can only be done in one plane. For ALFA it is the vertical direction which is optimized, as the ALFA detectors comes in above and below the beam pipe [23]. Considering only particles scattering in the y-plane, the minimum measurable value of the scattering angle can be estimated with eq. (36) and by substituting $u_y'^* = \theta_y^*$ and $u_y = y$.

$$y_{min} = \sqrt{\beta\beta^*}\sin\psi\theta_y^* \Leftrightarrow \theta_y^* = \frac{y_{min}}{\sqrt{\beta\beta^*}} \rightarrow -t = (p\theta_y^*)^2 = \frac{p^2 y_{min}}{\beta\beta^*} \tag{41}$$

Remembering that $\psi = \pi/2$ because of parallel-to-point optics. Here y_{min} is dependent on the beam spot width and of how close to the beam the ALFA detectors is able to go.

Emittance

Emittance is a measure of the width of the beam. Every proton in the beam will oscillate on its way around the LHC ring due to the betatron oscillations. At each point around the accelerator the motion of the particle is described by the coordinates u and u'. At each turn the coordinates shift and at any given point in s, u and u' maps out an ellipse [20]. The ellipse is given by the formula:

$$\gamma u^2 + 2\alpha u u' + \beta u'^2 = \epsilon \quad , \quad \gamma = \frac{1-\alpha^2}{\beta} \tag{42}$$

Louivilles theorem states that if only conservative forces acts on the protons, the area of the ellipse, $\pi\epsilon$, remains invariant. However, there are several non-conservative forces acting in the accelerator experiment acting on the protons, e.g. energy loss, synchrotron radiation etc. Some of these forces blow up the beam but some can also be used to cool the beam and bring down the emittance. The maximum values of u and u' is given by

$$u_{max} = \sqrt{\epsilon\beta} \quad , \quad u'_{max} = \sqrt{\epsilon\gamma}, \quad \text{with} \quad \beta = \frac{v}{c}, \quad \gamma = \frac{1}{\sqrt{1-\beta^2}} \tag{43}$$

From this it is clear that the emittance, and therefore the beam spot, can be made smaller by minimizing β or larger by maximizing β.

Every time the beam is accelerated in the s-direction the u'_{max} is reduced as it is inversely proportional to β which is a function of the momentum of the protons. Thus, the normalized emittance is defined as

$$\epsilon_N = \gamma\beta\epsilon \tag{44}$$

Using eq. (43) we can get an expression of y_{min} as u_{max} is the beam spot width. For ALFA we define y_{min} as a multiple of the beam spot width [24].

$$y_{min} = n\sqrt{\epsilon\beta} \tag{45}$$

Combining with eq. (41) and eq. (44) we get the minimum achievable measurement of momentum transfer, $t_{\min}$ [24].

$$-t_{min} = (p\theta_y^*)^2 = \frac{p^2 y_m in^2}{\beta\beta^*} = \frac{n^2 p^2 \epsilon}{\beta^*} = \frac{n^2 p^2 \epsilon_N}{\gamma\beta^*} \tag{46}$$

With the protons travelling near the speed of light $\beta = v/c \approx 1$. However, the ALFA detectors is not able to go as close as the theoretical prediction, but is still able to cover the range of interest in t [24].

The emittance is measured in various ways at the LHC. One of the ways to measure the emittance is by Van der Meer scans. Van der Meer scans are done by separating the beams and then counting the event rate while moving the beams in opposite directions through each other. By then we can both get a measurement of the emittance and luminosity [1].

The width of the beams is also measured with wire scanners. Wire scans are done by moving a carbon wire through the beam while counting the rate of scattered particles with scintillators surrounding the wire scanner [24].

The evolution of the emmitance throughout a run is measured by a Beam Synchrotron Radiation Telescope (BSRT). The BSRT measures the synchrotron radiation from a dipole magnet, and from that a profile of the beam is calculated.

2.1.3 Luminosity

One the most important parameters when doing particle colliding experiments is the number of interactions occurring when particles collide. Here the luminosity plays a central role. The instantaneous luminosity, $\mathcal{L}$, is a measure of the collision rate. Recalling that the cross section is a measure of the probability of an event, the total number of events can be calculated by integrating the instantaneous luminosity over the period of the experiment [1].

$$N = \sigma \int_0^t \mathcal{L}(t')dt' = \sigma L \tag{47}$$

where L is called the integrated luminosity and σ is the cross-section. Hence, to determine the cross section by counting events, the luminosity needs to be known. The luminosity is determined by the accelerator parameters and for the LHC the instantaneous luminosity can be expressed as

$$\mathcal{L} = \frac{f n_1 n_2}{4\pi\sigma_x\sigma_y} \tag{48}$$

with f being the frequency of colliding bunches, n_1 and n_2 being the number of protons in each of the colliding bunches, and σ_x and σ_y being the beam spot width in the x and y direction. To get a large amount of event the luminosity needs to be big, hence a small beam spot size is desirable. In the 900 GeV run the emittance is bigger than for runs at higher energies as the emittance, and therefore the beam spot size, is inversely proportional to the beam energy [24].

Lack of accuracy of luminosity calculations will propagate to the error of the measured cross-section, making the luminosity a very important factor of the experiment [1].

2.2 ATLAS

ATLAS is the largest particle detector on the LHC ring, and it is on either side of the ATLAS detector that the ALFA detectors are located. ATLAS is an acronym for A Toroidal LHC AparatuS. ATLAS is designed to detect many different particles in a large range of phase space surrounding the beam interaction point (IP) located in the center of ATLAS. An illustration of the ATLAS detector is shown in fig. 11 where the different parts of the detector are labelled [25].

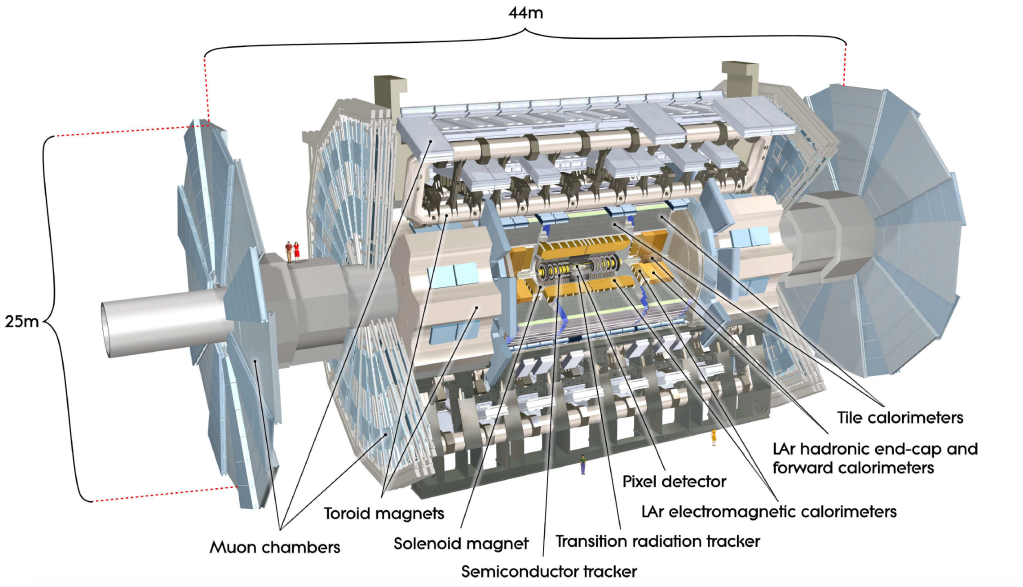

Figure 11: An illustration of the ATLAS particle detector. [25]

The inner detector consists of a silicon pixel detector, silicon strip detector and a transition radiation tracker, which are able detect charged particles travelling through. The inner detector is used to reconstruct interaction vertices and to measure momentum of charged particles. In order to measure the momentum of the charged particles a 2 TeV magnetic field is applied over the whole inner detector. In combination with the other the detectors of ATLAS the inner detector plays a crucial role in particle recognition [25].

Outside the inner detector is the calorimeters. The calorimeters consist of an electromagnetic calorimeter and a hadronic calorimeter. The electromagnetic calorimeter is a sampling calorimeter and uses liquid argon (LAr) as its detector medium and lead as the absorber. The outermost calorimeter is the hadronic calorimeter, which consists of plastic scintillator tiles with steel as the absorber. At the end caps of the calorimeters, electromagnetic end cap calorimeters, hadronic end cap calorimeters, and forward calorimeters are installed. They all use LAr as detector medium, and copper or a combination of copper and tungsten as detector medium. The calorimeters are designed to measure the energy of particles decaying and being fully absorbed within

the calorimeter, which is why the calorimeters have to be quite thick [25].

The outermost part of the detector is the muon spectrometer. The muon spectrometer is designed to detect muons traversing the whole detector without decaying [25].

2.2.1 ATLAS Trigger System

During an LHC run the proton-proton interaction rate is about 1 GHz, whereas the data recording is limited to about 200 Hz due to technology limitations. It requires a rejection system to bring the event rate down to a manageable level. This rejection system is called the trigger system. ATLAS has two initial trigger levels, the level 1 (L1) trigger system and the high level trigger (HLT) system.

The L1 trigger system is based on custom electronics and uses information from the calorimeters and muon spectrometers. The Central Trigger Processer (CTP) is what ultimately decides whether to keep an event or not, based on the information of the different trigger items from the L1 calorimeter triggers (L1Calo) and L1 muon triggers. The L1Calo trigger identifies events with high transverse energy deposited in the calorimeters, and the L1 muon trigger searches for particles with high transverse momentum originated from the interaction point. Each trigger item contains a prescale, n, which decides that only the n'th event should be saved. The L1 trigger system reduces the event rate from 1 GHz to 75 kHz [25].

The L1 trigger system passes events through to the HLT system. the HLT consists of the level 2 trigger (L2) and the event filter. It uses information from the regions of interest, i.e. information on coordinates, energy, and signature types, to manage what data to read-out for offline analysis. The HLT system reduces the data from 75 kHz to around 200 Hz [25].

2.3 ALFA

In this section the design of the ALFA (Absolute Luminosity for ATLAS) experiment covered in detail. The ALFA experiment is designed to measure

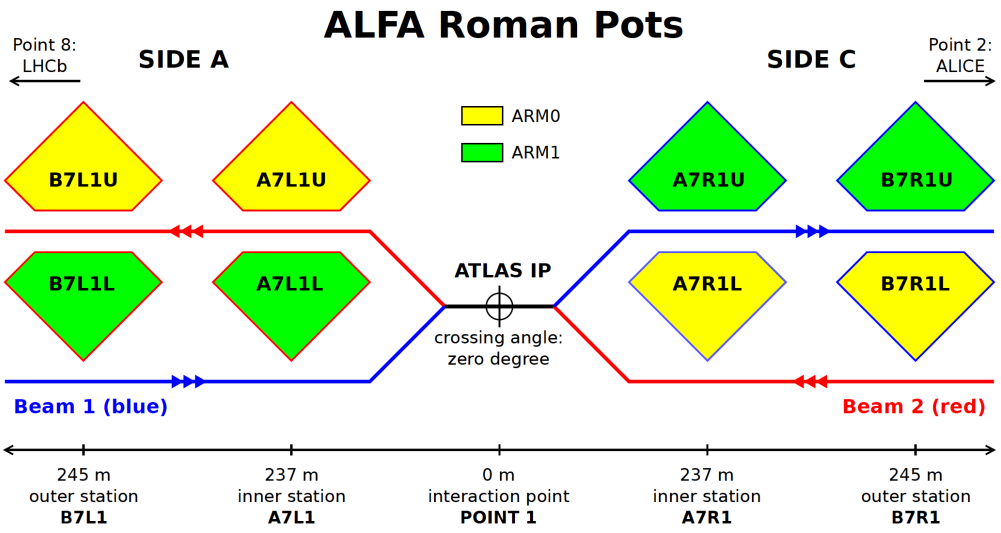

Figure 12: An overview of ALFA. [26]

elastic proton-proton scattering at the smallest possible angles in order to measure the total elastic cross section at very low energy transfers in order to study the elastic Coulomb and nuclear scattering amplitudes.

2.3.1 Design

ALFA consists of eight detectors, four on each side of the interaction point (IP) in ATLAS. On each side there are two detectors above the beam pipe and two detectors below the beam pipe. An overview is presented in fig. 12. The inner detectors are placed 237 m on each side of the ATLAS IP, with the outer detectors placed 8 m further out at 245 m. The eight detectors are named such that the first letter denotes if its an inner (A) or outer (B) detector. The number 7 indicates that it is the seventh element seen from the IP. L/R indicates if the detectors on the left- or right-hand side of the IP. The left side is also called the A-side while the right side is called the C-side. 1 means that the detectors are installed in the straight section of octant 1, and the final letter U or L indicates if its an upper or lower detector [26].

The ALFA detectors are installed in Roman Pots (RP), which sits above

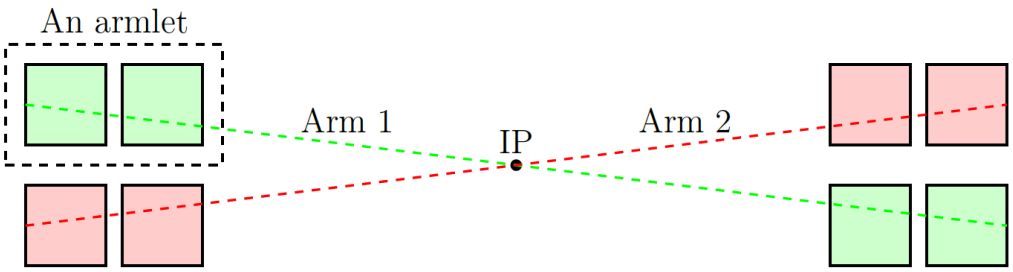

Figure 13: An illustration of ALFA divided into arms and armlets [19].

and below the beam pipe and are separated from the primary ultra high vacuum of the beam pipe. This allows the detectors to be moved extremely close to the beam by high precision screws, in order to measure elastically scattered protons at extremely small angles of the order of 10 μRad. [5].

ALFA is divided into arms and armlets as seen in fig. 13. Each armlet has two detectors and makes up an arm with the diagonally opposite armlet. Due to momentum conservation elastic scattered protons has equal and opposite scattering angles as seen in fig. 5 and described in section 1.4.1. Thus, when measuring an elastically scattered proton in A7L1U and B7L1U a proton with the same but opposite scattering angle should be measured in A7R1L and B7R1L. These four detectors constitutes arm 1 while A7L1L and B7L1L, and A7R1U and B7R1U makes up arm 2, as indicated by yellow and green on fig. 12 [5].

Each of the ALFA detectors consists of a Main Detector (MD), which measures the particles, a Overlap Detector (MD) that measures the gap between an upper and lower detector, and trigger detectors to reduce noise and pick out elastic events [27].

2.3.2 Main Detector

The Main Detectors measure the coordinates of the elastically scattered protons. The MDs consist of two sets of 10 layers of 64 scintillating fibres. One set glued to the front of a titanium plate, and the other set glued to the back of the plate. The two sets of fibre are arranged perpendicular to each other

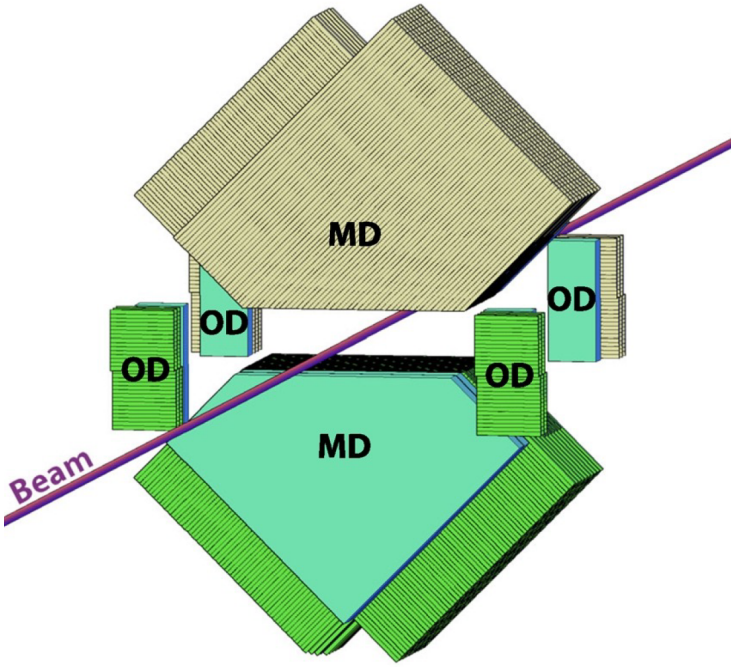

Figure 14: An illustration of the main and overlap detector of ALFA [5].

with angles of $\pm 45°$ with respect to the y-axis. Each set of fibre makes up a plane. The set at the front of the titanium plate is called the U-plane, and the set on the back is called the V-plane. 40 of the 64 fibres are cut with an angle of 45°. This gives the MD diamond shape with the bottom being horizontal in order to get as close the beam as possible. A depiction of the Main Detector (MD) and Overlap Detector (OD) are shown in fig. 14, where the diamond shape of the MD can be seen [5].

To prevent signals in one fibre from migrating to adjacent fibres, all fibres are coated with thin aluminum film. All fibres are also coated with aluminum at the ends except the fibres that are cut by 45°. However because of the 45° cut the total internal reflection is sufficient enough to keep the light inside the scintillating fibres [27].

The fibres are staggered with 1/10 overlap of the fibre thickness in order to improve the detector resolution. In reality this staggering was not achieved to perfection. So due to staggering imperfections, cross-talk between fibres,

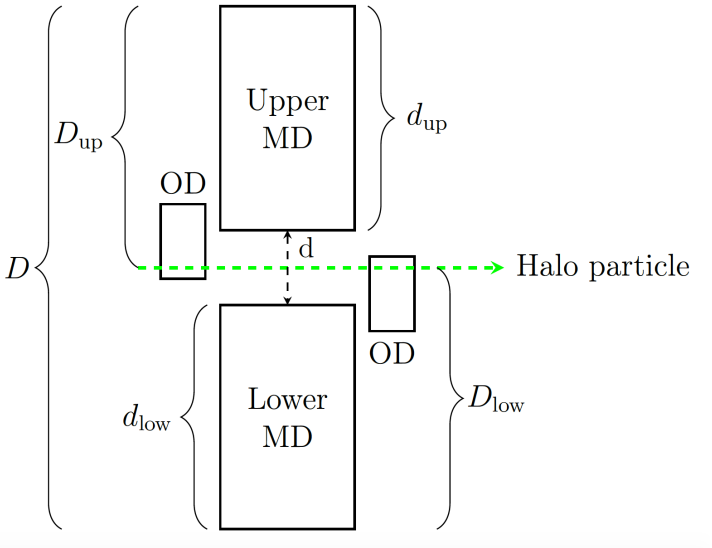

Figure 15: Scheme of the measurement of the gap between the upper and lower detector, by detecting halo particles with the overlap detectors [19].

and inefficient fibres, the resolution of the detectors was measured to a value around 30 µm [5].

The detector signal of both the MD and OD is read out by 23 multi-anode photomultipliers (MAPMT) to 64 channels [5].

2.3.3 Overlap Detector

The Overlap Detectors (OD) are positioned on each side of the MD. The OD makes use of halo particles travelling along the beam to determine the width of the gap between the upper and lower detectors. The principle of measuring the distance between the MDs are shown in fig. 15.

The ODs consists of three layers of 30 scintillating fibres each, with 15 fibres glued to the front of the titanium plate and 15 fibres glued to the back. The fibres are aluminum coated and are staggered by 1/3 of the fibre sized and are placed horizontally in order to measure the vertical distance. The fibre staggering results in a resolution of 50 µm. As depicted in fig. 14 there are two independent ODs on each side of the MD [5].

2.3.4 Trigger Detector

Both the MDs and the ODs are covered by a 3 mm thick scintillator plate, called the trigger detectors. The purpose of the trigger detectors is to reduce noise of the individual detectors. Each MD detector has two scintillating tiles and reduces noise by requiring a coincidence in both trigger tiles. Each OD has only one trigger tile and require a coincidence in both an upper and lower OD to trigger [5].

2.4 Data Taking

This section covers the different aspects of data taking of the ALFA detector. The data used in this thesis is from the 900 GeV elastic physics program, which was a part of the special physics run at the LHC that took place in October 2018 [24]. The data analysis in this thesis focuses on data taken with the optics setting of $\beta^* = 100$ m, to study elastic events at small values of $|t|$. This thesis studies the data taken in run 363461, one of the 12 runs taken with $\beta^* = 100$ m and beam energy of 450 GeV.

2.4.1 Alignment

When the LHC is filled the beam is not necessarily centered in the beam pipe, and the position of the beam can vary from fill to fill. Through a procedure called Beam Based Alignment (BBA) the ALFA detectors are placed equally close to the beam center. The BBA procedure has adopted its concept from the collimation of the beam. The RPs are moved slowly towards the beam center in steps of 10 µm. As the RPs reaches the beam halo edge they will start scraping the beam similar to the collimators. The beam center is then found by monitoring the ALFA trigger rate and the signal in Beam Loss Monitors (BLM), installed behind the ALFA stations. When seeing a sharp rise in the signal rate the beam halo edge is found. From this the beam center is calculated and the RPs positions are determined. The position of the RPs are not placed exactly on the beam edge but are instead placed 3σ

away from the beam center, with σ being the beam spot width [27].

2.4.2 Data Monitoring

During the experiment run it is important to monitor the data taking in order to get as high quality data as possible. This is done by monitoring certain trigger items that gives an initial idea of the signal to background ratio. Some of the level 1 (L1) trigger items monitored during the data taking period are presented in table 1.

Each trigger item are paired with two buch group triggers, BGRP0, BGRP1. BGRP0 triggers on every possible bunch crossing except the ones in the abort gap. BGRP1 triggers on colliding bunches. These make sure that events are only recorded in coincidence with two colliding proton bunches. L1_ALFA_ANY triggers if any of the MDs trigger and is thus the loosest of the triggers in table 1. The trigger items L1_ALFA_ELAST15 and L1_ALFA_ELAST18 are elastic triggers. They trigger if one detector in an armlet is hit in coincidence with one of the detectors in the diagonally opposite armlet. L1_ALFA_ELAST15 is the arm 1 trigger and L1_ALFA_ELAST18 is the trigger for arm 2. L1_ALFA_SYST17 and L1_ALFA_SYST18 are background triggers. L1_ALFA_SYST17 triggers if a detector in an upper armlet has a coincident event with one of the detectors in the other upper armlet. The same goes for L1_ALFA_SYST18 which is just for the lower detectors instead.

By observing the event rate for the elastic triggers and background triggers the quality of data can be optimized. In fig. 16 it is seen how the event rates of the elastic triggers, L1_ALFA_ELAST15 and L1_ALFA_ELAST18, are higher than for the background triggers, L1_ALFA_SYST17 and L1_ALFA_SYST18, in the beginning of the data taking. As time goes on the background rate starts to grow as the beam halo intensifies. To bring down the noise, the beam is collimated when the background triggers reaches a certain rate. The beam monitoring graph in fig. 16 shows trigger rates just before beam scraping [24].

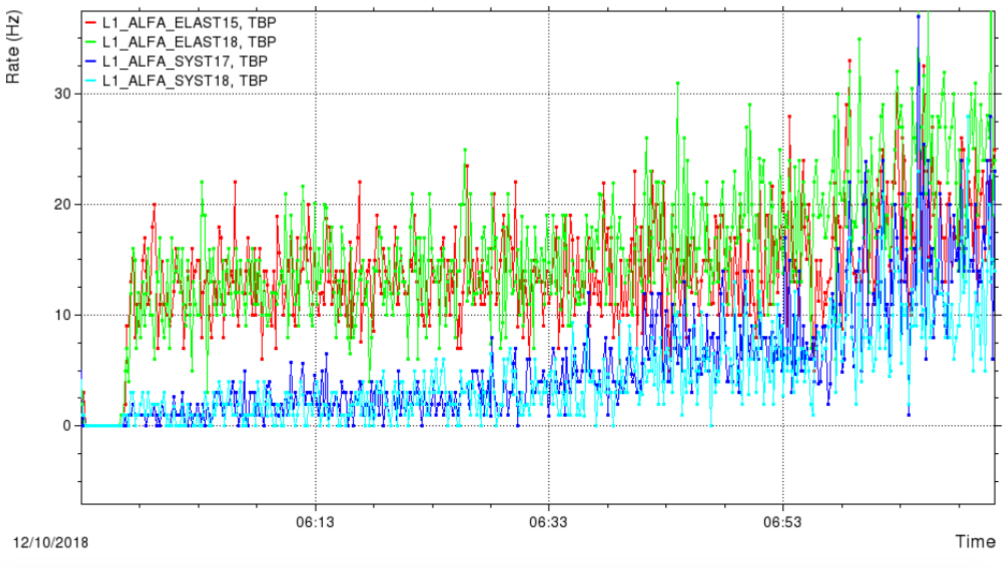

Figure 16: Beam monitoring graph for the two elastic and two background triggers [24].

Trigger Item	Trigger Logic
L1_ALFA _ANY	B7L1U ∨ B7L1L ∨ A7L1U ∨ A7L1L ∨ A7R1U ∨ A7R1L ∨ B7R1U ∨ B7R1L
L1_ALFA_ELAST15	(B7L1U ∨ A7L1U) ∧ (A7R1L ∨ B7R1L)
L1_ALFA_ELAST18	(B7L1L ∨ A7L1L) ∧ (A7R1U ∨ B7R1U)
L1_ALFA_SYST17	(B7L1U ∨ A7L1U) ∧ (A7R1U ∨ B7R1U)
L1_ALFA_SYST18	(B7L1L ∨ A7L1L) ∧ (A7R1L ∨ B7R1L)

Table 1: List of L1 trigger items used to monitor data during a data taking period. All trigger items has a prescale of 1 and are paired with bunch group triggers BGRP0, BGRP1 [24].

As time goes on the event rate is expected to drop, as the number of protons in the bunches are reduced by elastic scattering, and various other processes along the way around the LHC ring. The collimation scrapes away a lot of the beam halo particles, but it also affects the beam as scattered shower particles from the collimators could go in and affect some of the beam protons [24].

The data taken in the ALFA experiment is divided into luminosity blocks, or lumiblocks (LBs), which is a period of around 60 s, where the background level and beam properties are stable. Thus, if a sudden change in the run conditions occurs, data can be excluded so only good data is used for the analysis. The lumiblocks are desired to be as small as possible in order for the smallest amount of data to be discarded. However, the lumiblocks are required to have a certain length, in order to be able to measure the integrated luminosity of the experiment [19]. Through run 363461 the preliminary measurements of integrated luminosity indicated an integrated luminosity of $90.2\,\mu b^{-1}$ [24].

2.4.2.1 Collimation

During a data taking run in the LHC the number of off-orbit particles grow due to various beam dynamics. These particles are called the beam halo particles. The beam halo particles results in increased background and if the beam halo becomes to large is may cause quenches in the superconductive magnets. The magnets of the LHC is cooled to very low temperatures, and even small energy deposits may cause the temperature to rise making them lose their superconductive properties. To prevent quenches and reduce the beam halo induced background events in particle experiments, beam collimators are installed in the LHC. The collimators scrape the beam from halo particles reducing the number of background events. During collimation of the beam, the data taking is paused as the collimators creates a lot of shower particles during beam scraping, which would result in a rise in background events during a scraping period [26].

Initial test showed a signal rate of about 10 Hz, while the combined signal

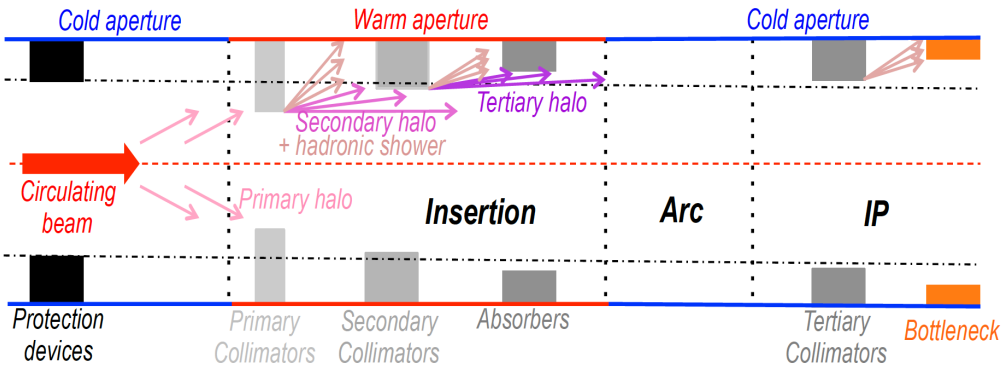

Figure 17: Illustration of the collimation principle. [28]

and background rate was around a few kHz not long after each scraping. As a result more advanced scraping schemes was developed, namely a two stage collimation scheme and a crystal collimation scheme [26].

The two stage collimation schemes consists of a primary collimator, TCP, made of carbon-fibre-composite material to withstand the large amount of energy deposited in the collimator. The secondary collimators, TCLA, which are absorber collimators absorbs secondary halo particles and hadronic shower particles from the primary collimators. An illustration of collimation are presented in fig. 17, where it is seen how halo particles hits the primary collimators, resulting in hadronic showers which are then absorbed by the secondary collimators.

For the two stage collimation scheme, the primary collimators are moved into a distance of 2.5σ of the beam center, with σ being the beam width, and then moved to data taking position. Then the absorber collimators are moved to 2σ until the signal in the Beam Loss Monitors (BLM), placed around the beam, stabilises. This ensures that the halo from 2σ and beyond are cleaned. The secondary collimators are then moved to 2.5σ and the Roman pots, where the ALFA detectors sits, are moved to a position of 3σ from the beam [26].

For the two stage collimation scheme an initial scraping is carried out during data taking. During data taking the trigger rates are monitored and

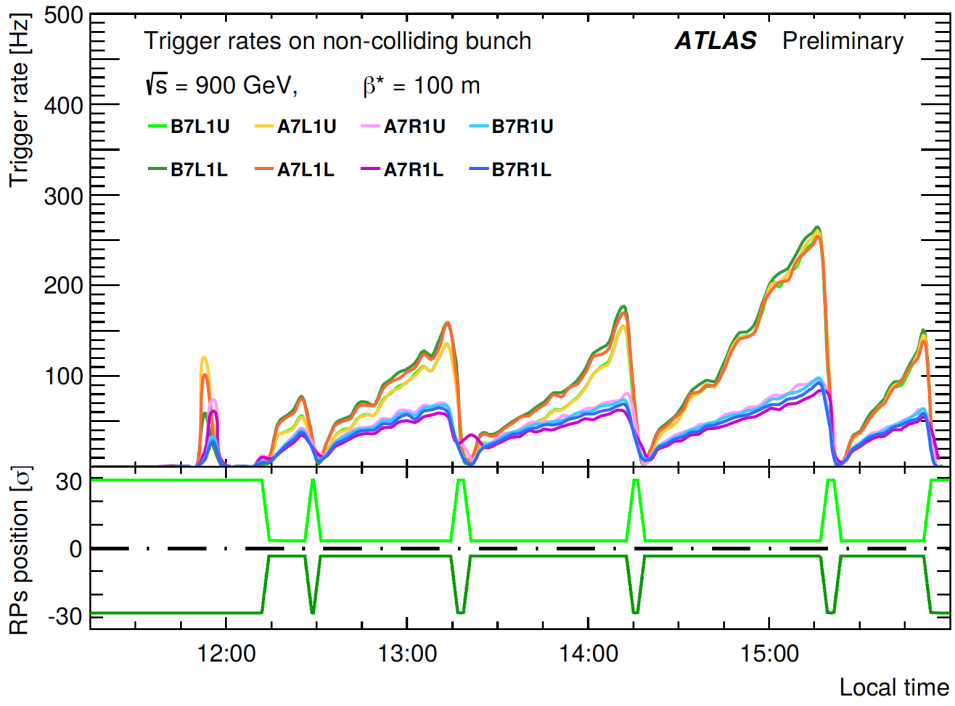

Figure 18: Trigger rates of non-colliding bunches (upper) and the Roman Pot position during data-taking (lower), showing the effect of the initial scraping and rescraping due to the two stage collimation scheme. Run 363469 (LHC Fill 7284). [26]

when they become two high a rescraping is carried out. This is shown in fig. 18. Here the trigger rate for non-colliding bunches, of each of the detectors increases as we move forward in time, and then suddenly drops due to rescraping of the beam. The positions of the Roman Pots indicate when the rescraping takes place, as the RPs moved out during scraping [26]. The trigger rate of non-colliding bunches are used, as this only show background events.

The crystal collimation scheme is similar to the two stage collimation scheme. However, instead of secondary and tertiary collimators and absorbers, there is a bent crystal which steers the secondary halo particles and hadronic shower particles from the primary collimators into an absorber. An

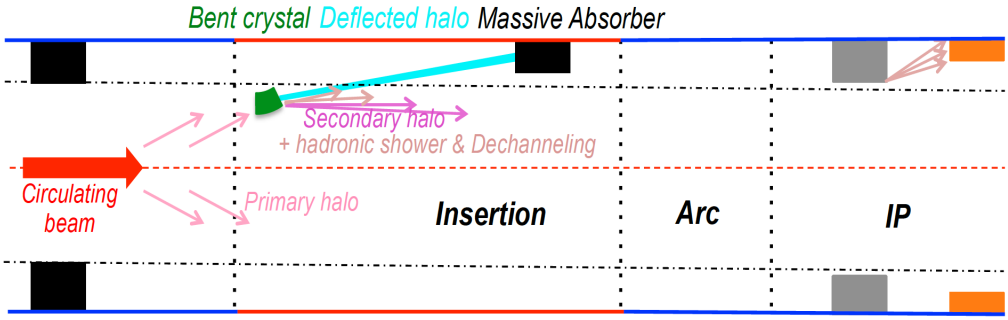

Figure 19: Illustration of crystal collimation principle. [28]

illustration of this is shown in fig. 19. Here it is seen how the crystal bends the secondary particles into the massive absorber.

For the crystal collimation scheme the primary collimator is moved to 2.5σ of the beam. Afterwards the collimators are moved out to 2.7σ and the bent crystal are moved to 2.5σ. The crystal collimation is so efficient that there, over a data taking period of about three hours, is no need for rescraping. This is shown in fig. 20.

2.4.3 Monitoring Emittance

The emittance of the beam in the LHC is measure by wire scanners installed for both beams. The wire scanners consist of a carbon wire moved slowly through the transverse plane of the beam at low intensities. There is a wire scanner installed both for the x and y direction. The wire is moved slowly through the beam in constant motion, to ensure that there is measurement for each proton bunch. The wire causes scattering of protons, and the event rate of scattered particles are measured by a scintillator placed outside the beam pipe. This event rate is then translated into a Gaussian beam profile in each direction. The wire scanners gives two measurements per scan, one for the inward motion and one where the wire is retracted [29].

The evolution of the emittance is monitored by a Beam Synchrotron Radiation Telescope (BSRT) placed just down stream of a dipole magnet. The

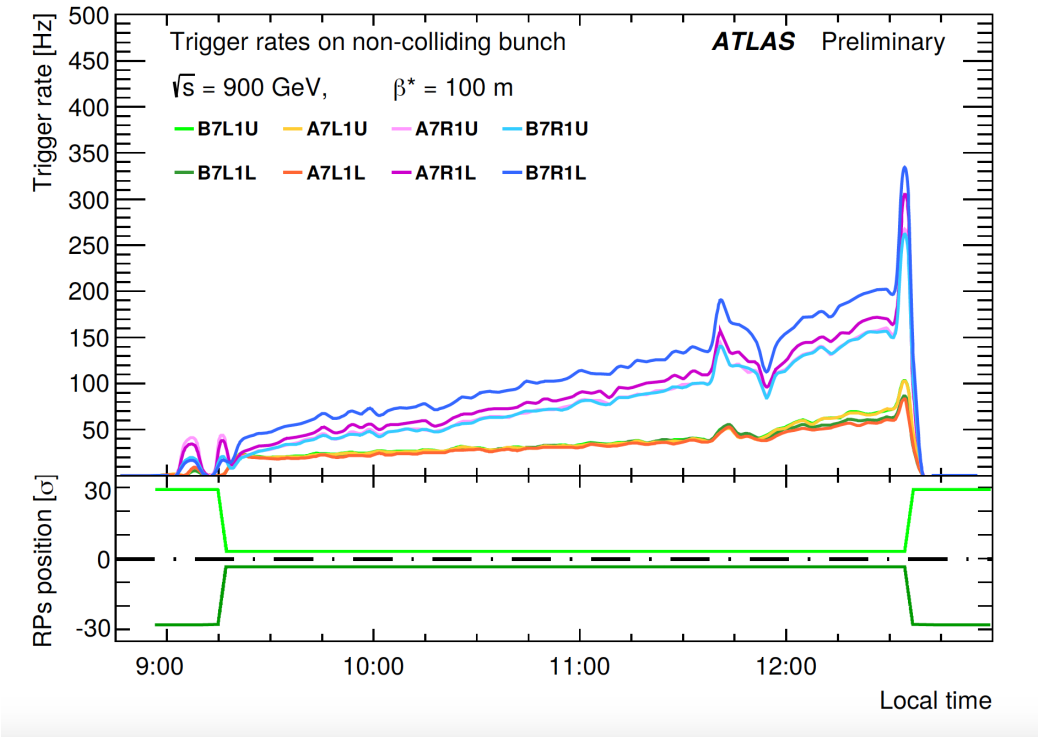

Figure 20: Trigger rates of non-colliding bunches (upper) and the Roman Pot position during data-taking (lower), showing the effect of the initial scraping and rescraping due to the crystal collimation scheme. Run 363500 (LHC Fill 7289) [26].

dipole bends the beam causing the emittance of synchrotron radiation. For low beam energies the intensity of synchrotron radiation emitted is not strong enough to be measured, and is therefore amplified by an undulator. In the space between the dipole and the next magnet the synchrotron radiation is extracted by a mirror and passed on to the telescope outside the beam vacuum. From the radiation signal the telescope produces images of the beam profile and is able to do so throughout an entire run. The measurement from the BSRTs are calibrated with the emittance measurements from the wire scans by the relation [29]:

$$\sigma_{BSW} = \sqrt{\sigma_{BSRT} - \sigma_{WS}}$$

From the measurement of the beam spot width σ_{BSW} the emittance can be calculated by the relation:

$$\epsilon = \frac{\sigma_{BSW}^2}{\beta(s)}$$

Where $\beta(s)$ is the beta function at some point s. The wire scans measures the emittance at the beginning of the run whereas the BSRTs measures the evolution of the emittance [29]. These measurements are later used in the Monte Carlo (MC) simulation, in order to estimate the beam spot width and the divergence throughout the data run. The divergence is related to the emittance by

$$D_u = \sqrt{\frac{\epsilon_u}{\gamma\beta^*}} \tag{49}$$

2.4.4 Optics

The trajectories of protons scattering elastically and travelling roughly 240 m to the ALFA detectors are affected by the magnetic fields of the dipole and quadrupole magnets that are part of the LHC machinery. These magnets

Detector (U/L)	M_{11}	M_{12}	M_{21}	M_{22}
A7L1$_x$	-1.69399	9.59626	0.00005	-0.59062
B7L1$_x$	-1.69355	4.71859	0.00005	-0.59062
A7R1$_x$	-1.7658	9.81712	-0.00223	-0.55393
B7R1$_x$	-1.7842	5.24277	-0.00223	-0.55393
A7L1$_y$	0.02012	189.128	-0.00559	-2.81583
B7L1$_y$	-0.02602	165.874	-0.00559	-2.81583
A7R1$_y$	0.02048	186.165	-0.00569	-2.85018
B7R1$_y$	-0.02647	162.629	-0.00569	-2.85018

Table 2: Transport matrix values given by the optics design of the 900 GeV elastic physics campaign [24].

where optimized in the 900 GeV run in order to be able to obtain protons scattered at very small angles. During this elastic campaign the LHC was optimized with $\beta^* = 100\,\text{m}$ in the y-plane and $\beta^* = 50\,\text{m}$ in the x-plane, and with the betatron phase advance $\psi = \pi/2$ in so called parallel-to-point optics as discussed in section 2.1.2.

The effect of the magnets combined is written as the transport matrix $\mathbf{M}$ given in eq. (35) in section 2.1.2. There is a transport matrix for the inner detectors on each side of the ATLAS IP and a transport matrix for the outer detectors on both sides of the IP. These transport matrices are calculated by the CERN - BE/ABP Accelerator Beam Physics Group, and their program called MadX, which simulates and optimizes beam dynamics [30]. The values of the matrices are given in table 2.

Recalling, from eq. (38), that it is the values of M_{11} and M_{12} which are decisive for the position of the protons when reaching the ALFA detector. Thus the parallel-to-point optics are given by the small values of $M_{y,11}$. They suppress the importance of knowing the exact vertical coordinate of the interaction point. However the large values in $M_{y,12}$ demands a precise reconstruction of the scattering angle of the protons at collision. The large absolute values of $M_{x,11}$ and $M_{x,12}$ results in a poorer resolution in the

horizontal plane [24].

2.4.5 Track Reconstruction

When a proton hits the main detectors (MDs) it will cause the scintillating fibres it traverses to light up. By detecting which fibres light up, the signals in the U- and V-plane can be combined into a signal of x- and y-coordinates in the beam coordinate system. Each MD consist of 20 layers of fibres with 10 fibres in the u-plane and 10 fibres in the v-plane which are perpendicular to the U-plane. A proton hitting a plane will traverse multiple overlapping fibres and the signals from these fibres are combined into a U or V coordinate. The principle of this is shown in fig. 21. The pattern of the staggering of the fibres improves the resolution as it narrows the overlap regions of fibres with signals. This is seen on the right hand side of fig. 21. The maximum overlap region is then used to determine the coordinate in the u and v plane. Combining the signal in the U- and V-plane, the signals are translated into x- and y-coordinates in the beam coordinate system [5].

On average an elastic event has signals in 23 fibres. Around 18-19 of these signals are due to the proton and the rest are due to noise or background events. To reduce noise there are constraints set on the number of hit fibres. If a layer has more than 10 hits, the event is discarded. For events to be approved, three or more layers are required to have between 1 and 3 hit fibres, and each of the U- and V-plane need to have a minimum of 3 overlapping fibres [5].

If more than one track are seen in an armlet, these tracks are matched with the diagonally opposite armlet signal tracks. Usually more tracks are only seen in one the armlets, and the track that does not match a track in the opposite detectors is discarded. These tracks are mostly due to beam halo particles. If there are multiple elastic events in both detector arms, the tracks that matches each other best are used [5].

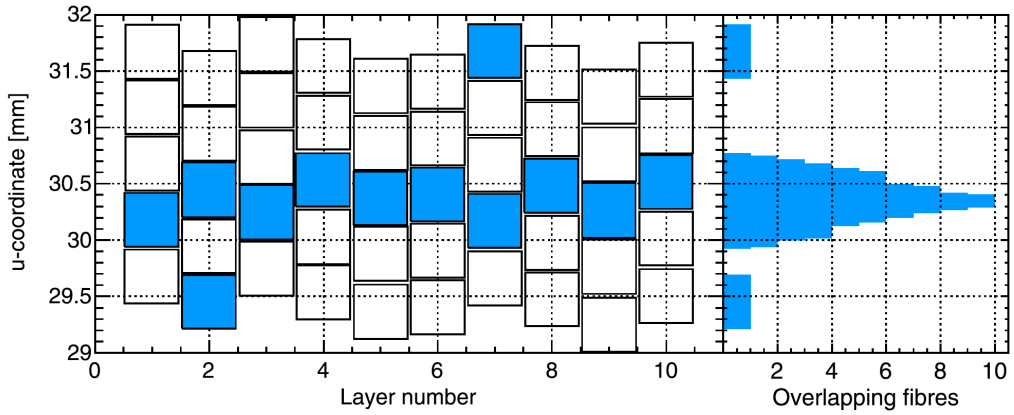

Figure 21: Hit pattern of a proton traversing the scintillating fibres in the U-plane [5].

2.4.6 Run Conditions

During run 363461 certain conditions are monitored throughout. These conditions are important to know when simulating the data taken in this particular run.

Beam conditions

The luminosity is measured during LHC runs with multiple detectors and software, e.g. a Cherenkov integration detector (LUCID), the inner detector of ATLAS, and the Beam Conditions Monitor (BCM). The preliminary integrated luminosity for run 363461 is measured to be $90.2\,\mu b^{-1}$. this measurement has to be calibrated by Van der Meer scans, which measures the absolute luminosity [24].

The emittance was monitored by Beam Synchrotron Radiation Systems (BSRT) and wire scans. The wire scans are used to calibrate the BSRTs in the beginning of LHC runs [5]. During a data taking run the protons bunches and thereby the emittance grow due to internal interactions in the bunches. The evolution of the emittance is exponential of the form $\epsilon(t) = C - a\exp(\tau \cdot t)$, where C is an offset determined by wire scans, and the parameters, a and τ,

of the exponential evolution, is determined by the BSRT measurements. This evolution is later used for the event generation in the Monte Carlo simulation [24].

Detector Status

The conditions and performance of the detectors are of great importance to the ALFA analysis of elastic physics. The performance of the detectors ultimately determines the efficiency and resolution of the ALFA measurements. During data taking the detectors are monitored to make sure the detectors are functioning properly and that the data is of high quality.

One of the crucial parameters of track reconstruction and resolution is the number of overlapping fibres hit in the detectors. In fig. 21 an event with 10 overlapping fibres in the U-plane is shown. This results in a narrow signal with great resolution in the U-plane, and this is of course desirable. From fig. 22 it is seen how many overlapping layers that are hit during the triggered elastic events of run 363461. In the optimal case all the events would have 10 overlapping fibres in both the U- and V-plane, resulting in strong narrow signals in the upper right corners of the distributions in fig. 22. All detectors show close to optimal signals in all detectors despite B7L1U and B7R1L, where the distributions peak around 9 overlapping layers in both the U- and V-plane, as can be seen in fig. 22a and fig. 22h.

Before the 900 GeV elastic physics run two previous runs at ALFA had already taking place, one at 8 TeV and one at 13 TeV [19][22]. During these runs the ALFA detectors were exposed to a lot of radiation, which in the long run damages the detectors. This could be the reason for this small deficiency in detector B7L1U and B7R1L. Previous to the 900 GeV campaign the detector signals were optimized to some degree to catch most of the signal, however a more thorough optimization could be carried out [24].

The efficiency of the detector layers is shown in fig. 23. The layer efficiency is given by how often the layers contributes to an elastic event. The plots in

fig. 23 shows that most layers has an efficiency of $\sim 90\%$, however fig. 23a and fig. 23h shows several layers with efficiencies lower than 90% for the detectors B7L1U and B7R1L respectively. This correlates with the plots fig. 22a and fig. 22h where deficiencies in number of overlapping layers where seen in the same detectors.

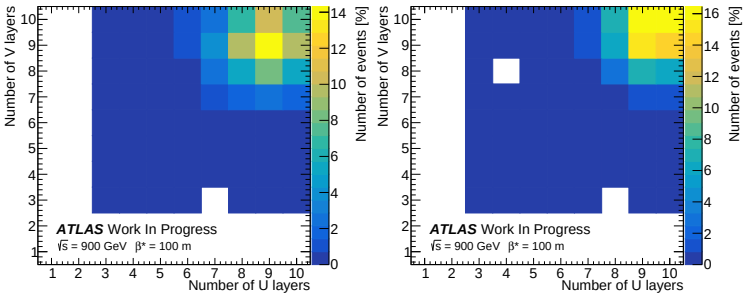

(a) B7L1U. (b) B7L1L.

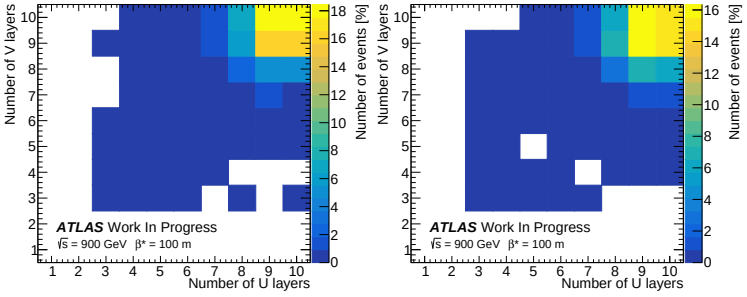

(c) A7L1U. (d) A7L1L.

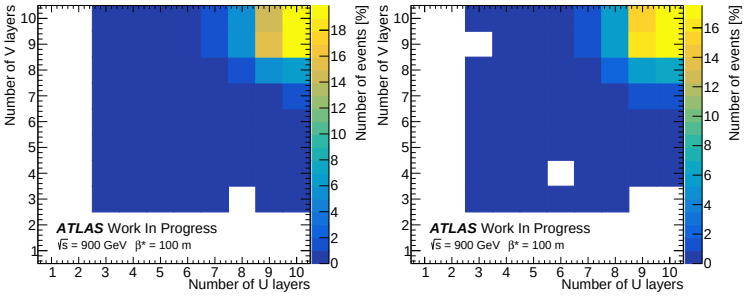

(e) A7R1U. (f) A7R1L.

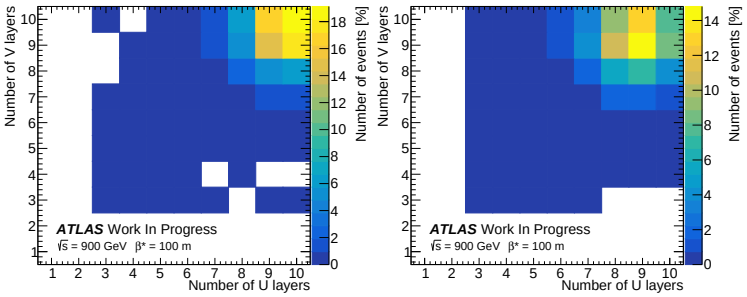

(g) B7R1U. (h) B7R1L.

Figure 22: Number of hits in overlapping fibre in the U- and V-plane for elastic events.

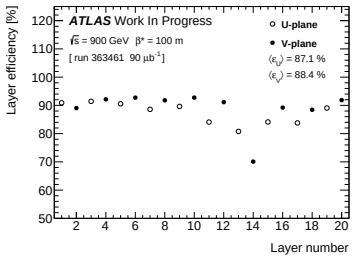

(a) B7L1U.

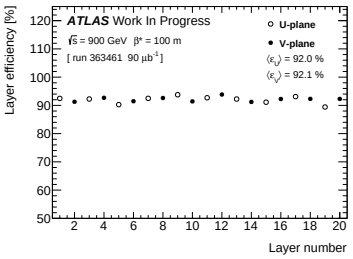

(b) B7L1L.

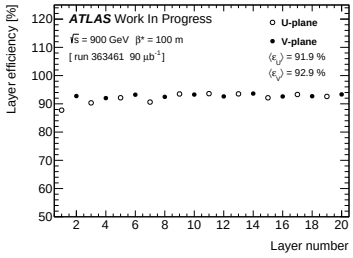

(c) A7L1U.

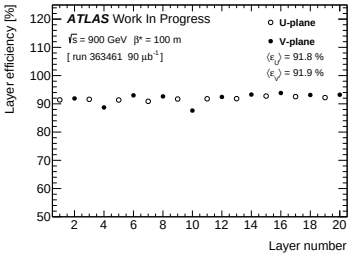

(d) A7L1L.

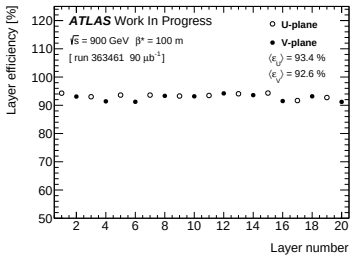

(e) A7R1U.

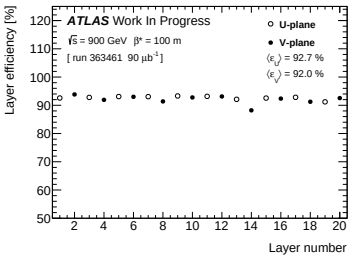

(f) A7R1L.

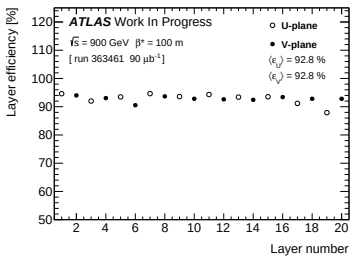

(g) B7R1U.

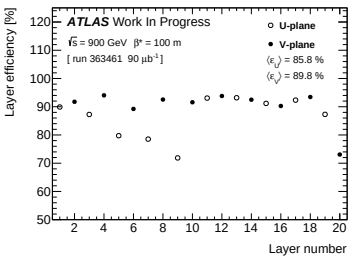

(h) B7R1L.

Figure 23: Layer efficiency for each of the 8 detectors.

3 Data Analysis

This data analysis is based on run 363462 of the elastic physics campaign with center-of-mass energy of 900 GeV and $\beta^* = 100\,\mathrm{m}$. The elastic events in this run are intended to probe the region of the Coulomb Nuclear interference of the differential cross section. During data taking a preliminary measurement of the integrated luminosity was carried out indicating an integrated luminosity of $90\,\mu\mathrm{b}^{-1}$ for the 363462 run.

ALFA is built to measure the elastic cross section of protons, by detecting elastically scattered protons at very small angles. To recognize an elastic event, the principle of momentum conservation is utilized, as this means that elastic events has an equal scattering angle for both of the outgoing protons.

The cross-section is measured by counting elastic events and reconstructing their scattering angles, and thereby the energy transfer, and then fitting the distribution of events, as a function $|t|$, with theory. The counting of events and the cross-section are related by,

$$\sigma = \frac{N_{\mathrm{tot}} - N_{bg}}{\epsilon A L} \tag{50}$$

Where N_{tot} is the total number of events, N_{bg} is the number of background events, ϵ is the detector efficiency, A is the acceptance of the detector, and L is the integrated luminosity. Other than the physical aspects of the experiment, the measurement of the cross-section also relies on the detectors performance. All these aspects of data taking has to be taking into account when analysing the data.

This analysis is based on the elastic signal simulated with a Monte Carlo (MC) simulation developed for the ALFA experiment. The purposes of the analysis is to gain a full understanding of how the elastic signal behaves according to the various experimental effects of ALFA and get an idea of how the signal of ALFA in analysed in the best way possible. There is yet to be

conducted a modelling of the background of ALFA at 900 GeV, therefore this analysis in solely based on MC simulated signal events.

The following section presents a brief description of the background sources of ALFA. Then explanation of how elastic events are selected in the offline analysis are provided, followed by a thorough study of the experimental effects of ALFA are provided. Then follows an analysis of the performance of various t-reconstruction methods, and in the end an analysis of the optimal fit procedures is provided.

The analysis is developed on the basis of an existing data analysis framework used in earlier analyses [22] [24] [19].

3.1 Selection of Events

The initial selection of events is done during data taking by the elastic triggers L1_ALFA_ELAST15 and L1_ALFA_ELAST18. Further event selections are carried out after data taking to bring down noise and background event rate. The criteria for further event selection is based on track reconstruction, trigger criteria, and geometrical cuts, and cuts based on correlations of the measurements in the different detectors. This section will cover how this event selection is carried out.

3.1.1 Track and Trigger

In fig. 21 a perfect track is depicted, with hits in 10 overlapping fibres. However, every track is not like this as the scintillating fibres do not have an efficiency of 100 % and hits in adjacent fibres may worsen the resolution. Therefore, for a track to be reconstructed, there are certain requirements.

- A track should have a minimum of 3 overlapping fibres
- At least 3 of the layers of these fibres should only have a multiple of 3 hits

- A detector must not contain a multiple of 5 additional hits that are not reconstructed into a track

The purpose of the first criterion is to reduce noise in the detector. This requirement also ensures a certain track resolution due to the 3 overlapping fibres. The second criterion reduces tracks from shower events, as shower events make it difficult to know, which track was induced by an elastic proton. The third criterion is to discard events that might have had an additional track which was not reconstructed, e.g. due to noise in the detector. The non-reconstructed track could be a proton track corresponding to a track in the opposite detectors, but as it is not reconstructed it cannot be used [19]. These criteria are for run 363461. The criteria are adjusted from run to run depending on, data quality, track reconstruction efficiency, and detector resolution.

3.1.2 Geometrical Selection Cuts

Due to the LHC beam screen and inefficiencies in the ALFA detectors, there are made geometrical selection cuts on the detectors to enhance the data quality. The two cuts applied are the beam screen cut and the edge cut. The principle of these cuts are depicted in fig. 24.

The beam screen cut is applied because of the LHC beam screen. The LHC beam has a protective screen around the beam, which is located 4 m before the inner ALFA detectors. This beam screen causes a drop in the event rate for large values of y, as particles with a large vertical angle will hit the beam screen and scatter or cause shower particles. To reduce noise arising from the beam screen a cut in the vertical coordinate is made.

Looking at fig. 25 it is clear that the event rate drop is not identical for all ALFA detectors. The inner detectors, denoted with A, are affected by the beam screen at larger y-values than the outer detectors. This is probably due to the alignment of the detectors with respect to the beam. In earlier analyses the beam screen cut has been the same for all detectors, while in this analysis the beam screen cut are made individually for all detectors. The cuts

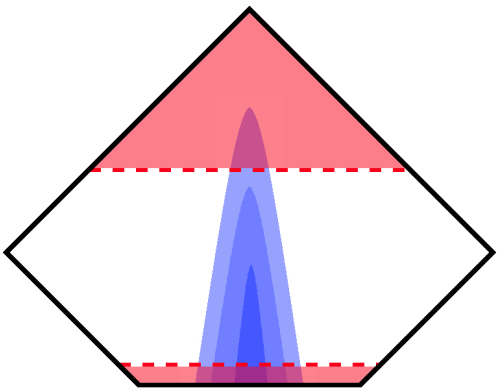

Figure 24: An illustration of a main detector with the applied beam screen cut and edge cut. The beam screen is the red region in top of the MD and the edge cut is the cut applied in the bottom of the MD. The blue area are a visualisation of where elastic protons are most likely to hit. The red and blue areas are not to scale, and are only for visualisation purposes.

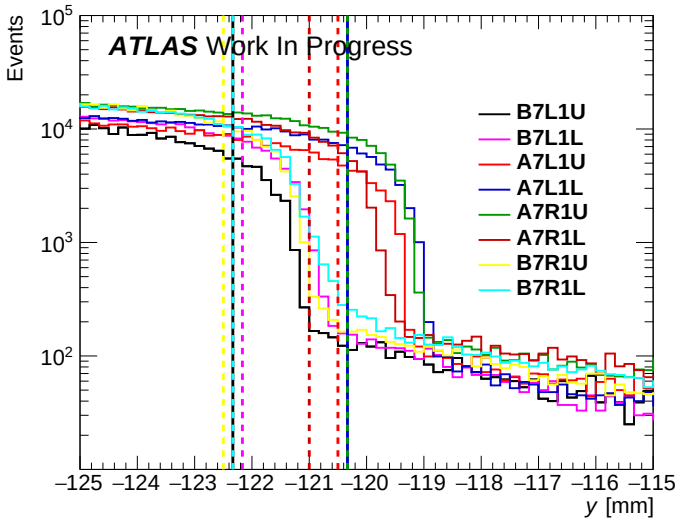

Figure 25: The event rate drop of the eight ALFA detectors. The beam screen cut is indicated by the dashed line, and the colors correspond to the detectors. B7L1U has the same cut as B7R1L and A7L1L and has the same cut as A7R1U.

Detector	Beam Screen Cut, y
B7L1U	$-122.3\,\mathrm{mm}$
B7L1L	$-122.2\,\mathrm{mm}$
A7L1U	$-120.5\,\mathrm{mm}$
A7L1L	$-120.3\,\mathrm{mm}$
A7R1U	$-120.3\,\mathrm{mm}$
A7R1L	$-121.0\,\mathrm{mm}$
B7R1U	$-122.5\,\mathrm{mm}$
B7R1L	$-122.3\,\mathrm{mm}$

Table 3: Individual beam screen cuts for each detector. All values are negative in order to be able to compare the beam screen cuts of all the detectors.

are made by finding the biggest drop in event count between two adjacent bins, and then making the cut at the y-value of the bin edge between the two bins subtracted by 1 mm. By making individual beam screen cuts for each detector more elastic events are preserved. The individual beam screen cuts are presented in table 3. Here all values are negative, as the y-coordinates of the upper detectors are made negative in order to compare all detectors in fig. 25.

An additional cut is made in the bottom of the main detectors. This cut is referred to as the edge cut. The edge cut ensures that the MD trigger tile overlaps the scintillating fibres and all active layers of the detector are traversed. The region near the detector edge is the region most sensitive to elastic protons scattered at the smallest angles. Therefore it is unfortunate that this part has to be cut of in the analysis. However it is important to ensure that the detector acceptance are uniform over the whole detector region. For this run the edge cut, cuts off the 90 µm closest to the beam [22].

3.1.3 Elastic Correlation

Elastic correlation cuts are based on the correlation between the coordinates measured in ALFA. Two elastically scattered protons are bound to have an equally large and opposite scattering angle by momentum conservation. Thus, the coordinates measured in the ALFA detectors of elastic protons are strongly correlated. By simulating signal events, these correlations on the elastic protons can be used to discard background events, which does not have the same correlations. The correlation distributions made during this analysis are listed below:

$$
\begin{aligned}
x_i^A &\quad \text{vs.} \quad x_i^C \\
x_o^A &\quad \text{vs.} \quad x_o^C \\
x_i^A &\quad \text{vs.} \quad \theta_x^A \\
x_i^C &\quad \text{vs.} \quad \theta_x^C \\
y_i^A &\quad \text{vs.} \quad y_i^C \\
y_o^A &\quad \text{vs.} \quad y_o^C \\
y_i^A &\quad \text{vs.} \quad \theta_y^A \\
y_i^C &\quad \text{vs.} \quad \theta_y^C
\end{aligned}
$$

The i/o denotes the inner/outer detector, and A/C denotes at which side of ATLAS the detector is placed. $\theta_{x/y}$ is the local angle calculated from the difference between the coordinates measured in the inner and outer detector, in an armlet, divided by the distance between the detectors.

In fig. 26a and fig. 26c the elastic selection plots of the x-coordinates measured in the inner and outer detectors are plotted, respectively. Due to conservation of energy a diagonal signal is expected, as the scattering angles must be equal. However, the diagonal signal is smeared due to divergence, beam spot width, and detector resolution, and a signal in the opposite diagonal is also seen. In fig. 26e we also expect a diagonal signal, as large absolute values of x must result in large angles in the x-plane. Again we see

a smearing of the signal and an off-diagonal signal for low absolute values of x. Elastic selection plots i the y-plane are shown in fig. 26b, fig. 26d and fig. 26f, which are diagonal as expected by the same logic as for the x-plots, but also has a smeared signal. The smearing of the signal is investigated further in section 3.4.

3.2 Background

The background events in the ALFA experiment come primarily from three sources: Beam halo particles, single diffractive (SD) events, and protons which have had a double pomeron exchange (DPE). In DPE procceses both protons emits a pomeron which then interact resulting in more outgoing particles. In these processes both protons lose momentum but survive and can be detected in the detectors as elastic events. However, these events are not elastic as energy is lost.

In single diffractive events one of the protons survive while the other protons breaks apart. These events can be detected as elastic with the surviving proton detected in one detector in coincidence with uncorrelated noise in the other detector arising from beam halo particles or other sources of detector noise.

These events have a possibility of satisfying the elastic selection trigger criteria and can be difficult to distinguish from real signal events. Thus they are inevitably present in the detector signal sample. The background should be modelled in order to be able to distinguish signal from background and get the best possible estimation of the physics parameters of the elastic cross section. For the 900 GeV elastic campaign there has not yet been conducted a modelling of the background sources.

3.3 Experimental Effects of ALFA

This section covers the various experimental effects of the ALFA experiment. The detector effects includes the acceptance, the evolution of the beam spot

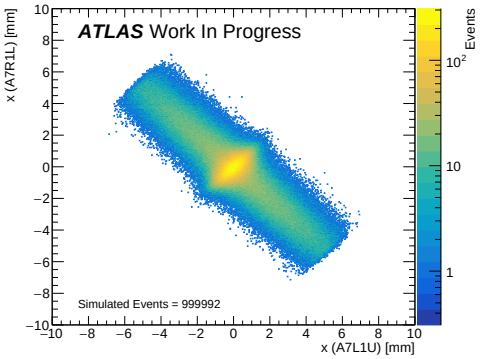

(a) x_i^A vs. x_i^C.

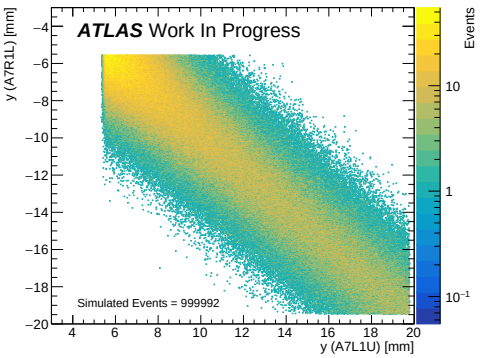

(b) y_i^A vs. y_i^C.

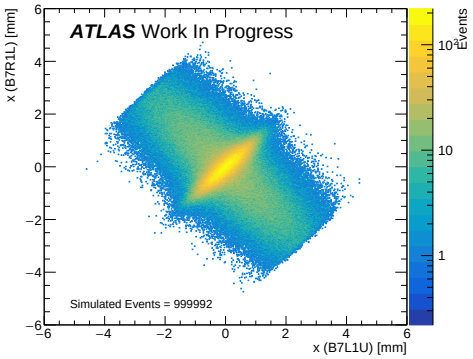

(c) x_o^A vs. x_o^C.

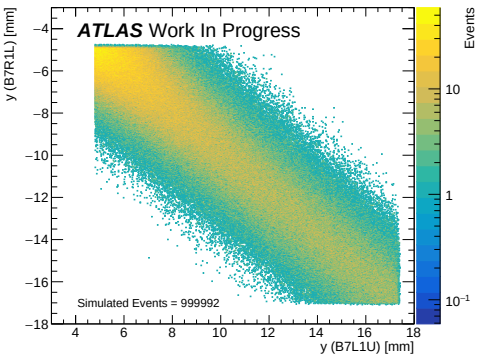

(d) y_o^A vs. y_o^C.

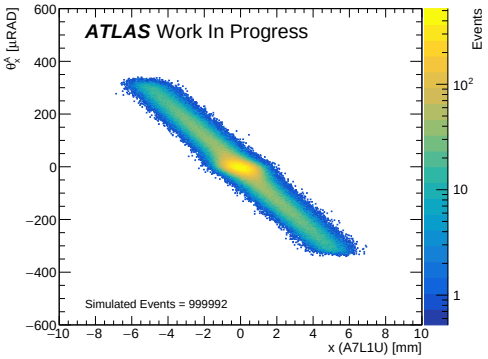

(e) x_i^A vs. θ_x^A.

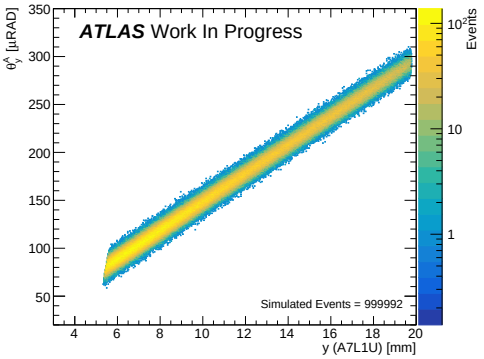

(f) y_i^A vs. θ_y^A.

Figure 26: Elastic correlation plots.

width, and the detector resolution. The acceptance is a measure of how efficient the ALFA detectors are in detecting elastic events as a function of t. The evolution of the beam spot width describes how the width of the beam grows in time between scraping blocks, and the detector resolution is how precisely the ALFA detectors are in determining the coordinates of the particles hitting the detectors.

3.3.1 Acceptance

The acceptance of the ALFA detectors are determined through simulation. The acceptance is defined as a ratio of total number of simulated events divided by the total number of accepted events. The number of accepted events is counted after the geometrical cuts and the elastic selection criteria.

The acceptance is presented in fig. 27. For small energy transfers a drop is seen around $|t| \approx 2 \cdot 10^{-3}$ due to the edge cut. The drop beyond the peak is due to the shape of the detector. The protons scatter uniformly in the azimuthal angle ϕ, and the detector covers a large range in ϕ for low scattering angles θ. Going to larger scattering angles the detectors covers a smaller part of ϕ-space, resulting in more particles missing the detectors. For the plot in fig. 27 the detector efficiency is taken to be 100%, which is not the case. Thus, a drop in efficiency is expected, while the shape of the histograms are expected to remain the same more or less.

3.3.2 Beam Spot Width

During data taking the beam halo is populated by more and more particles. This causes the beam spot width to grow over, as well as the beam positions during the data taking period might change. The interaction point (IP) is a crucial factor to where the proton ends up in the detector, and the beam spot width ultimately results in smearing of the signal.

From fig. 28a and fig. 28b it is clear that the position of the beam spot does not change dramatically throughout the run. However, as expected, the width of the beam increases throughout the data taking run as seen in

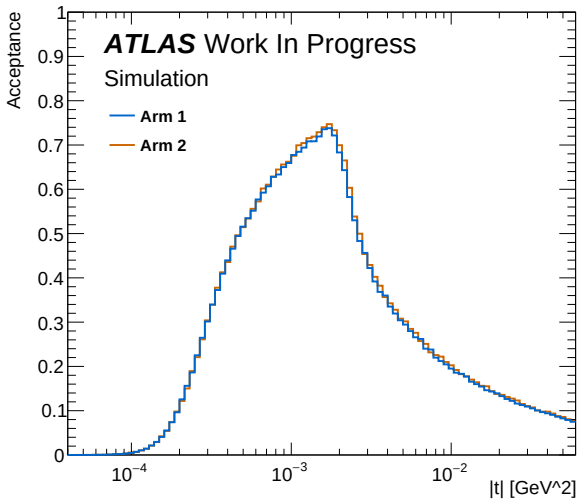

Figure 27: Acceptance for events in arm 1 and 2. This plot is done with 100% detector efficiency.

fig. 28c and fig. 28d. The measurements in fig. 28 are from the inner detector of ATLAS. The inner detector of ATLAS was not turned on throughout the entire run, hence not all lumiblocks has a measurement of the beam properties in these plots.

The evolution of the beam is furthermore measured by BSRTs. These measurements are normalized by wire scans and are presented in fig. 29. When simulating the experiment the measurements are fitted by exponential functions, which are then used to simulate the evolution of the emittance. The emittance is crucial knowledge as both the beam spot width and the divergence are dependent of the emittance. As divergence smears out the scattering angle it is an important factor to include in the simulation, to resemble the actual data as much as possible. The beam spot width has a big impact as well, although mostly in the x-plane as parallel-to-point optics ensures that all particles scattered with the same vertical angle ends up at the same position in y in the detectors.

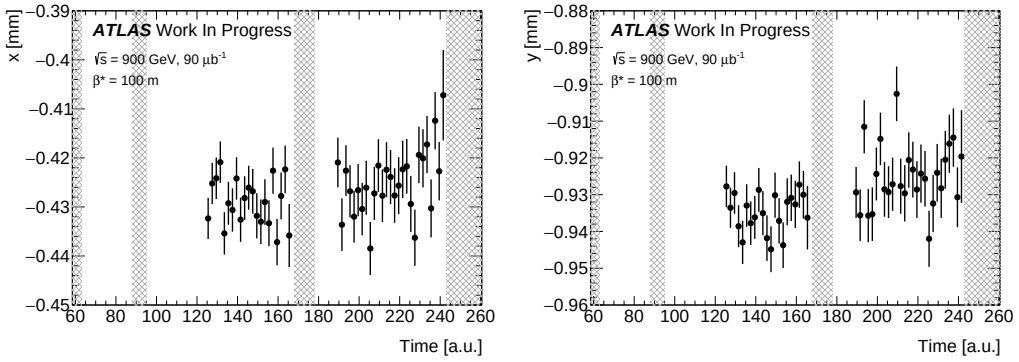

(a) Beam spot position in x.

(b) Beam spot position in y.

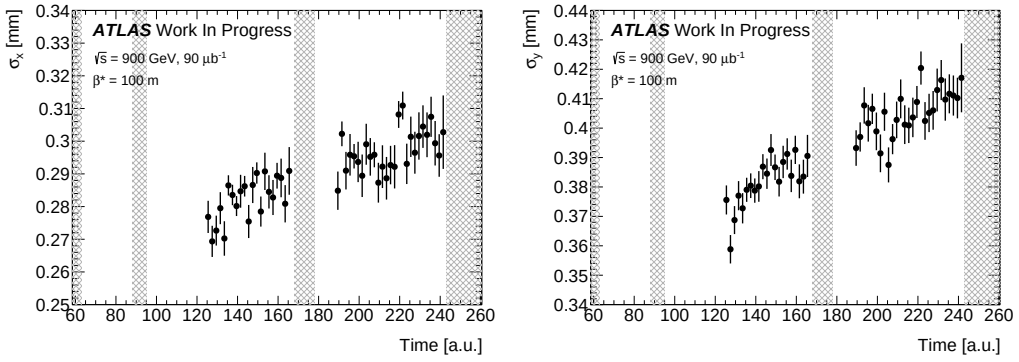

(c) Beam spot width in x.

(d) Beam spot width in y.

Figure 28: The position and width of the beam as a function of time given by LB number during run 363461. The grey regions are scraping blocks. The beam spot position and width are measured by the ATLAS inner detector.

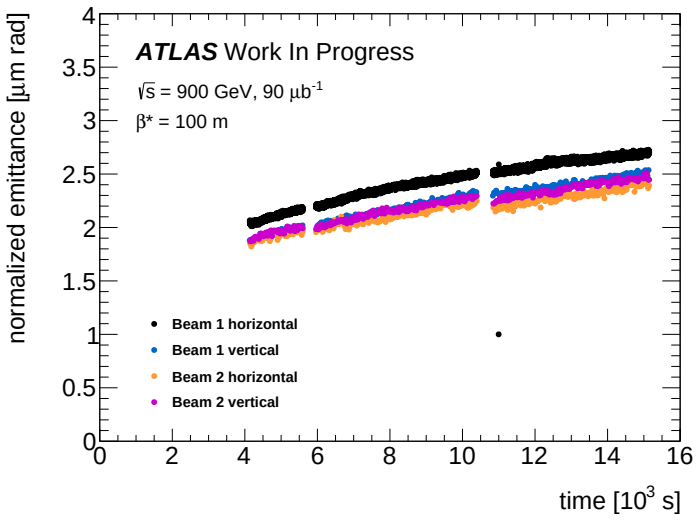

Figure 29: Normalized emittance as function of time. The emittance determined from BSRT measurements and normalized by the wire scans.

3.3.3 Detector Resolution

The detector resolution is determined by two factors: The resolution of the detectors, due to the staggering of the scintillating fibres, and multiple scattering. Multiple scattering arises from the protons traversing the first detector, from where the scattering angle is changed slightly, due to many small angle deflections in the detector material. Due to the central limit theory the sum of the many small angle scatters are Gaussian distributed with an width of [15]

$$\theta_0 = \frac{13.6\,\mathrm{MeV}}{\beta cp} z \sqrt{\frac{x}{X_0}} \left[1 + 0.088 \ln\left(\frac{x}{X_0}\right)\right] \tag{51}$$

where βc, is the velocity of the particle, p is the momentum, z is the charge number, and x/X_0 is the thickness of the traversed material in terms of scattering length. All protons leaving the inner detector picks up an additional error of θ_0 due to multiple scattering, which results in a poorer resolution of the outer detectors compared to the inner detector. The resulting multiple scattering error is given by [15]

$$\sigma_{MS} = \frac{1}{\sqrt{3}} x\theta_0 \tag{52}$$

As θ_0 is inversely proportional to the momentum of the particles, it is clear that multiple scattering has a larger effect on the convoluted error of the ALFA experiment done with a center-of-mass energy of 900 GeV compared to the experiment done with a center-of-mass 8 TeV. From the error calculated for 8 TeV the multiple scattering error can be estimated by

$$\sigma_{MS,900\,\mathrm{GeV}} = \frac{8\,\mathrm{TeV}}{900\,\mathrm{GeV}} \sigma_{MS,8\,\mathrm{TeV}}$$

The convoluted error of the 8 TeV run is measured to be around 42 µm [22]. The data taken in the 900 GeV campaign reveals a resolution of 100 µm. This is seen in fig. 30 where the residuals of the predicted y-values and measured y-values are plotted and fitted by a Gaussian. The width of the fitted Gaussian reveals a convoluted resolution of 100 µm for all armlets. Assuming that the detectors are in same condition for the two runs and the fact that multiple scattering scales inversely with momentum it can be written that

$$\sigma_{8\,\mathrm{TeV}} = \sqrt{2\sigma_{Det}^2 + \sigma_{MS,8\,\mathrm{TeV}}^2} = 42\,\mu\mathrm{m} \tag{53}$$

$$\sigma_{900\,\mathrm{GeV}} = \sqrt{2\sigma_{Det}^2 + \sigma_{MS,900\,\mathrm{GeV}}^2} = 100\,\mu\mathrm{m} \tag{54}$$

$$\sigma_{900\,\mathrm{GeV}} = \sqrt{2\sigma_{Det}^2 + \left(\sigma_{MS,8\,\mathrm{TeV}} \frac{8\,\mathrm{TeV}}{900\,\mathrm{GeV}}\right)^2} = 100\,\mu\mathrm{m} \tag{55}$$

Combining eq. (53) and eq. (55), $\sigma_{MS,8\,\mathrm{TeV}}$ and σ_{Det} is determined to

$$\begin{aligned} \sigma_{MS,8\,\mathrm{TeV}} &\approx 10\,\mu\mathrm{m} \\ \sigma_{MS,900\,\mathrm{GeV}} &\approx 10\,\mu\mathrm{m} \frac{8\,\mathrm{TeV}}{900\,\mathrm{GeV}} \approx 90\,\mu\mathrm{m} \\ \sigma_{Det} &\approx 29\,\mu\mathrm{m} \end{aligned}$$

Thus, with multiple scattering the detector resolution, σ_{Det}, is determined to be around 29 µm. This is consistent with what it was measured to be in preliminary test [22], meaning that multiple scattering is a valid explanation to the poor resolution of the data in the 900 GeV campaign.

The resolution measured in fig. 30 is measured from the y-coordinates. Due to the symmetry of the detector and multiple scattering in the x- and y-plane, it is expected that the resolution of the x-plane is equal to that of the y-plane.

3.4 Simulation

This section describes the simulation of the ALFA experiment, followed by a study of how the various experimental effects influences the signal.

In order to study the ALFA experiment thoroughly, a simulation is build to model every aspect of the experiment, which is tweaked in order for the simulated data to resemble the actual data as much as possible.

Every elastic event in the simulation is created with a value of t from the theory describing the expected distribution of t depicted in fig. 6. As the scattered protons are uniformly distributed in the azimuthal plane, ϕ, every event is assigned a random value of ϕ between $-\pi$ and π.

With the emittance estimated from data, t and ϕ are used to calculate an interaction point (IP) and an initial scattering angle. A divergence term is then added to the scattering angle of the event.

From the IP the events are transported to the detectors via the transport matrices given in table 2. After checking whether the events hit the detectors, the events are smeared according to the detector resolution. The inner detectors are smeared by $\sigma_{Det} = 30$ µm and the outer detectors has additional smearing according to multiple scattering of $\sigma_{900\,\mathrm{GeV}} = \sqrt{2\sigma_{Det} + \sigma^2_{MS,900\,\mathrm{GeV}}} \approx 95$ µm.

During the data taking period of ALFA the data taking is monitored as

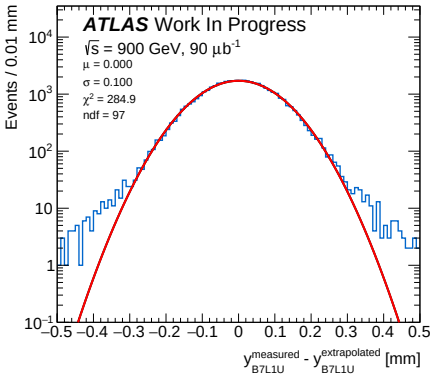

(a) Detector resolution of B7L1U.

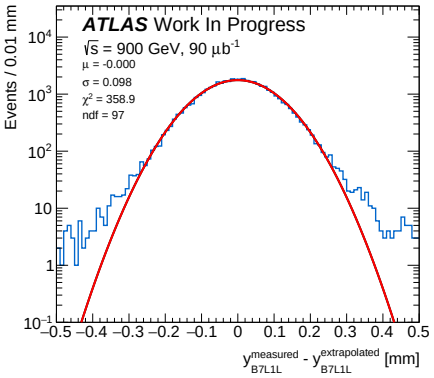

(b) Detector resolution of B7L1L.

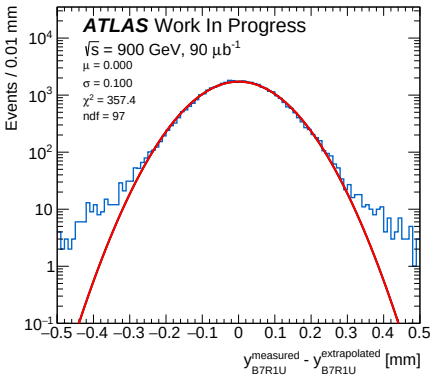

(c) Detector resolution of B7R1U.

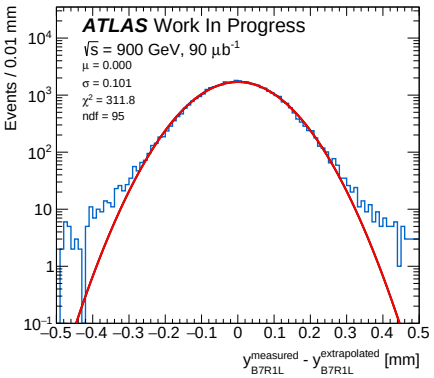

(d) Detector resolution of B7R1L.

Figure 30: The residuals of the predicted and the measured y-coordinates of the four outer detectors. The residuals are fitted by Gaussians revealing a convoluted error for all the detectors of $\approx 100\,\mu\text{m}$.

described in section 2.4.2 and section 2.4.3. Through the data collected in monitoring, the data is split into super lumiblocks (SLBs). A super lumiblock is a period of 10 lumiblocks, where the background level and the beam properties are approximately constant.

The number of simulated events in each SLB are then scaled to match the ratio between the number of detected events in the SLBs according to data. The events of each SLB are then generated with the beam properties estimated from data monitoring.

The Monte Carlo simulation used for this analysis has generated events in the $|t|$-range from $4 \cdot 10^{-5}\,\mathrm{GeV}^2$ to $6 \cdot 10^{-2}\,\mathrm{GeV}^2$, with the theory parameters $\rho = 0.1$, $\sigma_{\mathrm{tot}} = 68\,\mathrm{mb}$, $B = 16\,\mathrm{GeV}^{-2}$.

3.4.1 Elastic Selection

The selection of elastic events are done on the basis of the elastic correlations of the simulated signal as described in section 3.1.3. The principle of energy conservation sets constraints of how elastic scattered protons behave and are seen in the detectors, and these correlations are then utilized to discard event that does not behave accordingly.

The elastic selection cuts are presented in fig. 31. The distributions $x^A_{i/o}$ vs. $x^C_{i/o}$ and $x_i^{A/C}$ vs. $\theta_x^{A/C}$ for both detector arms are fitted by two 2-dimensional Gaussian functions of the form

$$\begin{aligned} f(x,y) = A\exp\Big[-\Big(a_B(x-x_0)^2 + 2b_B(x-x_0)(y-y_0) + c_B(x-x_0)^2\Big)\Big] \\ + B\exp\Big[-\Big(a_R(x-x_0)^2 + 2b_R(x-x_0)(y-y_0) + c_R(x-x_0)^2\Big)\Big] \end{aligned} \tag{56}$$

with

$$a_1 = \frac{\cos^2\theta}{2\sigma_{x_B}^2} - \frac{\sin^2\theta}{2\sigma_{y_B}^2}, \quad a_2 = \frac{\cos^2(\theta-\delta\theta)}{2\sigma_{x_R}^2} - \frac{\sin^2(\theta-\delta\theta)}{2\sigma_{y_R}^2}$$
$$b_1 = \frac{\sin 2\theta}{4\sigma_{x_B}^2} + \frac{\sin 2\theta}{4\sigma_{y_B}^2}, \quad b_2 = \frac{\sin 2(\theta-\delta\theta)}{4\sigma_{x_R}^2} + \frac{\sin 2(\theta-\delta\theta)}{4\sigma_{y_R}^2}$$
$$c_1 = \frac{\sin^2\theta}{2\sigma_{x_B}^2} - \frac{\cos^2\theta}{2\sigma_{y_B}^2}, \quad c_2 = \frac{\sin^2(\theta-\delta\theta)}{2\sigma_{x_R}^2} - \frac{\cos^2(\theta-\delta\theta)}{2\sigma_{y_R}^2}$$

$\sigma_{x/y_{B/R}}$ is the width of the ellipse, where B/R denotes the black and red ellipse seen on the fits of the x-plane in fig. 31. θ describes the rotation of the ellipses and $\delta\theta$ describes the angle between the two ellipses. The ellipses are both set to be centered in the same point.

First the ellipses are fitted with the whole function, then the center and the angles are fixed to the fitted values. Now the widths σ_{x/y_B} are fitted again while subtracting the signal described by the red ellipse from the total underlying distribution. Afterwards the widths σ_{x/y_B} are fitted while subtracting the signal described by the black ellipse from the total distribution. By then it is assured that the large diagonal signal is fitted without taking the signal of the red ellipse into account, and then the small ellipse are fitted by the red function without seeing the large underlying signal of the black ellipse.

The $y_{i/o}^A$ vs. $y_{i/o}^C$ are fitted by a straight lines with the slope fixed to -1. The slope is fixed to -1 as the signal is known to be diagonal in the beam coordinate system. After fitting the straight line, the distribution is projected onto a plane orthogonal to the line, and fitted with a Gaussian to get the with of the diagonal signal. The fit procedure of y_i^A vs. θ_y^A is the same as for the $y_{i/o}^A$ vs. $y_{i/o}^C$ plot, though with the slope not being fixed to -1.

The elastic selection cuts are made by excluding points lying outside 3 standard deviations of the fitted widths, indicated by the ellipses on the plots in x, and lines on the plots in y. When discarding the points lying outside the ellipses, or lines, 98% of the elastic events are preserved.

The elastic selection fits shown in fig. 31 are all signal distributions for

arm 1 and for the local angle on the A-side. Due to the symmetrical nature of elastic scattering in the ϕ plane, the signal in arm 1 and 2, and on the A-side and C-side, are close to identical. Elastic cuts are also done for arm 2 and the C-side and can be seen in section C.1.

3.4.2 Beam Spot Width

The simulation enables a study of how the signal data are affected by the beam spot width (BSW), the divergence, and the detector resolution. The width of the beam spot has an affect on the output signal of the x plots, this is seen in fig. 32 and fig. 33 where the signal smears out for both the x_i^A vs. x_i^C and x_i^A vs. θ_x^A distributions when the beam spot width increases. However, looking at the plots in fig. 34 there is no noticeable difference between small beam spot width and large beam spot widths, for the elastic correlation distributions in the y-plane. The parallel-to-point optics ensures that particles with the same scattering angle in y end up at the same vertical coordinate in the detector. Thus, it is expected that the width of the beam spot do not have an impact on the signal in the y-plane.

The plots of fig. 32, fig. 33, fig. 34 are all distributions of the signal in arm 1, and the distributions of the local angles are only presented for the A-side. Due to the symmetric nature of elastic scattering the same behavior of the signal as the BSW is varied, is seen for arm 2 and for the local angle on the C-side. This is presented in section C.2.

In fig. 35 the width of the fitted ellipses and the angle between the ellipses are plotted as functions of the nominal beam spot width. In fig. 35a it is seen that the width of the black ellipse scales roughly linearly with the BSW. The same goes for the red ellipse, shown in fig. 35c. However, fig. 35e the angle between the ellipses does not change as a function of the BSW. The outlier in fig. 35e can be explained by looking at fig. 32b where the red ellipse are seen to be roughly circular, thus making the angle an irrelevant fit parameter for the red ellipse in the x_i^A vs. x_i^C distribution fit for 1/2 of the nominal BSW.

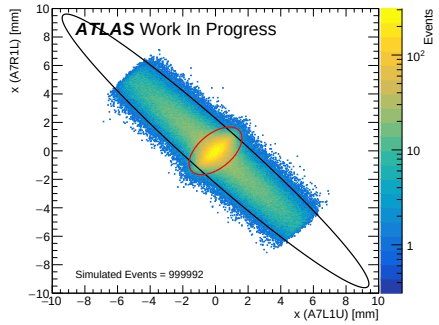

(a) x_i^A vs. x_i^C.

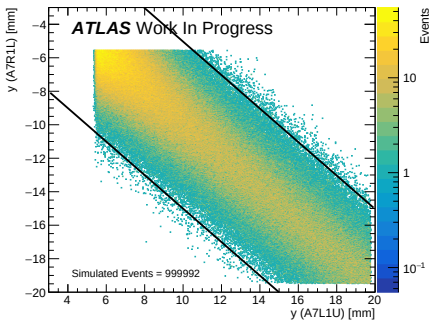

(b) y_i^A vs. y_i^C.

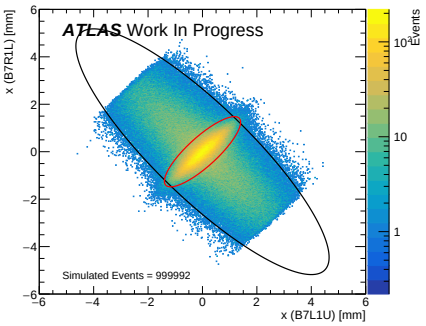

(c) x_o^A vs. x_o^C.

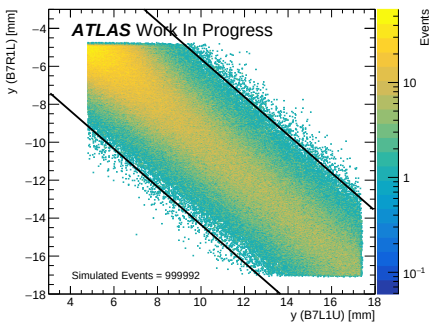

(d) y_o^A vs. y_o^C.

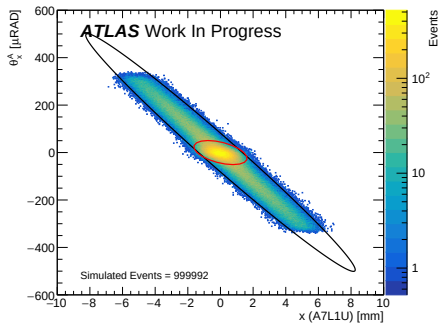

(e) x_i^A vs. θ_x^A.

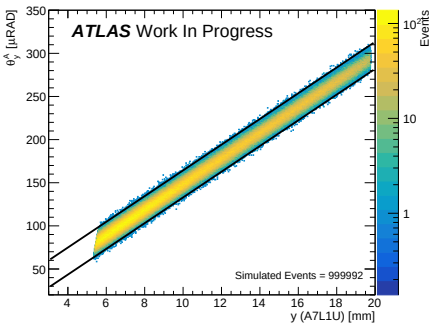

(f) y_i^A vs. θ_y^A.

Figure 31: Elastic selection correlation fits. The x-plots are fitted with two ellipses. The y-plots are fitted with straight lines, and the width is fitted by projection the points onto a plane, orthogonal to the line, which is then fitted with a Gaussian. All plots are signal from arm 1.

The width of the ellipses fitting the x_i^A vs. θ_x^A distributions also increases roughly linearly as the BSW increases, which is shown by the linear fits in fig. 35b and fig. 35d. fig. 35f shows that there is no notable change in the angle between the ellipses as functions of BSW.

The linear dependence in shown in fig. 35a, fig. 35b, fig. 35c, and fig. 35d can possibly be utilized for determination of the beam spot width of the beam by fitting the signal distribution of actual data.

In fig. 36 the widths of the signal of the of the y_i^A vs y_i^C and y_i^A vs θ_y^A distributions as functions of the BSW is presented. The width of the signal of the y_i^A vs y_i^C distributions is shown to be constant as a function of the BSW, in fig. 36a. However, in fig. 36b an increase in width is seen as the BSW grows, although the increase of signal width is small, which is why it is difficult to see in fig. 34.

3.4.3 Divergence

As the beam has a certain emittance, the incoming angle of the protons are not known precisely, as the protons are allowed to have an angle inside the beam due to the betatron oscillations. This angle is called the divergence and it is a source of smearing of the signal measured in ALFA. In the simulation the scattering angles are estimated by adding an additional random divergence term to the scattering angle, which allows us to study how the signal is affected by the divergence.

The study of the divergence is done on signal distributions of the inner detectors and the local angle on the A-side in arm 1. This is done because the signal in the inner and outer detectors behaves the same, while the symmetry of elastic scattering results in the signal on either side and arm of the detectors are equivalent. The distributions with varying divergence in the outer detectors, and on the C-side, and the distributions of arm 2 can be seen in section C.3.

In fig. 37 it is seen that the divergence is the main cause of the smearing

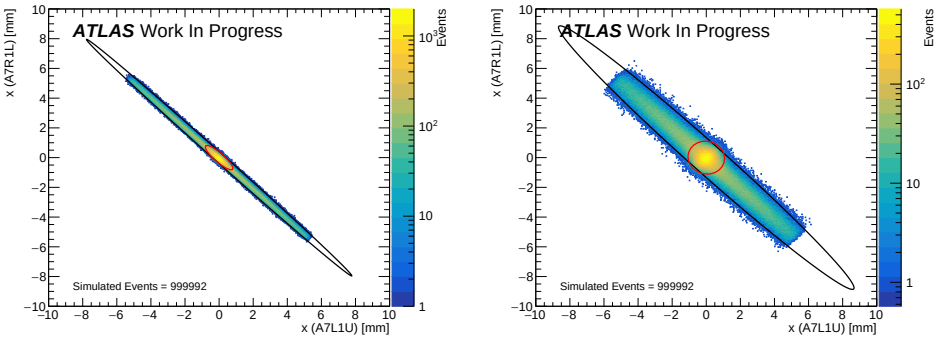

(a) No beam spot width.

(b) 2/4 of nominal BSW.

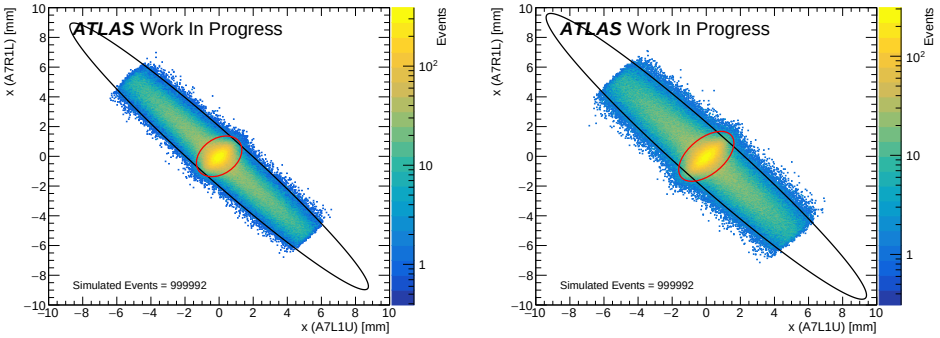

(c) 3/4 of nominal BSW.

(d) Nominal BSW.

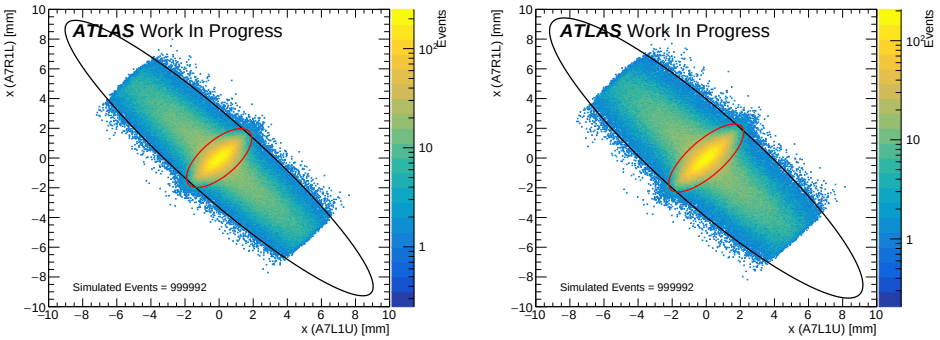

(e) 5/4 of nominal BSW.

(f) 6/4 of nominal BSW.

Figure 32: Distributions of x_i^A vs. x_i^C, generated with varying fractions of nominal beam spot width. With nominal divergence and detector smearing applied.

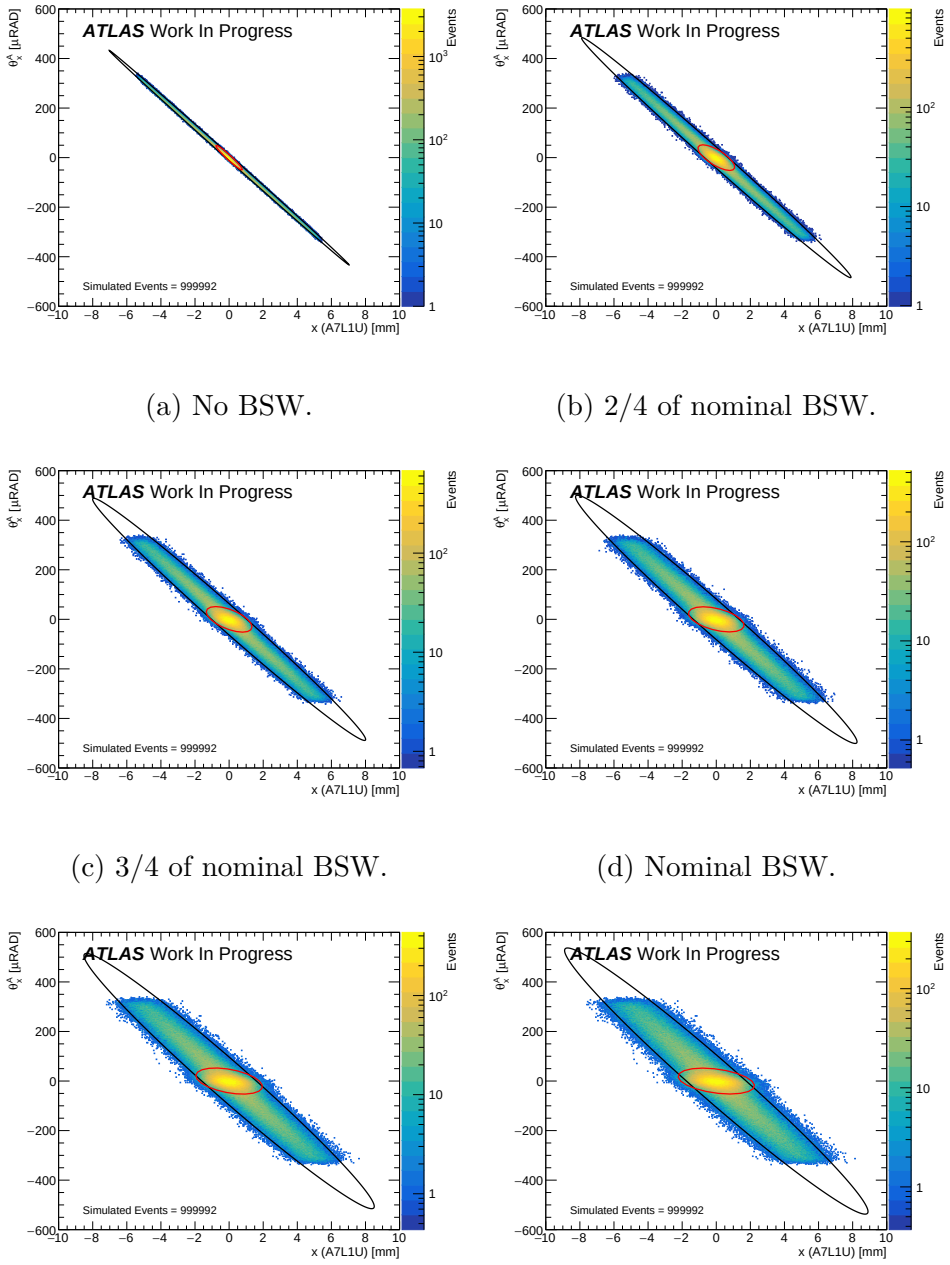

(a) No BSW.

(b) 2/4 of nominal BSW.

(c) 3/4 of nominal BSW.

(d) Nominal BSW.

(e) 5/4 of nominal BSW.

(f) 6/4 of nominal BSW.

Figure 33: Distributions of x_i^A vs. θ_x^A, generated with varying fractions of nominal beam spot width. With nominal divergence and detector smearing applied.

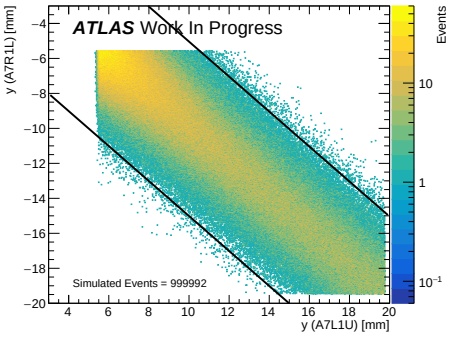

(a) y_i^A vs. y_i^C. 2/4 of nominal BSW.

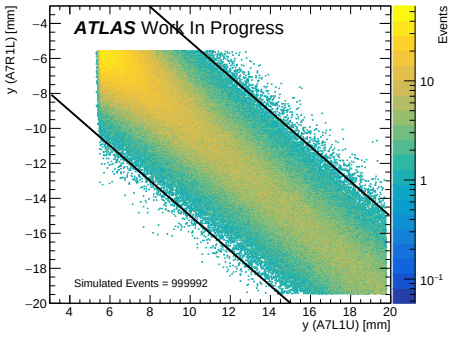

(b) y_i^A vs. y_i^C. 6/4 of nominal BSW.

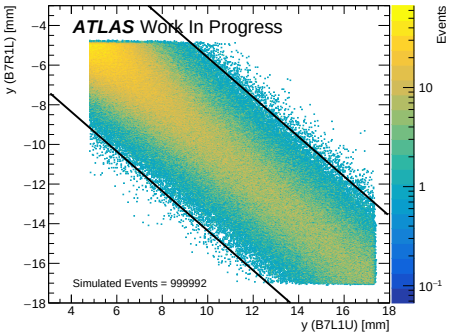

(c) y_o^A vs. y_o^C. 2/4 of nominal BSW.

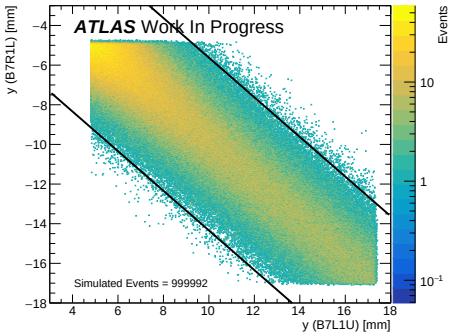

(d) y_o^A vs. y_o^C. 6/4 of nominal BSW.

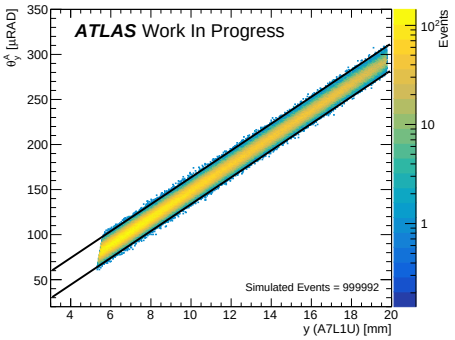

(e) y_i^A vs. θ_y^A. 2/4 of nominal BSW.

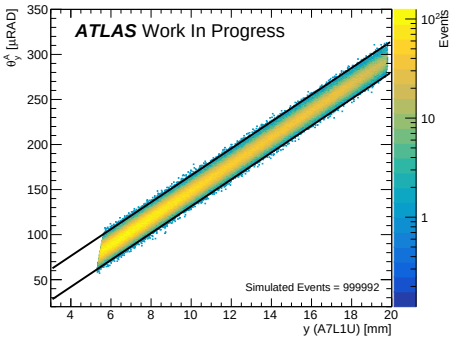

(f) y_i^A vs. θ_y^A. 6/4 of nominal BSW.

Figure 34: Distributions of y_i^A vs. y_i^C, y_o^A vs. y_o^C, and y_i^A vs. θ_y^A, with 2/4 and 6/4 of nominal beam spot width. With nominal divergence and detector smearing applied in all plots.

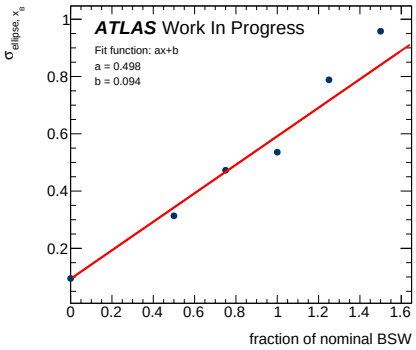

(a) x_i^A vs. x_i^C fit: σ_{x_B}.

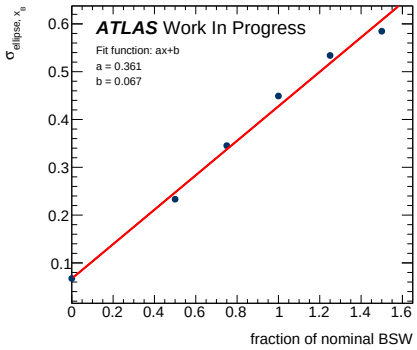

(b) x_i^A vs. θ_x^A fit: σ_{x_B}.

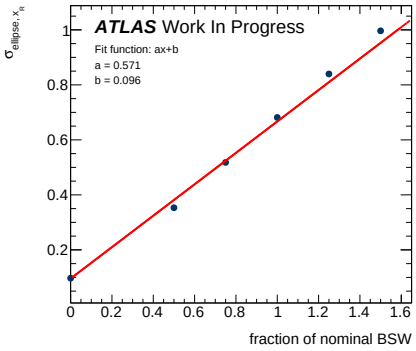

(c) x_i^A vs. x_i^C fit: σ_{x_R}.

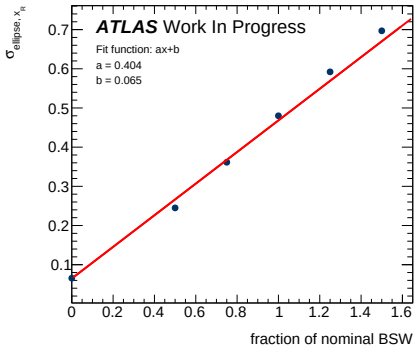

(d) x_i^A vs. θ_x^A fit: σ_{x_R}

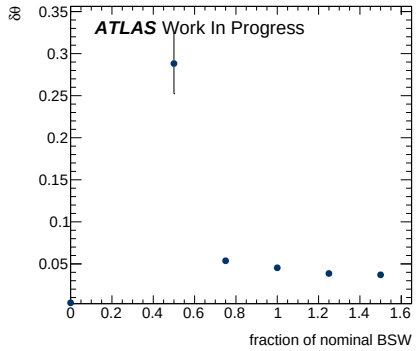

(e) x_i^A vs. x_i^C fit: $\delta\theta$

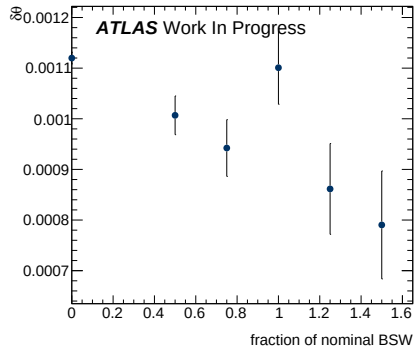

(f) x_i^A vs. θ_x^A fit: $\delta\theta$

Figure 35: The evolution of σ_{x_B}, σ_{x_R}, and $\delta\theta$ as functions of nominal beam spot width, for the fits of the x_i^A vs x_i^C distributions and x_i^A vs θ_x^A distributions.

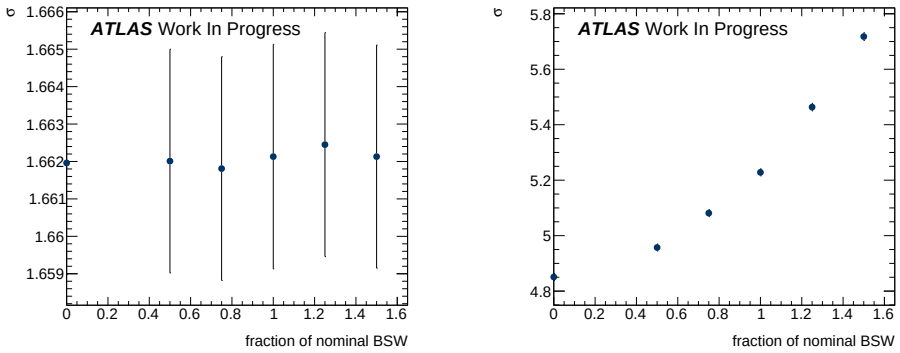

(a) y_i^A vs. y_i^C fit: σ (b) y_i^A vs. θ_y^A fit: σ

Figure 36: The evolution of the width of the signal, σ, as functions of the fraction of the nominal BSW, of the y_i^A vs. y_i^C and y_i^A vs. θ_y^A distributions.

of the signal in the $y_{i/o}^A$ vs. $y_{i/o}^C$ distributions. The protons that scatter elastically both with an incoming angle of 0, will scatter back to back with the same outgoing angles and will result in a signal on the diagonal in the plots of fig. 37. The divergence results in the protons protons not necessarily having the same incoming angle, which causes a lot of the events to not have back-to-back scattering angles, thus smearing out the signal in fig. 37. The correlation between the width of the signal of the y_i^A vs. y_i^C distributions and the fraction of nominal divergence is plotted in fig. 39a, which reveals a close to linear correlation. This correlation could be used, together with other measurements, to determine the divergence of the elastic events in data.

The signal is extremely narrow with no divergence, shown in fig. 37a. As the distributions are plotted with nominal BSW and detector smearing it shows that tells us that the main cause of smearing is the divergence and that the BSW and detector smearing almost has no effect, as the signal is extremely narrow with no divergence. This is backed up by what we saw for the BSW in the previous section.

The divergence seems to have little, if any, effect on the plots in the x-plane and neither on the $y_i^{A/C}$ vs $\theta_y^{A/C}$ distributions. This is shown in the plots

presented in fig. 38. The small effect in the x-plane can be explained by the optics of the 900 GeV elastic run. The transport matrix element M_{12} is small for all detectors in the x-plane and from Hill's equation eq. (36) it is seen that matrix element M_{12} governs the influence of the scattering angle on the resulting coordinate measured in the detectors. As the divergence affects the scattering angles, the small values of M_{12} in the x-plane, suppresses the affect of the divergence in the x-plane. This also means, that the large values of M_{12} in the y-plane results in a huge affect of the divergence of the measured y-coordinates in the detectors, which is what is seen in fig. 37.

The signal in the $y_i^{A/C}$ vs $\theta_y^{A/C}$ distributions does not smear out when going up in divergence, as shown in fig. 39b where the width of the signal of the y_i^A vs θ_y^A distribution is plotted as a function of divergence. This is because these plots are only made with coordinates in one side of the detector. The divergence has an affect on the back-to-back scattering angles of the two protons, as it is not certain that the protons collide with an incoming angle of 0. Hence, the divergence does not affect the correlations between the local scattering angles in y and the y-coordinate of the inner detector, as the protons with the same outgoing angle, regardless of the incoming angle, will end up at the same y-coordinate in the detector. The only effect is that there due to divergence are more protons at higher values of y, seen by a longer yellow center in the middle of the signal in fig. 38f. We also see a small enlargement of the signal in the center of the x_i^A vs θ_x^A distribution, x.

3.4.4 Detector Smearing

Detector smearing is the smearing of the signal due to the resolution of the detectors and multiple scattering. The convoluted resolution is 100 µm according to the fits in fig. 30. The inner detectors has a resolution of ~ 29 µm and the outer detectors has a resolution of $\sigma_{out} = 94.5$ µm. The effect of detector smearing is visualized in fig. 40 where the correlations of the outer detectors are plotted as it is in these where we expect to see the largest effect of the detector resolution. The correlation plots of x_o^A vs. x_o^C and y_o^A vs. y_o^C

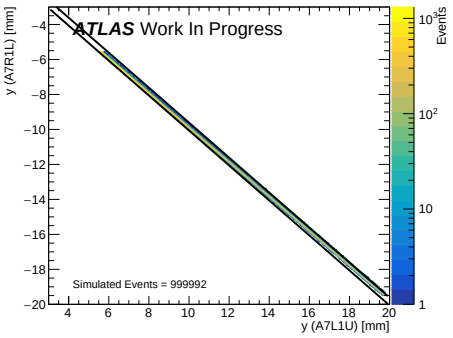

(a) No divergence.

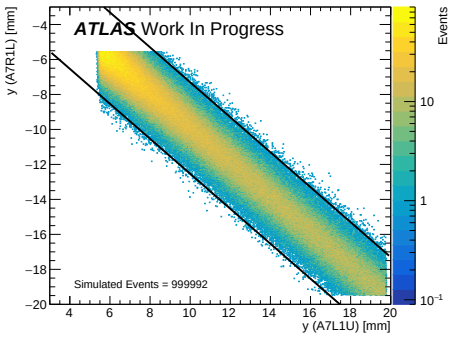

(b) 2/4 of nominal divergence.

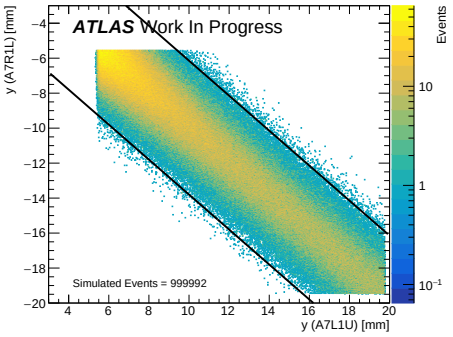

(c) 3/4 of nominal divergence.

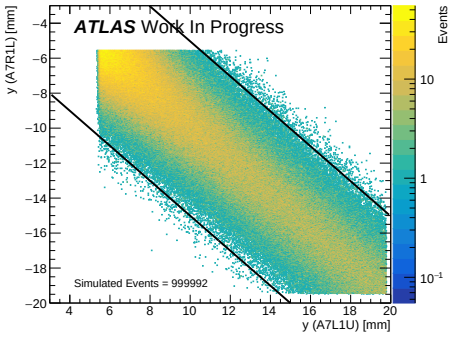

(d) Nominal divergence.

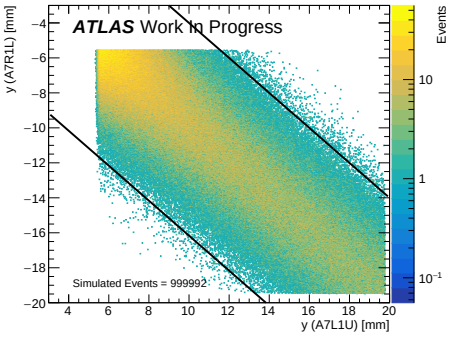

(e) 5/4 of nominal divergence.

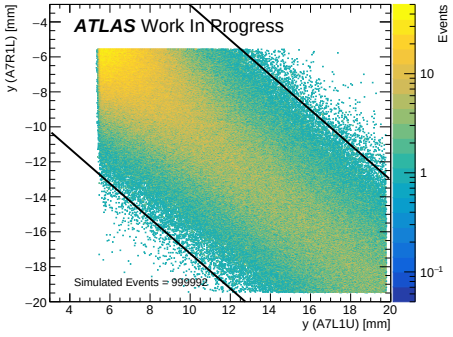

(f) 6/4 of nominal divergence.

Figure 37: Distributions of y_i^A vs. y_i^C, generated at different fractions of nominal divergence. With nominal BSW and detector smearing applied.

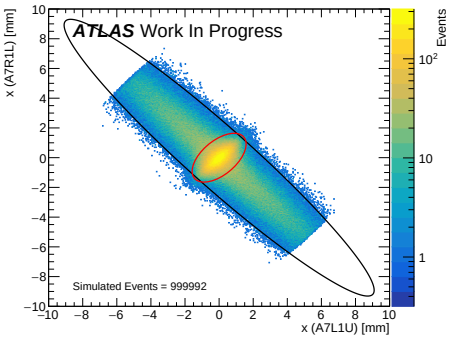

(a) x_i^A vs. x_i^C. 0 divergence.

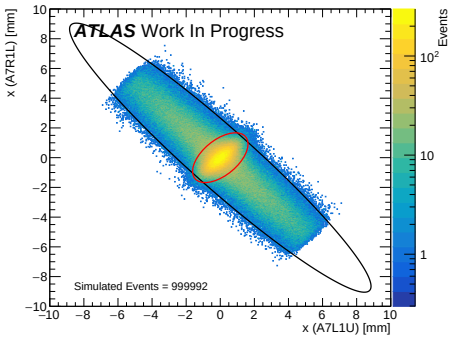

(b) x_i^A vs. x_i^C. 6/4 of nominal div.

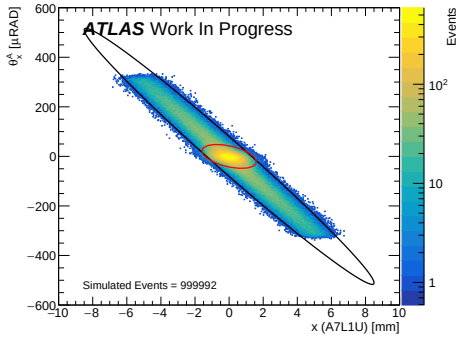

(c) x_i^A vs. θ_x^A. 0 divergence.

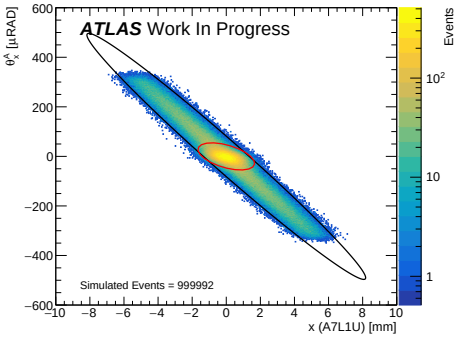

(d) x_i^A vs. θ_x^A. 6/4 of nominal div.

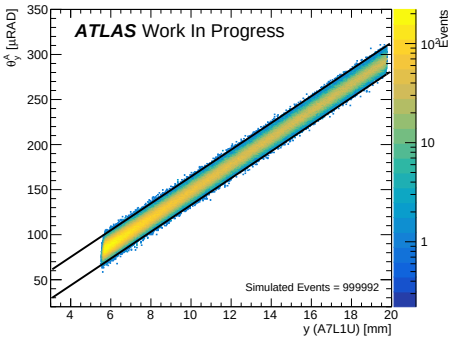

(e) y_i^A vs. θ_y^A. 0 divergence.

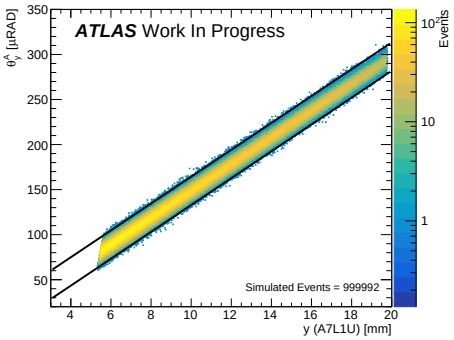

(f) y_i^A vs. θ_y^A. 6/4 of nominal div.

Figure 38: x_i^A vs. x_i^C, x_i^A vs. θ_x^A, and y_i^A vs. θ_y^A distributions with 0 and 6/4 of nominal divergence. With nominal BSW and detector smearing applied.

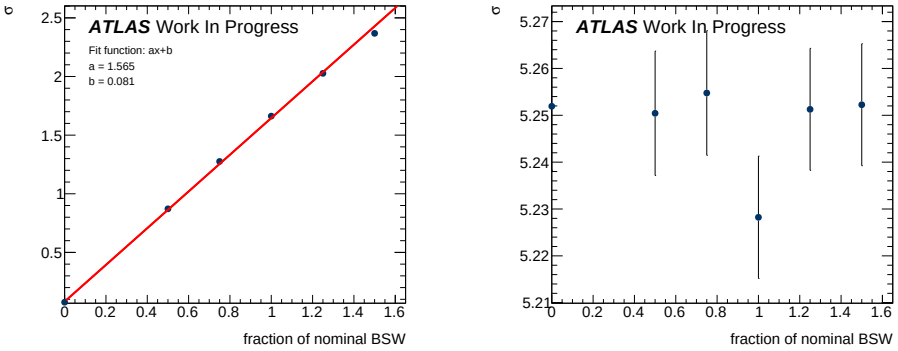

(a) y_i^A vs. y_i^C fit: σ (b) y_i^A vs. θ_y^A fit: σ

Figure 39: The evolution of the width of the signal, σ, as functions of the fraction of the nominal divergence, of the y_i^A vs. y_i^C and y_i^A vs. θ_y^A distributions.

are plotted in mm and a smearing of $\sim 0.1\,\text{mm}$ is therefore negligible and does not show in these plots. The same goes for fig. 40c and fig. 40d where the small contribution from the detector smearing is negligible compared to the smearing of the signal arising from the BSW which is visualized in fig. 33.

The effect of the detector smearing is seen in fig. 41. As discussed the y_i^A vs θ_y^A distribution is not affected by the BSW or the divergence due to parallel-to-point optics. This means that the detector smearing becomes the main factor of smearing of the signal. The detector smearing smears out the local angle, calculated from the y-coordinate in the inner and outer detectors, and as the outer detector has a much larger resolution than the inner detector due to multiple scattering, the signal is smeared.

3.4.5 The Transport Matrix

For further investigation the various features of the experiment, the transport matrix elements are varied to see how this affects the data signal in the elastic selection plots. The matrix elements studied are $M_{11,237}^{Ax}$ $M_{12,237}^{Ax}$

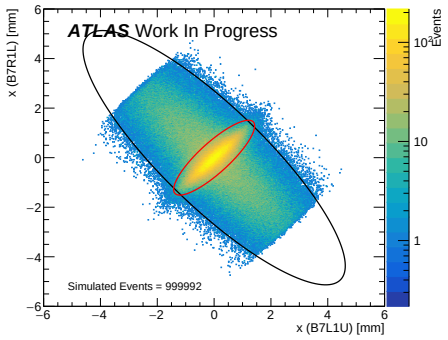

(a) x_o^A vs. x_o^C. No smearing.

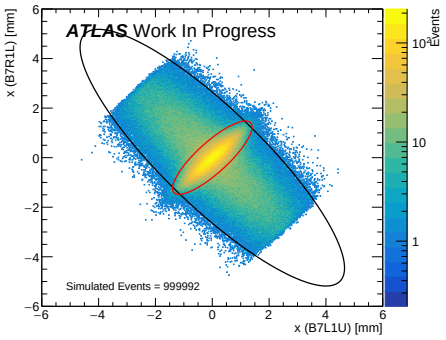

(b) x_o^A vs. x_o^C. With smearing.

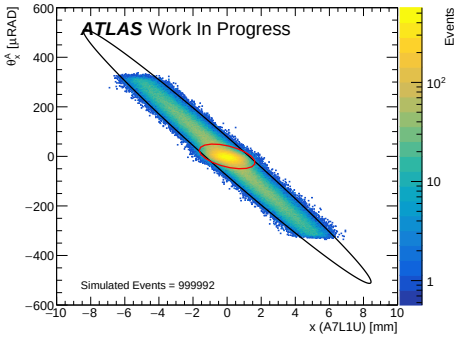

(c) x_i^A vs. θ_x^A. No smearing.

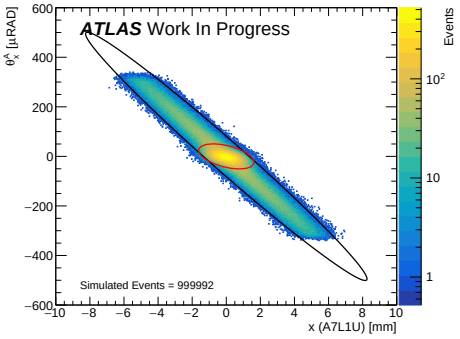

(d) x_i^A vs. θ_x^A. With smearing.

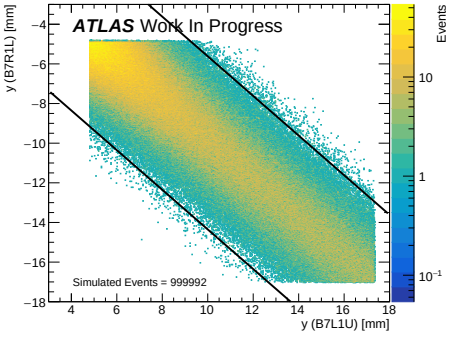

(e) y_o^A vs. y_o^C. No smearing.

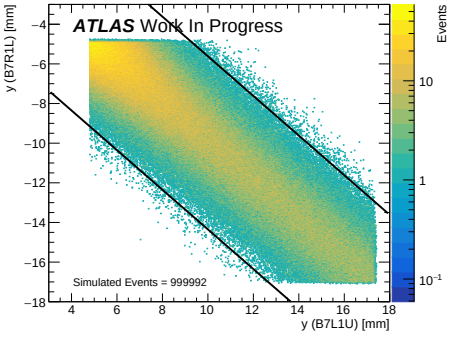

(f) y_o^A vs. y_o^C. With smearing.

Figure 40: The x_o^A vs. x_o^C, x_i^A vs. θ_x^A and y_o^A vs. y_o^C, distributions with and without detector smearing and with nominal BSW and divergence.

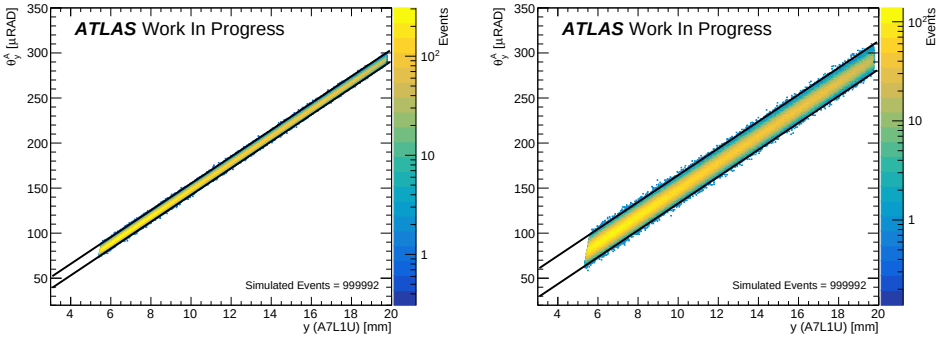

(a) y_i^A vs. θ_y^A. No smearing.

(b) y_i^A vs. θ_y^A. With smearing.

Figure 41: Distributions of y_i^A vs. θ_y^A generated with and without detector smearing and with nominal BSW and divergence.

of $A7L1_x$ presented in table 2, the x denoting the coordinate, A denoting the side, and 237 denoting the distance from the IP from the inner detector. This allows us to see how the signal of the x-coordinate, measured in the inner detectors on the A-side, is affected by the matrix elements.

The distribution of x_i^A vs x_i^C and x_i^A vs θ^A generated at different values of $M_{11,237}^{Ax}$ are presented in fig. 42 and fig. 43, respectively. It is clear that the signal fitted by the black ellipse remains diagonal for all plots, while the signal fitted by the red ellipse rotates as the absolute value of $M_{11,237}^{Ax}$ is made smaller.

The signal of the red ellipse is explained by the beam spot width. As a consequence of the beam having a width, the interaction point of the elastic events can be shifted in x and y, however due to the parallel-to-point optics no effect of the beam spot width is seen in y. If the IP of an elastic event is shifted in x, and has a dominantly vertical scattering angle, there will be no diagonal correlation between the two measured x-coordinates. Such event cause the signal fitted by the red ellipse. According to Hill's equation, eq. (36), the matrix element $M_{11,237}^{Ax}$ is multiplied with the position of the vertex point, hence matrix element $M_{11,237}^{Ax}$ influence the features of the signal

due to the beam spot width, which is the red ellipse.

In table 4 some of the fit values of the ellipses shown in fig. 42 and fig. 43 and in fig. 44 and fig. 45 are presented. Looking at the fits with $M^{Ax}_{11,237}$ varied, it is clear that the red ellipse of the x_i^A vs x_i^C and the x_i^A vs θ^A distributions is rotated, when having half the nominal value of the matrix element $M^{Ax}_{11,237}$, while we do not see any rotation going from the nominal value of $M^{Ax}_{11,237}$ to 90% of the nominal value. From the plots and the fit values, it is apparent that the varying of matrix element $M^{Ax}_{11,237}$ does not influence the angle of the black ellipse, which remains diagonal. However, when decreasing the value of $M^{Ax}_{11,237}$ the signal gets more narrow, as seen in the how values of σ_{x_B} and σ_{x_R} decrease as $M^{Ax}_{11,237}$ is decreased. This is expected it is the BSW that smears out the signal in the x-plane.

The fit in fig. 43a still has the diagonal black ellipse, although the red ellipse is rotated, which results in the signal within the black ellipse to be wider than for larger values of $M^{Ax}_{11,237}$.

Varying matrix element $M^{Ax}_{12,237}$ probes features of the data signal having to do with the diagonal correlations, due to the scattering angles. As the element $M^{Ax}_{12,237}$ is multiplied with the scattering angle at the IP, the $M^{Ax}_{12,237}$ has an impact on the signal feature associated with the scattering angle. This is mainly the signal of black ellipses of the double ellipse fits. We see a rotation of the black ellipse signal in all plots in fig. 44 and fig. 45. When varying $M^{Ax}_{12,237}$ it is only done for the detector on the A-side, and essentially when reducing $M^{Ax}_{12,237}$ the scattering angle is decreased making the signal in x on the A-side more narrow while the signal on the C-side remains the same. This results in a rotation of the black ellipse in fig. 44. As the scattering angles are reduced by making $M^{Ax}_{12,237}$ smaller, the signal in fig. 45 become more narrow in both θ^A and x. Thus, also rotating the black ellipses in these plots. The signals of the red ellipses do not seem to be affected much by varying $M^{Ax}_{12,237}$, as the signal of the red ellipse is mostly due to the beam spot width.

Distribution	θ [rad]	$\theta - \delta\theta$ [rad]	σ_{x_B} [mm]	σ_{x_R} [mm]
x_i^A vs. x_i^C: $0.5M_{11,237}^{Ax}$	0.7678	0.766	0.461	0.574
x_i^A vs. x_i^C: $0.9M_{11,237}^{Ax}$	0.7721	0.723	0.553	0.618
x_i^A vs. x_i^C: $1.0M_{11,237}^{Ax}$	0.7724	0.727	0.576	0.679
x_i^A vs. θ^A: $0.5M_{11,237}^{Ax}$	0.016	0.033	0.593	0.369
x_i^A vs. θ^A: $0.9M_{11,237}^{Ax}$	0.016	0.017	0.392	0.432
x_i^A vs. θ^A: $1.0M_{11,237}^{Ax}$	0.016	0.017	0.403	0.476
x_i^A vs. x_i^C: $0.7M_{12,237}^{Ax}$	0.592	0.317	0.454	0.685
x_i^A vs. x_i^C: $0.9M_{12,237}^{Ax}$	0.720	0.672	0.600	0.647
x_i^A vs. θ^A: $0.7M_{12,237}^{Ax}$	0.028	0.035	0.447	0.487
x_i^A vs. θ^A: $0.9M_{12,237}^{Ax}$	0.018	0.011	0.327	0.360

Table 4: The values of some fit parameters of the ellipses presented in fig. 42 and fig. 43, and in fig. 44 and fig. 45. θ is the angle of the black ellipse, and $\theta - \delta\theta$ is the angle of the red ellipse. The widths σ_{x_B} and σ_{x_R} are the widths of the black and red ellipse indicated by B and R. The errors of the fit values are negligible.

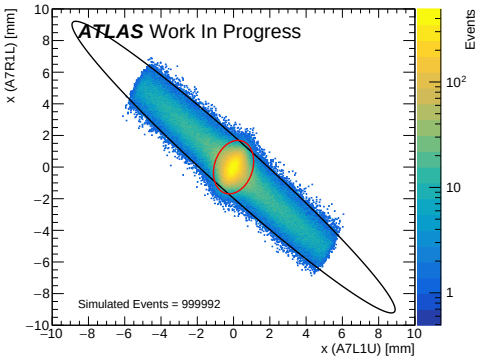

(a) $A7L1_x$: $0.5M_{11}$.

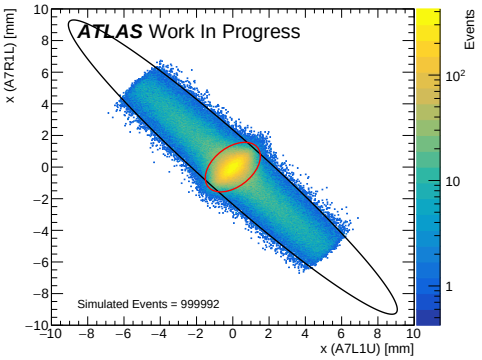

(b) $A7L1_x$: $0.9M_{11}$.

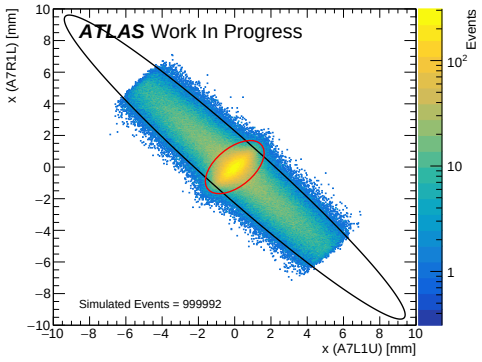

(c) $A7L1_x$: $1.0M_{11}$.

Figure 42: Distributions of x_i^A vs x_i^C fitted by the double ellipse fit. The three distributions have been generated at different values of the transport matrix element M_{11} of the x-coordinate measured in the inner detector on the A-side. The value of M_{11} is indicated by a fraction of the nominal value for each plot.

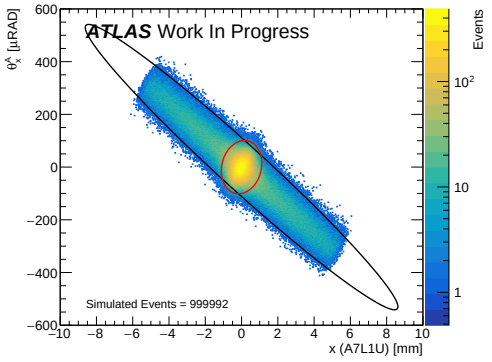

(a) $A7L1_x$: $0.5M_{11}$.

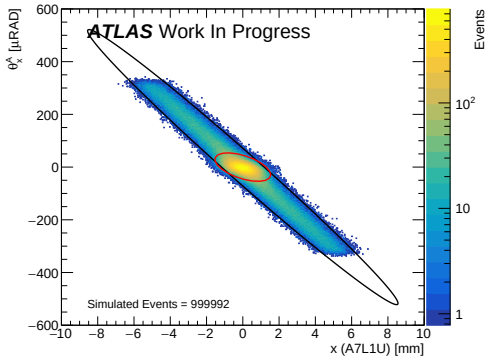

(b) $A7L1_x$: $0.9M_{11}$.

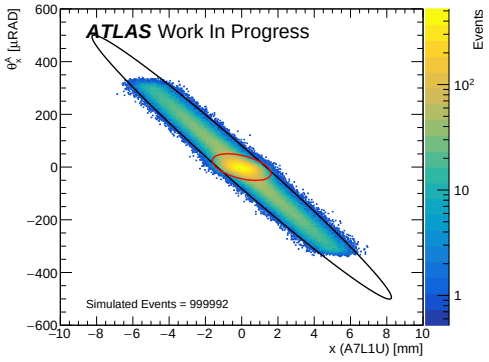

(c) $A7L1_x$: $1.0M_{11}$.

Figure 43: Distributions of x_i^A vs θ_x^A fitted by the double ellipse fit. The three distributions have been generated at different values of the transport matrix element M_{11} of the x-coordinate measured in the inner detector on the A-side. The value of M_{11} is indicated by a fraction of the nominal value for each plot.

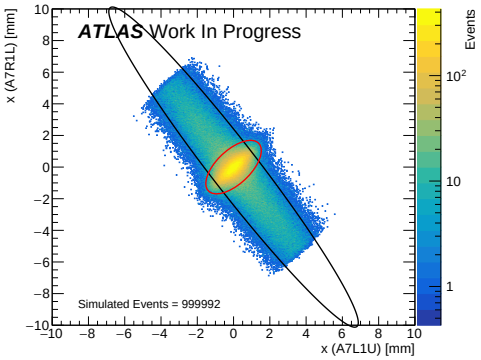

(a) $A7L1_x$: $0.7M_{12}$.

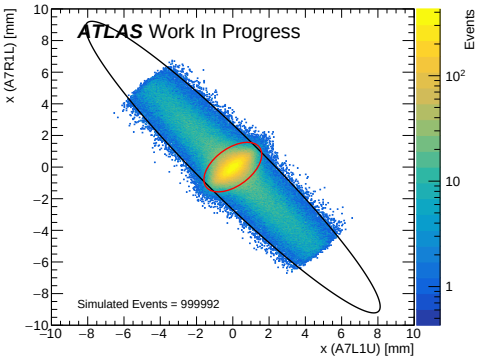

(b) $A7L1_x$: $0.9M_{12}$.

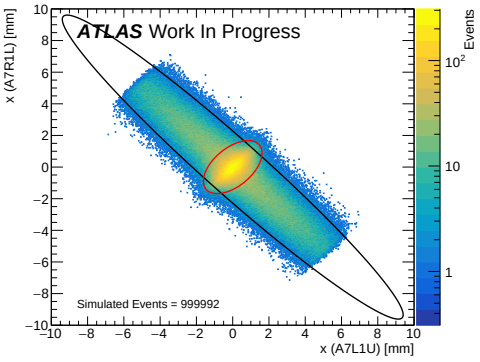

(c) $A7L1_x$: $1.0M_{12}$.

Figure 44: Distributions of x_i^A vs x_i^C fitted by the double ellipse fit. The three distributions have been generated at different values of the transport matrix element M_{12} of the x-coordinate measured in the inner detector on the A-side. The value of M_{12} is indicated by a fraction of the nominal value for each plot.

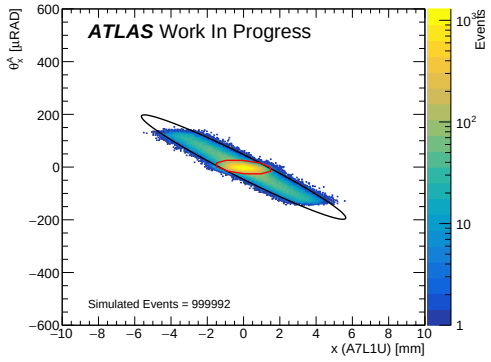

(a) $A7L1_x$: $0.7M_{12}$.

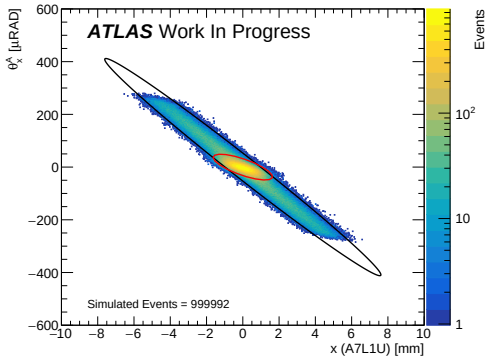

(b) $A7L1_x$: $0.9M_{12}$.

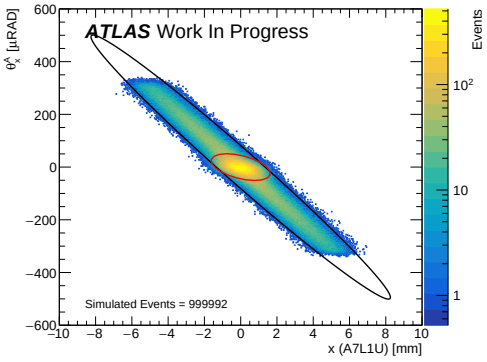

(c) $A7L1_x$: $1.0M_{12}$.

Figure 45: Distributions of x_i^A vs θ_x^A fitted by the double ellipse fit. The three distributions have been generated at different values of the transport matrix element M_{12} of the x-coordinate measured in the inner detector on the A-side. The value of M_{12} is indicated by a fraction of the nominal value for each plot.

3.5 Estimation of t

This section provides a description and performance analysis of the t-reconstruction methods, derived from Hill's equations, and a new reconstruction method called the Hyper Cube (HC) reconstruction method.

The differential cross-section as a function of the energy transfer, t, is described in theory by the formula given in eq. (28) with the parameters ρ, σ_{tot}, and the nuclear slope B. To fit the parameters to data, it is crucial to be able to reconstruct the scattering angle of the elastic scattered events as this is related to t by $t \simeq -(p\theta)^2$.

The t-reconstruction techniques currently used in ALFA are derived from the transport equations obtained from eq. (36). The transport equations are given by

$$u^A_{237} = M^A_{11,237}u^* + M^A_{12,237}(\theta^*_u + D^A_u) \tag{57}$$
$$u^A_{245} = M^A_{11,245}u^* + M^A_{12,245}(\theta^*_u + D^A_u) \tag{58}$$
$$u^C_{237} = M^C_{11,237}u^* + M^C_{12,237}(\theta^*_u + D^A_u) \tag{59}$$
$$u^C_{245} = M^C_{11,245}u^* + M^C_{12,245}(\theta^*_u + D^A_u) \tag{60}$$
$$\theta^A = M^A_{21}u^* + M^A_{22}(\theta^*_u + D^A_u) \tag{61}$$
$$\theta^C = M^C_{21}u^* + M^C_{22}(\theta^*_u + D^C_u) \tag{62}$$

The coordinates and matrix elements are denoted by A/C, indicating the side of the detector, and 237/245 indicating the distance to the interaction point. Hence, 237 denotes the inner detectors and 245 denotes the outer detectors. These equations can be combined into various methods of reconstructing the scattering angle. The matrix elements are known from MadX, while the interaction point, scattering angle, and the divergence are unknown. ALFA currently uses three reconstruction methods in combination with each other. These are called subtraction, local subtraction, local angle. For this analysis a new algorithm for t-estimation has been developed that uses simulated of events to estimate t, called the Hyper Cube (HC)

reconstruction method.

3.5.1 Subtraction

The subtraction method utilizes the coordinates measured on each side of the IP. Here the first four transport equations are used, where eq. (57) and eq. (59) constitutes the inner pair, and eq. (58) and eq. (60) constitutes the outer pair. Combining these equations we arrive at

$$\theta_u^* = \frac{\frac{M_{11}^C}{M_{11}^A}u^A - u^C}{\frac{M_{11}^C}{M_{11}^A}M_{12}^A + M_{12}^C} \approx \frac{u^A - u^C}{M_{12}^A + M_{12}^C} \tag{63}$$

The last part only holds if $M_{11}^A \approx M_{11}^C$. Comparing the values of the transport matrix, presented in table 2, it is seen that this only holds for y with the optics used for the 900 GeV campaign.

The final result can then be calculated by an average of the angle measured by the outer detectors and the inner detectors. A simple average only holds if the matrix elements of M_{12} is of similar size. Otherwise the least precise measurement will dominate over the reconstructed angle with the highest precision. From table 2 it is seen that there is a factor 2 between the values of $M_{x,12}$ between the inner and the outer detector, whereas the matrix elements for y are quite similar in size. In this analysis the subtraction method is used both with a simple average in x, and a version of the subtraction method where the outer coordinate is omitted, and one where the inner coordinate is omitted. As described the resolution in the outer detectors are far worse than for the inner detectors, hence we expect to see better performances for the techniques using measurements in the inner detectors rather than the outer.

3.5.2 Local Subtraction

Local subtraction is done by subtracting the measured coordinates of the inner detector with the coordinates measured in the outer detector on one

side of the detector. The eq. (57) and eq. (58) is used for the A-side and the eq. (59) and eq. (60) is used for the C-side. The scattering angle is then reconstructed by

$$\theta^*_{u,A/C} = \frac{M^{A/C}_{11,245}u^{A/C}_{237} - M^{A/C}_{11,237}u^{A/C}_{245}}{M^{A/C}_{11,245}M^{A/C}_{12,237} - M^{A/C}_{11,237}M^{A/C}_{12,245}} \tag{64}$$

An average of the reconstructed angles of the two sides is then combined to a final reconstructed scattering angle.

3.5.3 Local Angle

The local angle methods utilizes the fact that there are no magnets between the inner and outer detectors. This makes the calculation of the local angle in an armlet very straight forward. Combining eq. (61) and eq. (62) the scattering angle can be reconstructed as

$$\theta^*_u = \frac{\frac{M^C_{21}}{M^A_{21}}\theta^A_u - \theta^C_u}{\frac{M^C_{21}}{M^A_{21}}M^A_{22} - M^C_{22}} \approx \frac{\theta^A_u - \theta^C_u}{M^A_{22} - M^C_{22}} \tag{65}$$

Where $\theta^{A/C} = (u_{245} - u_{237})/d$, with d being the distance between the inner and outer detector. It is crucial to have large values of M_{22} in order to obtain high precision.

3.5.4 Reconstruction of t

The subtraction, local subtraction, and local angle reconstruction methods can be combined in various ways to determine the scattering angle. In this analysis 10 methods and combinations of methods are studied. The 10 methods of t reconstruction are:

- Subtraction (Sub)

- Subtraction inner (SubInner), where only the coordinates in the inner detectors are used. x-coordinates of the inner detectors are used, while both the outer and inner y-coordinates are used.
- Subtraction light out (SubLightOut), where only the x-coordinates of the outer detectors are used, while both the outer and inner y-coordinates are used.
- Full Local Subtraction (FullLocSub), where only local subtraction is used.
- Standard Local Subtraction (StdLocSub), where local subtraction are used in x, and subtraction are used in y.
- Full Local Angle (FullLocAng), where only the local angle method is used.
- Standard Local Angle (StdLocAng), where the local angle method is used in x and subtraction is used in y.
- Local Subtraction A (LocSubA), where only local subtraction on the A side is used.
- Local Subtraction C (LocSubC), where only local subtraction on the C side is used.

The results of the 10 combinations are presented in fig. 46 and fig. 47. The relative error on of the reconstruction precision is plotted against the true value of t, and it reveals that every reconstruction method is more efficient for large values of $|t|_{\text{true}}$. Low $|t|_{\text{true}}$ values are difficult to reconstruct, as small errors on the reconstruction leads to large relative errors. All the plots reveals a bias towards overestimating $|t|$ for low $|t|_{\text{true}}$. This is due to divergence. In fig. 49a and fig. 49a, the reconstruction efficiency of simulated data with no divergence is shown. The plots show that events below $|t| \approx 2 \cdot 10^{-4}$ is cut due to the edge of the detector and the edge cut, when

there is no divergence, and that the bias is gone. The divergence results in the scattering angles of the elastic events being measured as either smaller or larger than the true angle. This results in some events being overestimated and some being underestimated. One of the consequences of this is that some of the events that are not expected to be detected, due to the edge cut, are seen in the detector as their scattering angles are made larger by the divergence. These events are then predicted to have a higher value of $|t|$ than the true value, resulting in a bias for $|t|$ values below $|t| \approx 2 \cdot 10^{-4}$. This bias is seen as the tails to the right for low $|t|_{\text{true}}$ in all the plots in fig. 46 and fig. 47. It is clear that the tails are results of the divergence as the same bias is not seen in fig. 49 with no divergence. When plotting with divergence but without BSW the same bias is still present, as seen in fig. 50, which tells us that the bias is not due the BSW.

In fig. 48 the performances of all the reconstruction methods derived from the transport equations are compared. It is difficult to distinguish which reconstruction method is performing the best as most of the methods are performing at the same level. However, it is clear that the local subtraction methods done on only one side of the IP are the worst performing methods. By a small margin, the best performing reconstruction method is the subtraction method only using the inner detectors, called SubInner. The next best performers are the subtraction and subtraction light methods. By comparing the SubInner and the subtraction method, it is clear that adding the measurements in the outer detectors slightly worsens the performance. This is probably due to the resolution of the outer detector being around 3 times larger than the inner detectors, which then penalizes the reconstruction.

The error of the reconstruction of t comes primarily from the divergence. This is seen by comparing the plots of fig. 46a, fig. 46d, fig. 49a, fig. 49b, fig. 50a, and fig. 50b. The distributions show no notable difference when having no beam spot with, compared to having a beam spot width of nom-

inal size. However, with divergence turned off the reconstruction improves dramatically.

3.5.5 Hyper Cube Estimation

For this analysis a new t estimation method was developed. Each elastic event is measured in one of the arms of ALFA resulting in 8 measured coordinates per event. On the A-side is measured an x and y coordinate in the inner detector and an x and y coordinate measured in the outer detector, for one proton, the other outgoing proton is measured equivalently by the diagonally opposite armlet on the C-side. Hence, the elastic events are distributed in a 8-dimensional coordinate space. The Hyper Cube (HC) t-estimation is done by simulating events similar to data, which are also distributed in the 8-dimensional coordinate space. For each data point $|t|_{\mathrm{HC}}$ is then estimated by making a weighted average of the $|t|$ values of the nearby MC points. The weights of the weighted average is calculated as an 8-dimensional Gaussian distance from the nearby MC points to the data point given by:

$$w_i = \frac{1}{2\pi\sigma_i^4\sigma_o^4}\exp\Bigg[-\frac{1}{2\sigma_i^2}\Big(\sum_j^{A/C}(x_{D,ij}-x_{MC,ij})^2+(y_{D,ij}-y_{MC,ij})^2\Big) - \frac{1}{2\sigma_o^2}\Big(\sum_j^{A/C}(x_{D,oj}-x_{MC,oj})^2+(y_{D,oj}-y_{MC,oj})^2\Big)\Bigg]$$

where $\sigma_i = \sigma_{Det} = 29\,\mu\mathrm{m}$ and $\sigma_o = 95\,\mu\mathrm{m}$, and i/o denoting the inner/outer detectors, and D/MC denotes the data/MC coordinates. In this way the outer detectors, which have a poorer resolution, are suppressed a bit compared to the inner detectors. We already saw how the measurements in the outer detector actually makes the t-reconstruction a bit worse. As the measurements in the outer detectors are suppressed by their poor resolution, the measurements of the inner detectors become more important.

In order to not having to measure the distance to every MC point from every data point, both the data and MC points are sorted in hyper cubes (HCs). The event distributions of the 4 x-coordinates are given in fig. 51

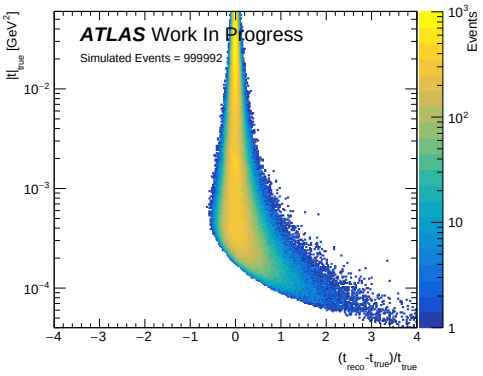

(a) Subtraction.

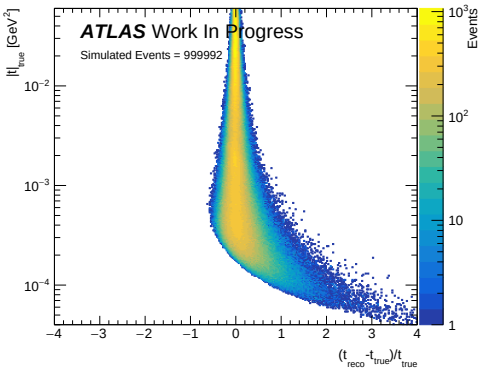

(b) Subtraction Light.

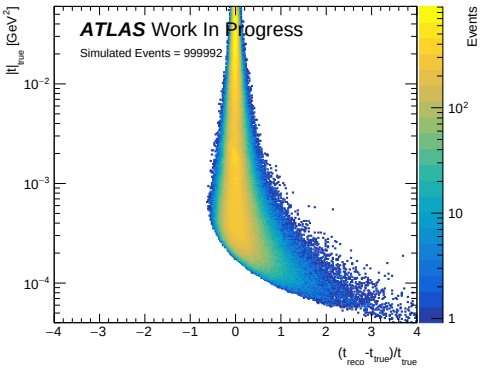

(c) Subtraction light out.

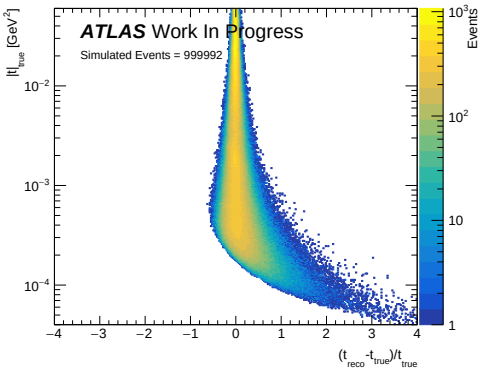

(d) Subtraction Inner.

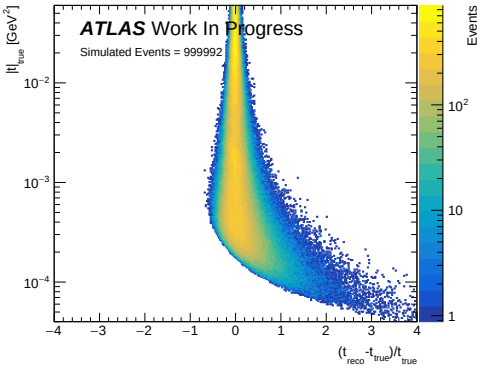

(e) Full Local Sub.

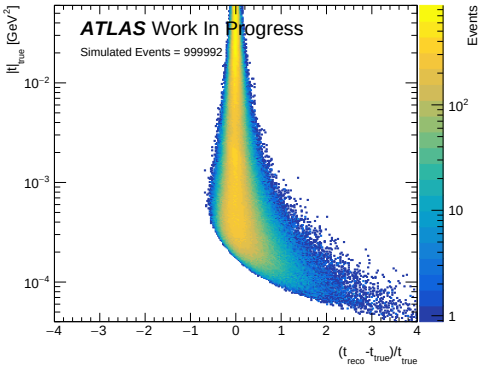

(f) Standard Local Sub.

Figure 46: The performances of the t-reconstruction methods. The relative error of $|t|_{reco}$ as a function of $|t|_{\text{true}}$.

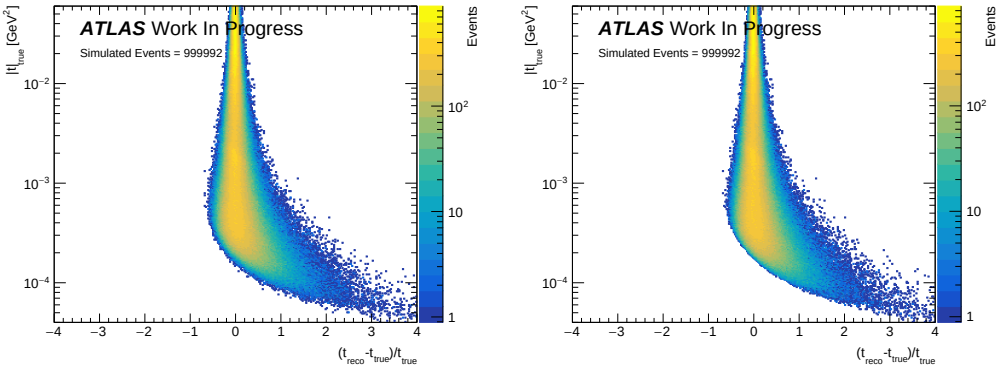

(a) Full Local Angle.

(b) Standard Local Ang.

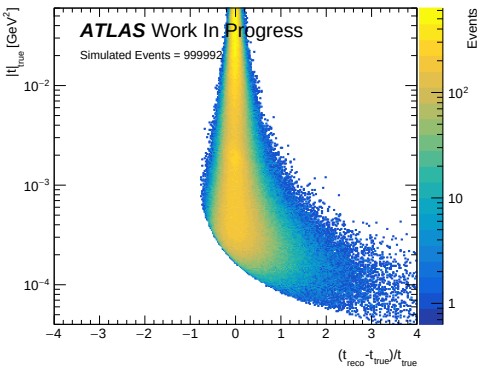

(c) Local Subtraction A.

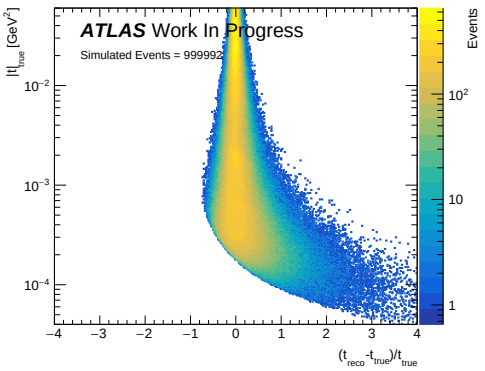

(d) Local Subtraction C.

Figure 47: The performances of the t-reconstruction methods (continued). The relative error of $|t|_{reco}$ as a function of $|t|_{\text{true}}$.

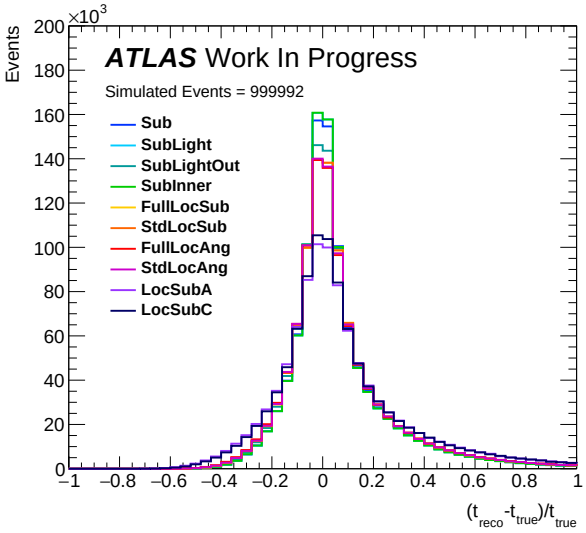

Figure 48: The relative error of the reconstruction of t, for the 10 different methods.

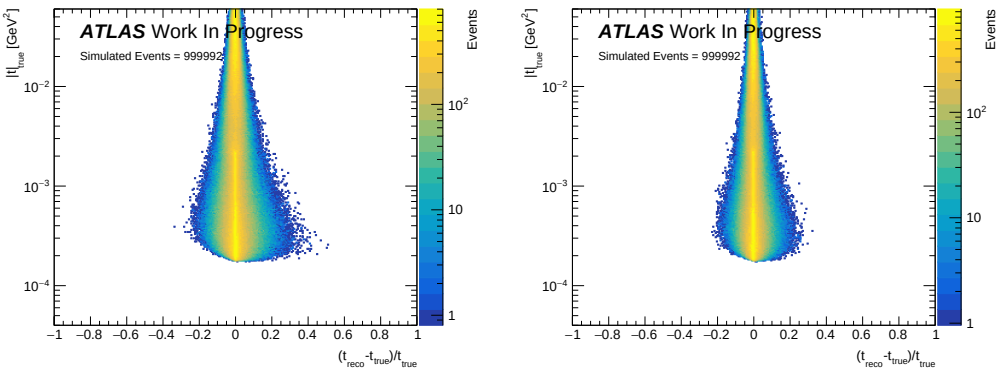

(a) Subtraction. No divergence.

(b) Sub. Inner. No divergence.

Figure 49: Best performing t-reconstruction methods, Subtraction and SubInner, done on simulated data with no divergence.

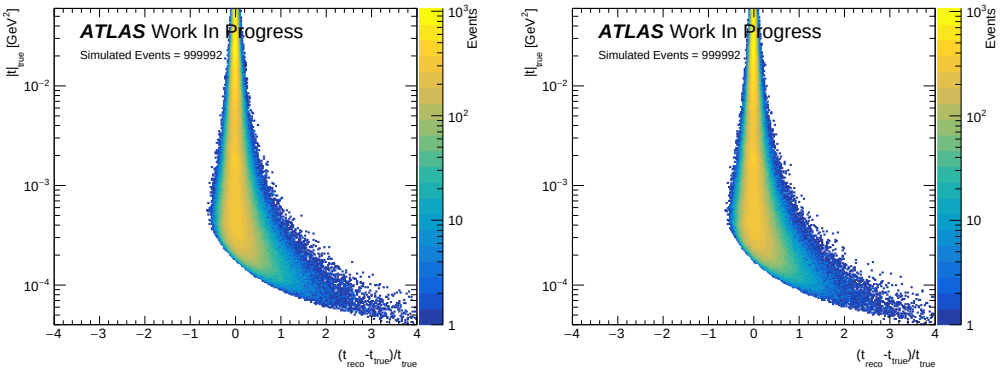

(a) Subtraction. No BSW.

(b) SubInner. No BSW.

Figure 50: Best performing t-reconstruction methods, Subtraction and SubInner, done on simulated data with no beam spot width.

and the distributions of the 4 y-coordinates are given in fig. 52. Here the red dotted lines indicates how the 8 coordinates are split in ten ranges each, which makes up the HCs. The ranges are set by eye such that there is roughly the same amount of events in each range.

The HC t-estimation for a data point is done by calculating the Gaussian weights to all MC points in the same hyper cube, and to all MC points in the surrounding HCs that are within 100 µm distance of the HC containing the data point. When the weights are calculated the $|t|_{\text{HC}}$ of the data point is estimated by a weighted average. Thus, the MC points close to the data point has a larger impact on the HC t-estimation than the MC points further away.

For this analysis two MC samples are used for the HC reconstruction method. The main MC sample of 10,000,000 events distributed in the full $|t|$-range, $4 \cdot 10^{-5}\,\text{GeV}^2 \leq |t| \leq 6 \cdot 10^{-2}\,\text{GeV}^2$, is combined with an MC sample of 4,000,000 events distributed in the low $|t|$-range of $4 \cdot 10^{-5}\,\text{GeV}^2 \leq |t| \leq 5 \cdot 10^{-3}\,\text{GeV}^2$ is used, to achieve a more precise reconstruction of t in the low energy regime, where the reconstruction is known to be difficult.

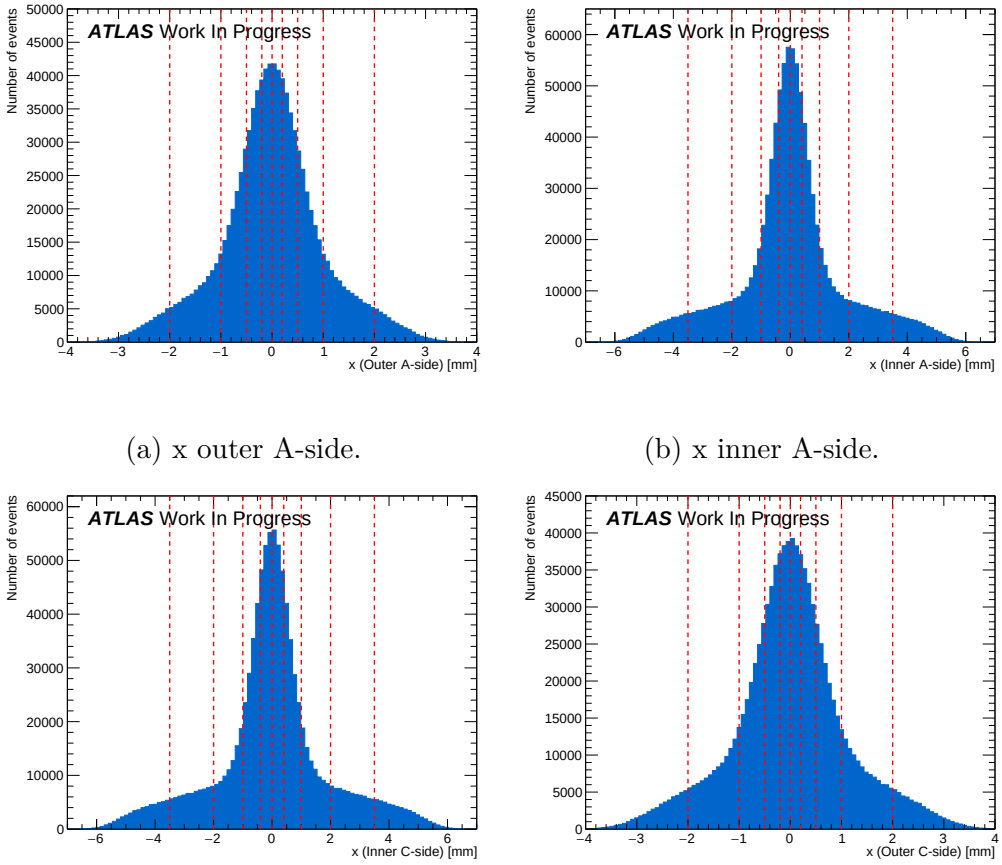

(a) x outer A-side.

(b) x inner A-side.

(c) x inner C-side.

(d) x outer C-side.

Figure 51: The signal distributions of the x-coordinates measured in the ALFA detectors. The red dotted lines indicates where the distributions are split into HCs.

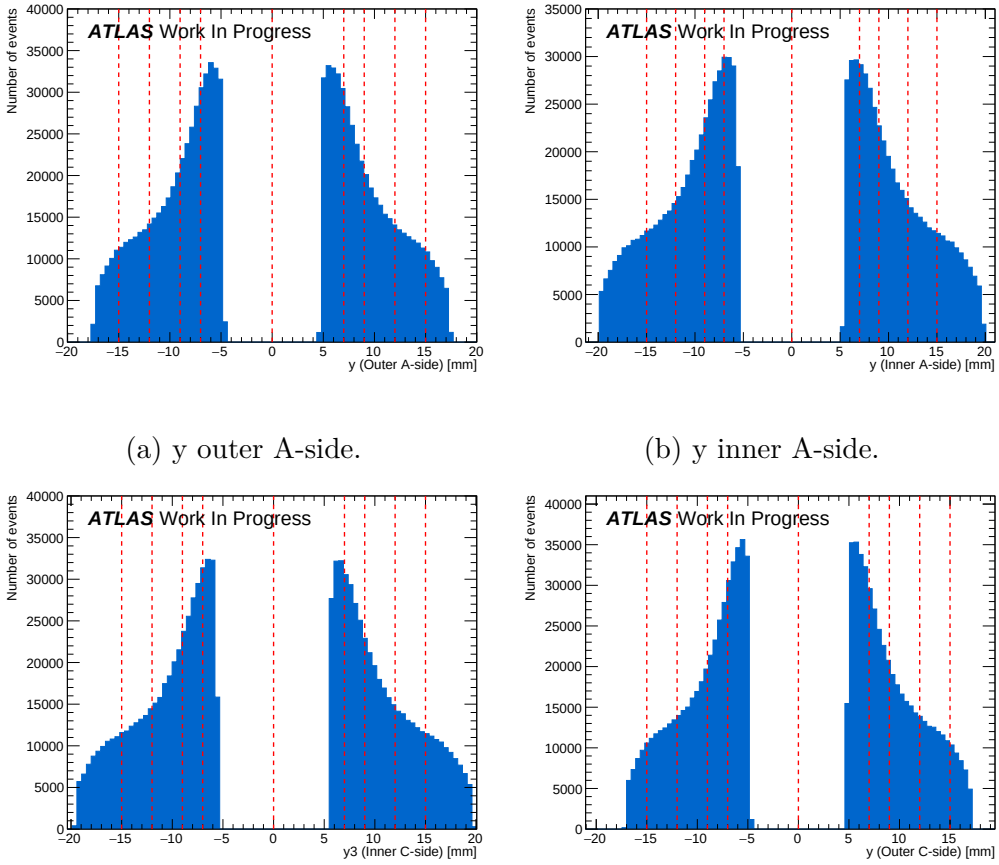

(a) y outer A-side.

(b) y inner A-side.

(c) y inner C-side.

(d) y outer C-side.

Figure 52: The signal distributions of the y-coordinates measured in the ALFA detectors. The red dotted lines indicates where the distributions are split into hyper cubes.

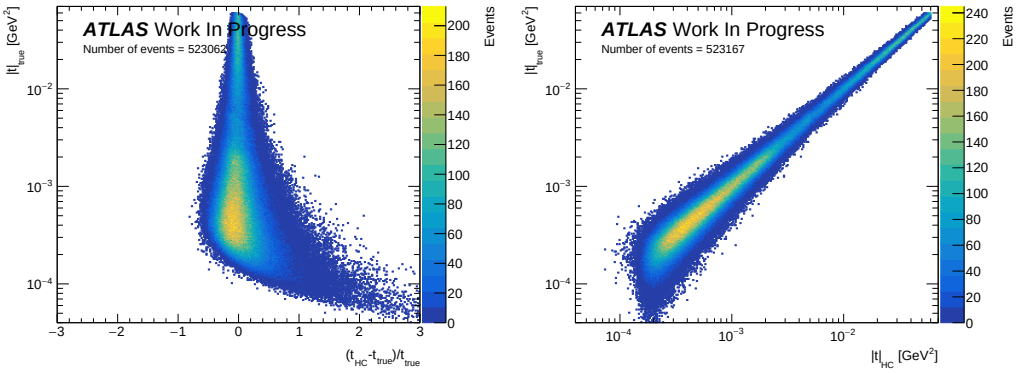

(a) The relative error of $|t|_{\text{HC}}$.

(b) $|t|_{\text{HC}}$ vs. $|t|_{\text{true}}$.

Figure 53: The performance of the HC reconstruction of t, where $|t|_{\text{HC}}$ is $|t|$ estimated by the HC reconstruction method.

HC Estimation Performance

The idea of the HC estimation was to get a smaller bias of the reconstructed t-values, by using all of the information of the data point and comparing to the surrounding MC points generated at different values of $|t|$. However, from the plots in fig. 53 a bias to overestimate $|t|$ is seen for small values of $|t|_{\text{true}}$ as was seen for the other reconstruction methods. By comparing fig. 53a and fig. 54a, it can be concluded that the SubInner method is more precise but slightly more biased than the HC reconstruction. By comparing fig. 53b and fig. 54b it is seen that the HC method, although less precise, are able to estimate events to have lower $|t|_{\text{HC}}$ values, than the SubInner method, as the SubInner methods is not able to estimate $|t|$ values below $2 \cdot 10^{-4}$ due to the edge cut. Hence, using the SubInner method some information are lost for small values of $|t|_{\text{true}}$, and as we shall see the fit parameter ρ are sensitive to events for low $|t|$ making these events very important.

The problem right now with the HC estimation method is that due to the emittance, divergence, and detector smearing the points are scattering widely in the 8-dimensional space. This means that not all data points are close enough to an MC point in order to be estimated. The HC estimation

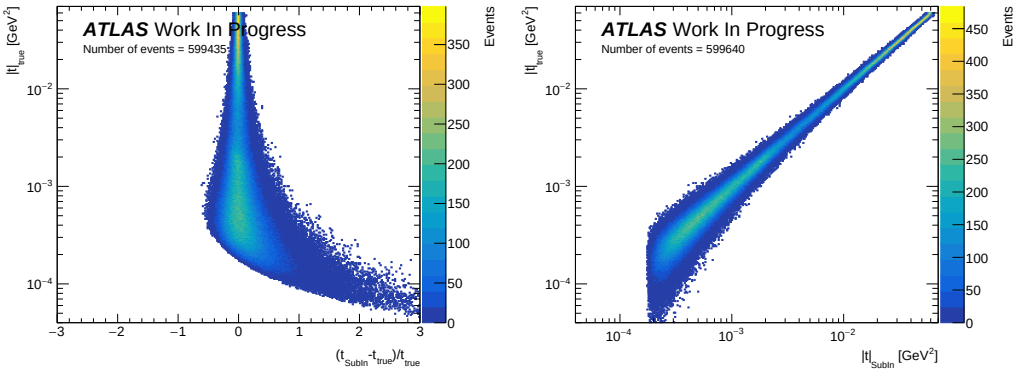

(a) The relative error of $|t|_{\text{SubIn}}$.

(b) $|t|_{\text{SubIn}}$ vs. $|t|_{\text{true}}$.

Figure 54: The performance of the SubInner reconstruction of t, where $|t|_{\text{SubIn}}$ is $|t|$ estimated by the SubInner reconstruction method. Here the SubInner reconstruction is done on the same points as for the HC reconstruction in fig. 53.

misses around 13% of the data points and they are distributed as shown in fig. 55. Most of the points not seen by the MC simulation are events with large values of $|t|$, which means they have large scattering angles. These events are more likely to be missed as they are distributed onto a larger area due to the elastic events being uniformly distributed in the azimuthal angle, ϕ. The distribution has a bump around $5 \cdot 10^{-3}\,\text{GeV}^2$, which is likely due to the extra MC estimation sample of 4 million events generated in the $|t|$-range of $4 \cdot 10^{-}5\,\text{GeV}^2$ to $5 \cdot 10^{-}3\,\text{GeV}^2$.

As the distribution of event in fig. 55 is not uniform, the distribution of events estimated is changed compared to generated sample. Thus, to make up for this, the events that are missed by the HC estimation is instead estimated by the SubInner reconstruction method. Looking at fig. 46d, the performance of $|t|$, hence we expect the missed event to be estimated with a good precision.

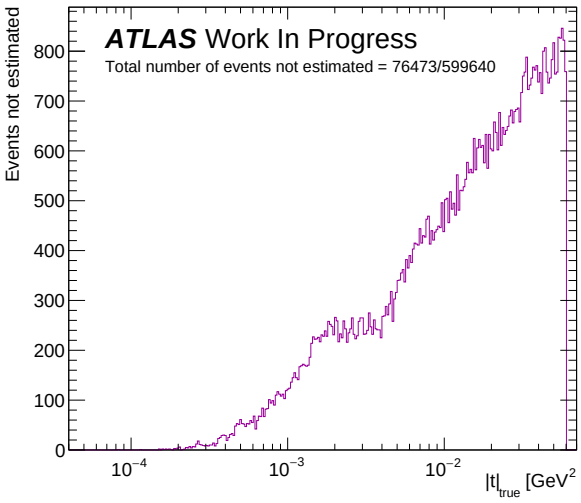

Figure 55: Distribution of $|t|$ of points not estimated by the HC reconstruction method.

HC $d\sigma/dt$ estimation

The estimation of $d\sigma/dt$ ($d\sigma$) is important for the likelihood fit, that will be discussed in the next section. It is usually done by estimating t and then translating this into a value for $d\sigma$ by the theory formula presented in eq. (28). Using the HC estimation method $d\sigma$ could be estimated directly by the weighted average, the same way as for the HC t-estimation described earlier. $d\sigma$ as a function of $|t|$ has a very steep curve in some $|t|$-ranges, where small errors in t-estimation will blow up the relative error of the estimated $d\sigma$. By estimating $d\sigma$ directly this may be avoided.

The methods of $d\sigma$ estimation is presented in fig. 56, here $d\sigma$ is estimated by the theory function and the estimated $|t|$ value estimated by the HC reconstruction method and the SubInner method in fig. 56a and fig. 56b respectively, and in fig. 56c $d\sigma$ is estimated directly from the weighted average the nearby MC points. From these plots we do not observe a drastic improvement from estimating $|t|_{\mathrm{HC}}$ to estimating $d\sigma_{\mathrm{HC}}$. The most precise

estimation of $d\sigma$ is done with the SubInner method, as was seen for the t-reconstruction, but the bias is also stronger in this case. All three methods are biased towards underestimating $d\sigma$ for small values of $|t|_{\text{true}}$. This is explained by the bias of the $|t|_{\text{HC}}$ and $|t|_{\text{SubIn}}$ estimation, where the divergence causes events with $|t|$-values below $\sim 2 \cdot 10^{-4}$ to end up in the detector and being overestimated. This results in underestimation of $d\sigma$ for low values of $|t|_{\text{true}}$ as $d\sigma$ decreases when going up in transferred energy, $|t|$.

All three methods have a tendency to overestimate $d\sigma$ in the range of $2 \cdot 10^{-4} \leq |t|_{\text{true}} \leq 2 \cdot 10^{-3}$. This is probably due to the very steep slope of the $d\sigma$ as a function of $|t|$ in that range as seen in fig. 6. When estimating $d\sigma$ from a value of $|t|$, it can cause huge relative errors if $|t|$ is underestimated, whereas the relative errors does not become quite so large when overestimating $|t|$ as the curve flattens when going to larger $|t|$. For the HC estimations in fig. 56a and fig. 56c the bias towards overestimating $d\sigma$ is greater than for the SubInner method. This again has something to do with the steep slope of $d\sigma$. As the MC simulation is generated from the theoretical function of $d\sigma$, a lot more events are created at large (small) values of $d\sigma$ ($|t|$). Hence, the $d\sigma$ of the data points is estimated by more MC points with high (low) values of $d\sigma$ ($|t|$), leading to an overestimation of $d\sigma$. This bias may be solved by estimating $d\sigma_{\text{HC}}$ and $|t|_{\text{HC}}$ with a more flat distribution of points as a function of $|t|$.

As there is not seen any major improvements when estimating $d\sigma_{\text{HC}}$ with the HC method, this method will not be used for fitting. Instead, the fitting routine will be carried out using the HC t-reconstruction method and the SubInner method. As the energy transfer for an elastic event is just a matter of the momentum and the scattering angle, it does not change when varying the theory of the differential cross section. So by using the t-estimation methods the measurements of t in the detectors and the theory are kept apart until the fitting routine.

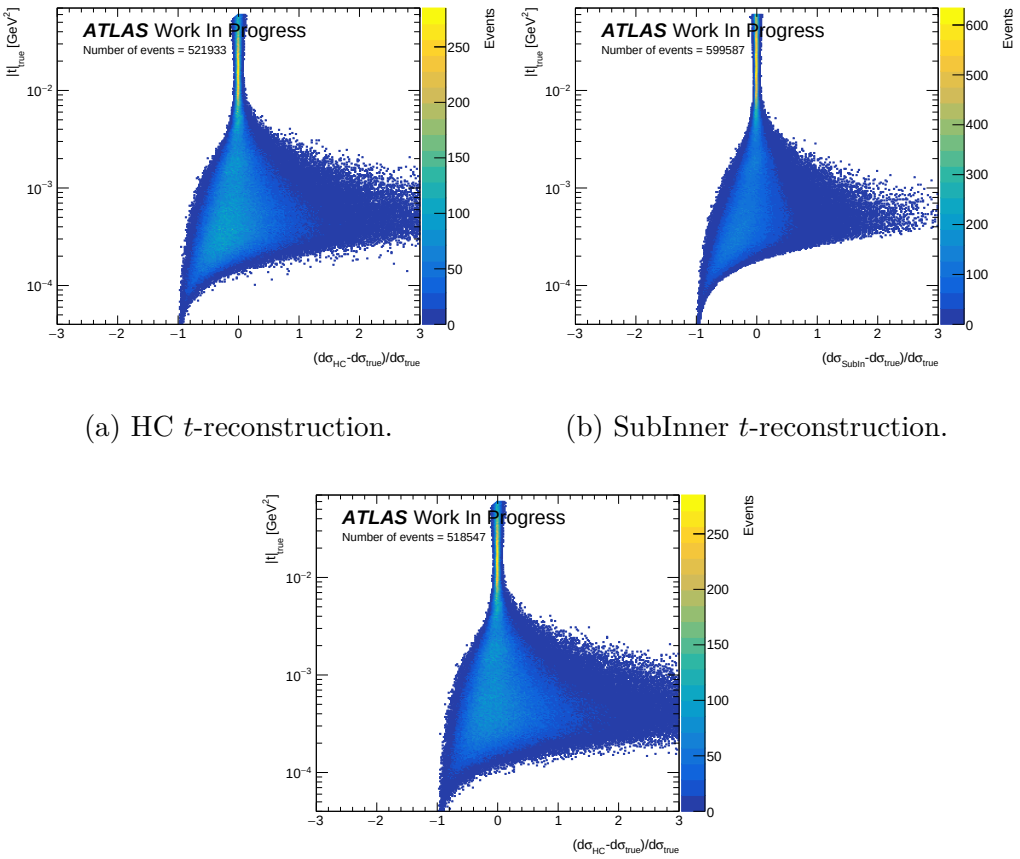

(a) HC t-reconstruction.

(b) SubInner t-reconstruction.

(c) HC $d\sigma$-estimation.

Figure 56: Relative error of $d\sigma$-estimation as function of $|t|_{\text{true}}$. $d\sigma$ is estimated by calculating it from the theory function with $|t|_{\text{HC}}$, and $|t|_{\text{SubIn}}$ in (a) and (b). In (c) $d\sigma$ estimated directly by HC method.

3.6 Fit

This section presents a study of the performance of a maximum log-likelihood fit routine developed for the estimation of the theory parameters from simulated data. The log-likelihood fit is studied by fitting simulated data, reconstructed with both the HC method and the SubInner method, to see which t-reconstruction methods performs best when fitting. The fit performance is tested by fitting an MC data sample of $\sim 600,000$ events, with another MC sample of $\sim 5,000,000$ events. The fit is not yet tested on real data.

The log-likelihood used for this analysis is given by

$$-2LLH(\bar{q}) = 2\sum_{i=1}^{N_{data}} \ln p_i = 2\sum_{i=1}^{N_{data}} \ln\left(\frac{d\sigma_i(\bar{q},t_i)}{\sum_{j=1}^{N_{MC}} \frac{d\sigma_j(\bar{q},t_j)}{d\sigma_j(\bar{q_G},t_j)}}\right) \tag{66}$$

where N_{data} is the number of data points, $d\sigma_i(\bar{q},t_i)$ is the differential cross section calculated from theory with the parameters $\bar{q}$ for the i'th data point. N_{MC} is the number of MC points used for the normalisation, $d\sigma_j(\bar{q},t_j)$ is the differential cross section calculated with the parameters $\bar{q}$ for the j'th MC point, and the parameters $\bar{q_G}$ is the parameters from which the MC sample was created. $\bar{q_G}$ is only used as a reference point and should not affect the fit results. The log-likelihood is multiplied by -2, which means that eq. (66) should be minimized in order to find the parameter value that results in the maximum probability for the data set. The factor 2 is added for it to match a χ^2.

The sum in the denominator is the normalization, where the theory is reweighted in reference to the theory at which the MC sample was generated.

3.6.1 Bias Correction

The distributions shown in fig. 53 and fig. 54 reveals a bias towards overestimating $|t|$ for low values of $|t|_{\text{true}}$ for both the SubInner and HC reconstruction method. This bias can be corrected for by utilizing the distributions

presented in fig. 53b and fig. 54b. These plots shows the distributions of the $|t|_{\text{true}}$ for all reconstructed values of $|t|$. When correcting the bias $d\sigma$ is calculated by extracting the distribution of the $|t|_{\text{true}}$ for the given value of $|t|_{\text{HC}}$, or $|t|_{\text{SubIn}}$ and using this distribution as a PDF. This is done by creating a 1D histogram of $|t|_{\text{true}}$ by slicing the histograms of fig. 53b and fig. 54b at the value of either $|t|_{\text{HC}}$ or $|t|_{\text{SubIn}}$ depending on the reconstruction method. This 1D $|t|_{\text{true}}$ histogram is then normalized to 1 making it a PDF of the $|t|_{\text{true}}$ values for that given value of $|t|_{\text{HC}}$ ($|t|_{\text{SubIn}}$). The bias corrected value of $d\sigma_{BC}$ is then calculated by

$$d\sigma_{BC}(\bar{q}) = \sum_{i=1}^{N_{bins}} n_i d\sigma(\bar{q}, |t|_{true,i}) \tag{67}$$

where n_i value of the i'th bin, corresponding to the probability of the event having the value of $|t|_{true,i}$, which is the value of the bin center of the i'th bin. $d\sigma(\bar{q}, |t|_{true,i})$ is $d\sigma$ calculated with the value of $|t|_{true,i}$, and N_{bins} being the number of bins of the 1D slice histogram. In this way $d\sigma_{BC}$ takes into account all the possible values of $|t|_{\text{true}}$ that the given event has a probability of having. Three of the 1D slice histograms at three given values of $|t|_{\text{HC}}$ and $|t|_{\text{SubIn}}$ are shown in fig. 57, where the means of the slices are indicated by the dotted lines.

This bias correction method is carried out for both the HC estimation method and the SubInner method and the performance is tested by how well the fit performs with and without the bias correction.

3.6.2 Preliminary Tests

Preliminary tests have been carried out in order to make sure that the fitting method is behaving properly, and to ensure that we can trust the fit.

Presented in fig. 58 is how the theory function behaves when varying the three fit parameters ρ, σ_{tot}, and B. When changing one variable the other variables are fixed so that only the effect of the one variable shows. The important $|t|$-ranges for each of the parameters can be seen from fig. 58. From

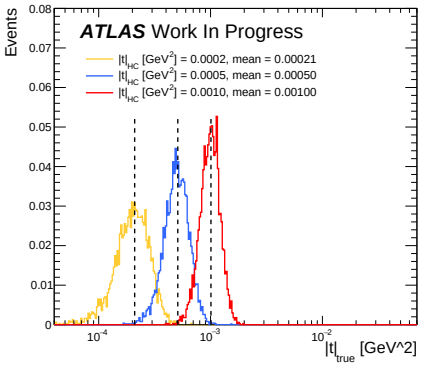

(a) Slices of fig. 53b at 3 values of $|t|_{\mathrm{HC}}$.

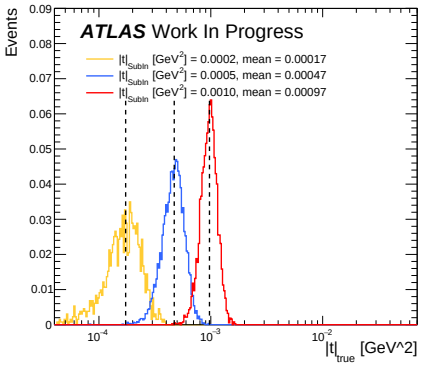

(b) Slices of fig. 54b at 3 values of $|t|_{\mathrm{SubIn}}$.

Figure 57: Three vertical slices of the plots fig. 53b and fig. 54b, at the values $|t|_{HC/SubIn} = 2 \cdot 10^{-4}\,\mathrm{GeV}^2$, $5 \cdot 10^{-4}\,\mathrm{GeV}^2$, $1 \cdot 10^{-3}\,\mathrm{GeV}^2$. The black dotted line indicate the mean value of the histograms.

fig. 58a it is clear that to fit ρ it is important to have events in the $|t|$-range from around $10^{-4}\,\mathrm{GeV}^{-2}$ to $5 \cdot 10^{-3}\,\mathrm{GeV}^{-2}$, as this is the region for which ρ has an impact on how many events is expected. In fig. 58b it shows that for σ_{tot} the crucial $|t|$-range is from $5 \cdot 10^{-4}\,\mathrm{GeV}^{-2}$ and beyond, and for the nuclear slope B the crucial $|t|$-range is from $5 \cdot 10^{-4}\,\mathrm{GeV}^{-2}$, which can be seen in fig. 58c. This information is useful when fitting as it may explain why the fits performs as it does for the different parameters.

The denominator of eq. (66) is the reweight normalization used for this particular fit. The reweight normalization is expected to behave the same way no matter what initial parameters the MC sample is generated at, apart from an offset between MC samples not generated with the same theory parameters. However, the evolution of the reweight normalization should be the same for different values of $\bar{q_G}$. This is shown in fig. 59 where the reweight normalization sum as a function of the three parameters are plotted for three different MC samples, generated at different values of ρ, while σ_{tot} and B are

kept the same for the three samples. Looking at all three plots in fig. 59, it is clear that the reweight normalization sums, as functions of the test parameters, all has identical slopes but different offsets as expected. This means that the fitting function in eq. (66) will be independent of the parameters at which the MC sample is generated.

Comparing with the plots in fig. 58, we see that the normalization sum is expected to increase when decreasing ρ_{test}, which is exactly what happens for all three functions in fig. 59a. The reweight normalization is expected to increase as a function of $\sigma_{tot,test}$, which is also what is observed in fig. 59b. This makes sense as σ_{tot} is the total cross-section, and when the cross-section increases more events should be observed. The functions in fig. 59c all have a decreasing normalization sum as a function of the nuclear slope B_{test}, which is again what is expected by looking at fig. 58c.

3.6.3 Fit Performance

The fit performance is tested for three t-reconstruction methods; SubInner, HC, and HC and SubInner combined. The fit is compiled both with and without the bias correction, to test if the bias correction enhances the fit performance. The MC data sample, that is fitted, is of approximately 600,000 events is generated at the values of $\rho = 0.1$, $\sigma_{\text{tot}} = 68\,\text{mb}$, and $B = 16\,\text{GeV}^{-2}$, and so is the MC sample used for the reweight normalization.

To test how the t-reconstruction methods perform while fitting, the fitting function in eq. (66) is evaluated by varying one variable and fixing the other two variables to the true values. This yields parabolas with a minimum around the fitted value, and the error of the fit can be estimated by eye by going up 1 on the y-axis from the minimum and reading the parameter value corresponding to $y_{min} + 1$.

In fig. 60 is shown how the three parameters ρ, σ_{tot}, and B fits individually with the other two parameters fixed, when using only the HC reconstruction method and not taking the missed events into account. The parameter values to be fitted are presented on the plots. As expected fig. 60 yields that the

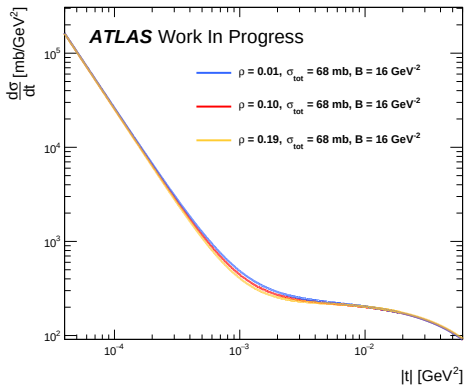

(a) $\rho = 0.01,\ 0.1,\ 0.19$.

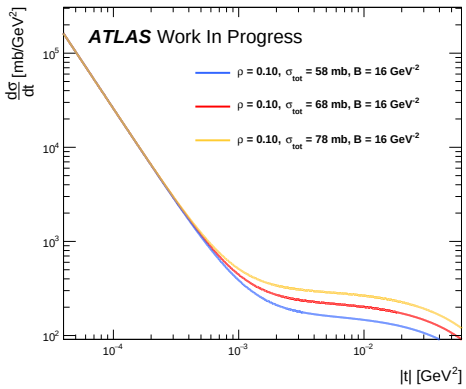

(b) $\sigma_{\text{tot}} = 58\,\text{mb},\ 68\,\text{mb},\ 78\,\text{mb}$.

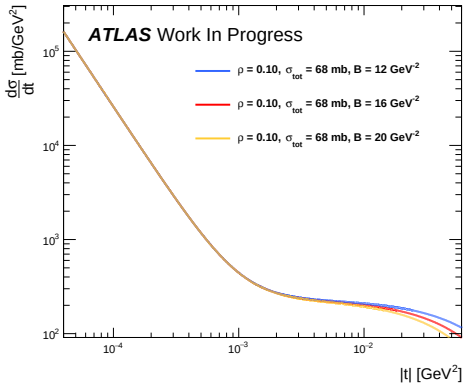

(c) $B = 12\,\text{GeV}^{-2},\ 16\,\text{GeV}^{-2},\ 20\,\text{GeV}^{-2}$

.

Figure 58: The theory function with varying values of ρ, σ_{tot}, and B. Each variable are varied with the other two variables fixed, in order to see how the theory function changes as the parameters are varied.

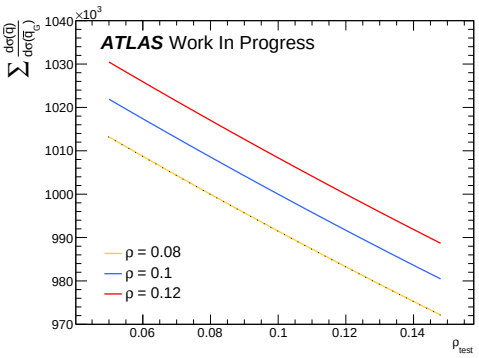

(a) $\sum \frac{d\sigma_j(\bar{q},t_j)}{d\sigma_j(q_{\bar{G}},t_j)}$ as function of ρ.

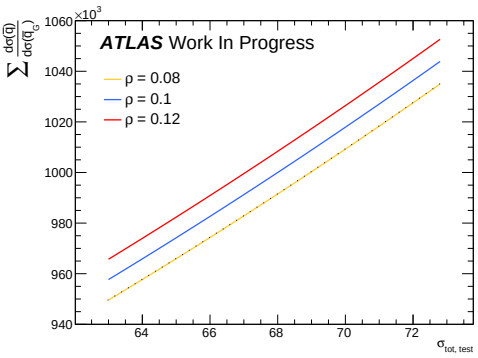

(b) $\sum \frac{d\sigma_j(\bar{q},t_j)}{d\sigma_j(q_{\bar{G}},t_j)}$ as function of σ_{tot}.

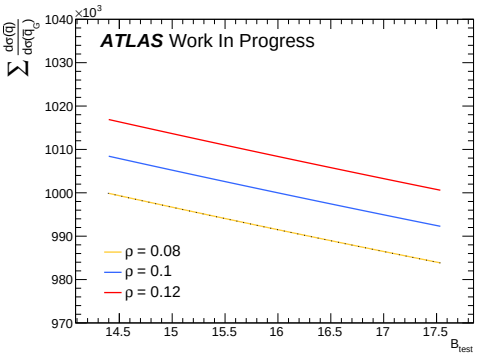

(c) $\sum \frac{d\sigma_j(\bar{q},t_j)}{d\sigma_j(q_{\bar{G}},t_j)}$ as function of B.

Figure 59: The reweight normalization as function of the three parameters ρ, σ_{tot} and B, calculated from three different MC samples The three samples are all generated with $\sigma_{\text{tot}} = 68\,\text{mb}$, and $B = 68\,\text{GeV}^{-2}$, and has different values of ρ being $\rho = 0.08$, 0.1, 0.12.

HC method on it is own is not very successful in fitting the correct values. As there's a lot of points not included in this fit, the distribution of events as a function of $|t|$ is missing all the events plotted in fig. 55. Hence, the distribution that is fitted does not represent the true distribution of the theory from which the MC data sample is generated. In order to account for the events that are not estimated by the HC reconstruction, these events are instead reconstructed by the SubInner reconstruction method. The fits done on MC data with reconstructed t of the combined HC and SubInner method is presented in fig. 61. These fits all show improvements compared to the fits in fig. 60. All of the fits in fig. 61 seems to have a minimum within one σ of the true value, however none of the fits have the minimum of exactly the correct value.

The bias correction has also been applied to the fit with the reconstructed t of the combined HC and SubInner method. These fits are shown in fig. 62 and shows that the fit to σ_{tot} improves a bit as it has a minimum of -2LLH is closer to the true value. The fitted minimum changes for ρ and is now overestimated a bit with the true value being within 2σ instead of 1σ as for the non bias corrected fit. The bias correction does not seem to change the fit to B, which was also already fitted within 1σ without the bias correction.

The fitting of events reconstructed with the SubInner method is tested in fig. 63. In fig. 63a it is seen that the fit is not sensitive to ρ and does not fit the correct value. The fit to σ_{tot} in fig. 63b is more precise however still several σs from the correct value, whereas the fit to B, in fig. 63b, fits the right value just within 1σ. The poor fits with the SubInner reconstructed events can be explained by the bias seen in fig. 54. The SubInner reconstruction is overestimating $|t|_{\text{SubIn}}$ for $|t|_{\text{true}} < 5 \cdot 10^{-4}\,\text{GeV}^2$, and since the theory is sensitive to changes of ρ in this $|t|$-range, it follows that the fit has trouble fitting ρ. B is fitted quite well as changes in B only affects the theory for $|t| > 2 \cdot 10^{-3}\,\text{GeV}^{-2}$, where the SubInner reconstruction method performs well. The theory is sensitive to changes in σ_{tot} for $|t| > 5 \cdot 10^{-4}\,\text{GeV}^2$, thus

the fit to σ_{tot} is only affected a bit by the bias of the SubInner reconstruction, though enough to be several σs from the true value.

In fig. 64 the fits of the three variables fitted with SubInner as the reconstruction method with the bias correction applied, are presented. By comparing the fits in fig. 63 and fig. 64 we see the effect of the bias correction. Looking at the fits of ρ, in fig. 63a and fig. 64a a huge improvement shows, as ρ is now fitted within 2σ of the true value. The fit to σ_{tot} also improves as it fits almost exactly to the correct value with the bias correction applied, seen in fig. 64b. The fit to B was already pretty good within one σ and this does not change when the bias correction is applied.

The bias corrected fits in fig. 62, done with HC and SubInner t-reconstruction combined, and in fig. 64, done only with SubInner t-reconstruction, is close to identical. This indicates that events reconstructed with the HC method could just as well have been estimated by the SubInner reconstruction method. Hence, even though the HC method is able to reconstruct to lower values of $|t|$ than the SubInner method, this does not improve the fits. It may be that the two methods is so similar because the points, estimated by SubInner in the combined method, is very crucial to the fits, thus dominating the events estimated by the HCs.

The best performing fits based on the parabolas presented in fig. 60, fig. 61, fig. 62, fig. 63, fig. 64, are the fits done with the t-reconstruction methods: HC and SubInner combined, HC and SubInner combined with bias correction, and the SubInner with bias correction. For further testing of the performance of these three fit procedures, all three parameters are fitted at once with the `minuit` minimizer. Fitting all three parameters at once means that the correlations of the fit parameters are also taken into account. This is done on the original MC data sample and on 9 new MC data samples made by bootstrapping the original MC data sample, by reweighting the events with a random Poisson PMF with $\mu = 1$. These fits are made in order to see how the fit results differs as the data fluctuates. The fit results are presented in fig. 65,

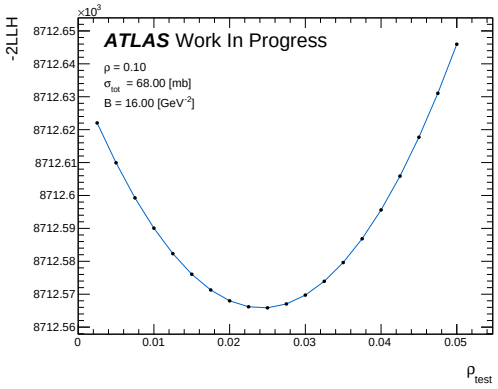

(a) -2LLH as function of ρ.

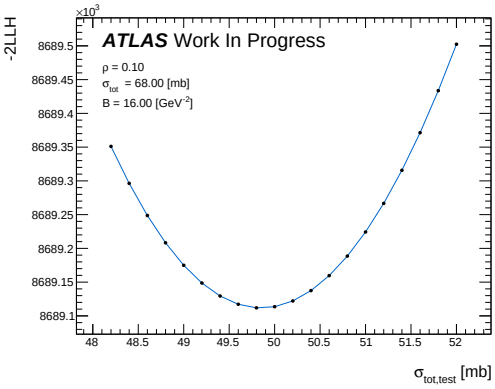

(b) -2LLH as function of σ_{tot}.

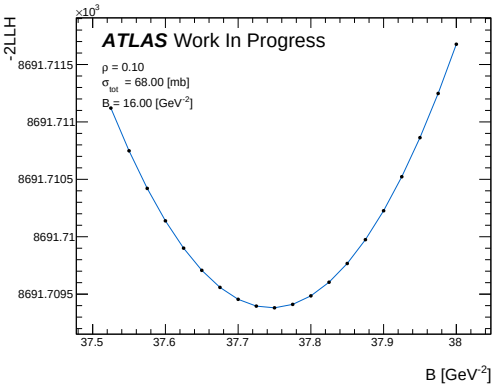

(c) -2LLH as function of B.

Figure 60: -2LLH as function of the three parameters ρ, σ_{tot}, B. The HC method is used for t-reconstruction with the bias correction not applied. In these fits events missed by the HC reconstruction are neglected. While varying one parameter the other two parameters are fixed to the true values. The events missed by the HC reconstruction method is left out. The true values of parameters is given on the plots.

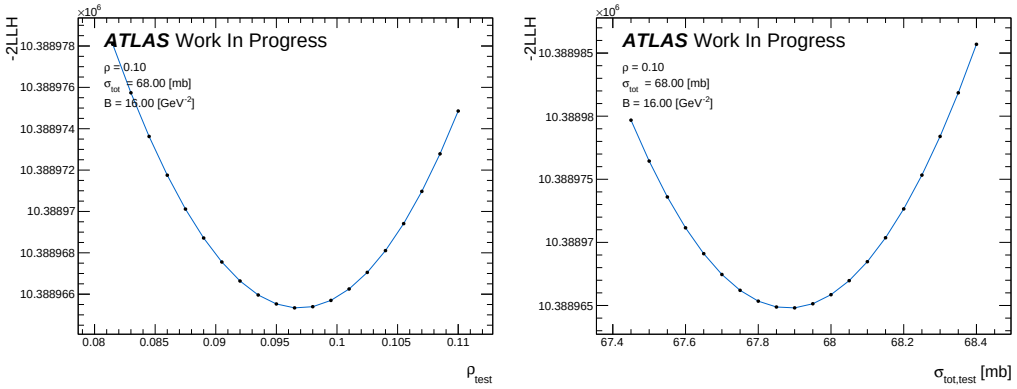

(a) -2LLH as function of ρ.

(b) -2LLH as function of σ_{tot}.

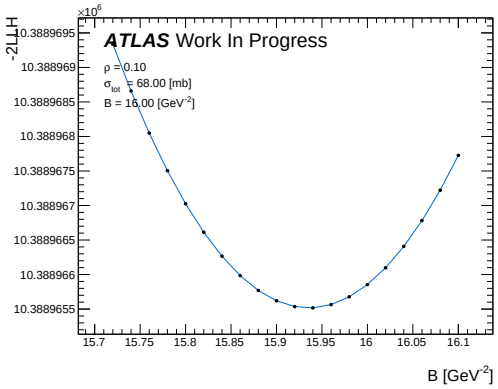

(c) -2LLH as function of B.

Figure 61: -2LLH as function of the three parameters ρ, σ_{tot}, B. The HC method in combination with SubInner is used for t-reconstruction with no bias correction applied. While varying one parameter the other two parameters are fixed to the true values. The true values of parameters is given on the plots.

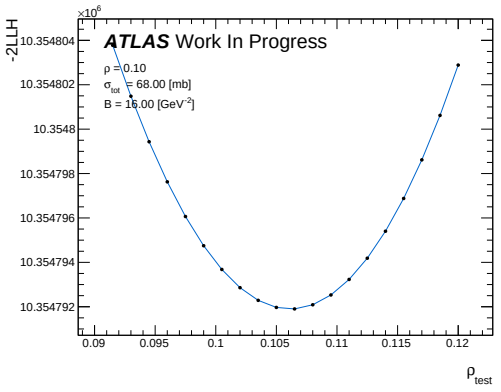

(a) -2LLH as function of ρ.

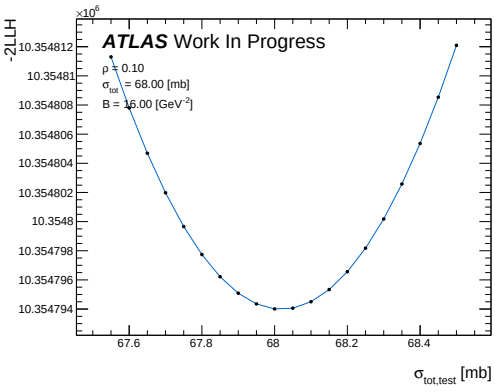

(b) -2LLH as function of σ_{tot}.

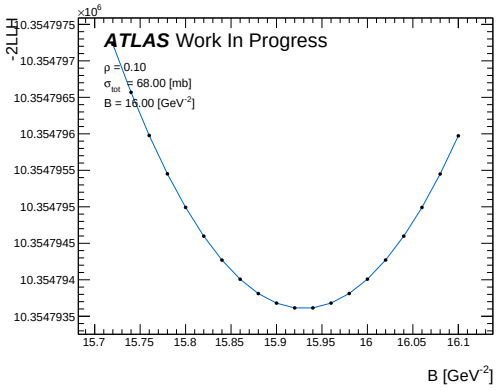

(c) -LLH as function of B.

Figure 62: -2LLH as function of the three parameters ρ, σ_{tot}, B. HC method in combination with SubInner is used for t-reconstruction with no bias correction applied. While varying one parameter the other two parameters are fixed to the true values. The true values of parameters is given on the plots.

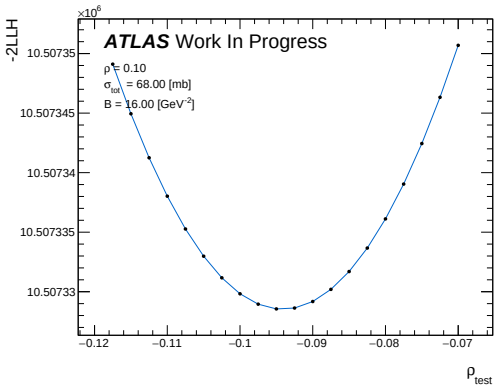

(a) -2LLH as function of ρ.

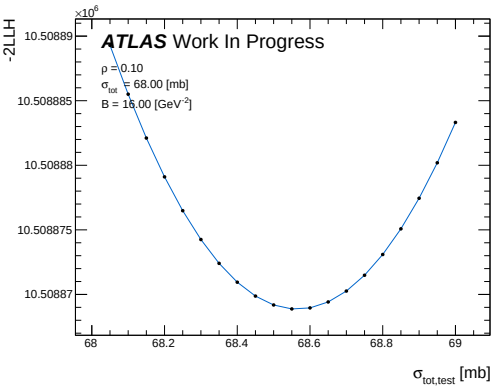

(b) -2LLH as function of σ_{tot}.

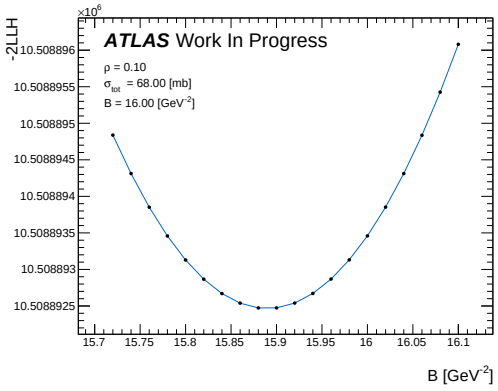

(c) -2LLH as function of B.

Figure 63: -2LLH as function of the three parameters ρ, σ_{tot}, B. The SubInner method is used for t-reconstruction with no bias correction applied. While varying one parameter the other two parameters are fixed to the true values. The true values of parameters is given on the plots.

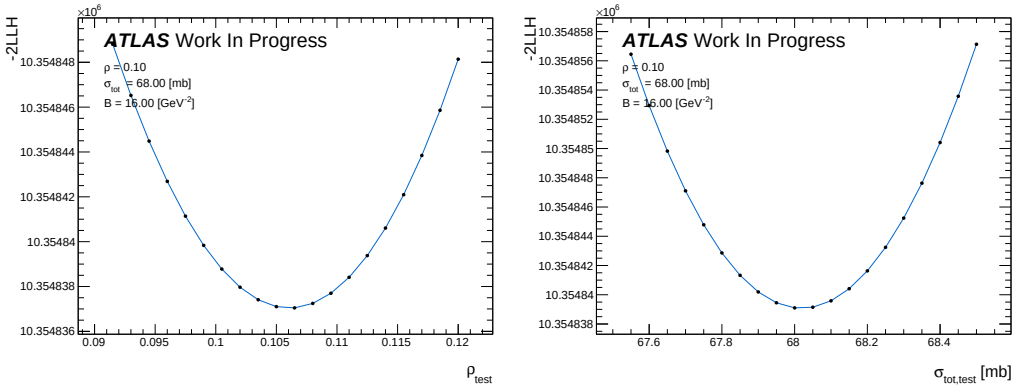

(a) -2LLH as function of ρ.

(b) 2LLH as function of σ_{tot}.

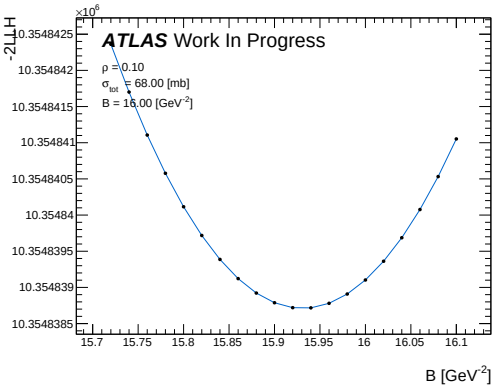

(c) -2LLH as function of B.

Figure 64: -2LLH as function of the three parameters ρ, σ_{tot}, B. SubInner is used for t-reconstruction with the bias correction applied. While varying one parameter the other two parameters are fixed to the values at which the MC data sample is generated. The true values of parameters is given on the plots.

fig. 66, and fig. 67, for the HC and SubInner t-reconstruction method combined without bias correction, the HC and SubInner t-reconstruction method combined with bias correction, and the SubInner reconstruction method with bias correction, respectively.

The fit using the HC and SubInner method combined, without the bias correction, has a tendency to underestimate all of the fit parameters, as the average value of the fit results for all three parameters are several standard deviations below the true value.

The other two reconstruction methods with the bias correction applied, both show improved results, and the two methods have almost the same outcome. There is a small tendency to overestimate ρ with a value of $\rho = 0.1063$ and $\sigma_\rho = 0.0042$, even though the mean of the fits still lies within two standard deviations of the true value. For both reconstruction methods the mean of the fit results of σ_{tot} and B fits almost exactly the true values.

The correlations between the fit parameters, when fitting all three parameters at a time, might affect the fit results. An average of the correlations of the three parameters are presented in table 5, where we see that the three parameters are correlated. σ_{tot} and B are the most correlated parameters, which makes sense as they are sensitive to events in the same $|t|$-range. Looking at fig. 68, where ρ is fitted independently, it is still overestimated, which could mean that the error of the ρ-fit is not due to the correlations between the parameters.

The deviation of the fitted ρ values are tested further by fitting ρ in 11 single parameter fits, with fixed $\sigma_{\text{tot}} = 68\,\text{mb}$ and $B = 16\,\text{GeV}^{-2}$. The first test is done by fitting using the true values of $|t|$ of the MC data sets. This is compared to single parameter fits of ρ using the SubInner t-reconstruction method and the bias correction. The results are presented in fig. 68 where we see very similar results for the fits using $|t|_{\text{true}}$ and $|t|_{\text{SubIn}}$. This tells us that the SubInner with bias correction fit is performing very well, and that the offset is not due to poor reconstruction of $|t|$ or an inefficient bias correction.

The inadequacy of the ρ fits may arise from the acceptance of the ALFA

Fit routine	$\rho_{\rho,\sigma_{\mathrm{tot}}}$	$\rho_{\rho,B}$	$\rho_{\sigma_{\mathrm{tot}},B}$
HC+SubInner, no BC	0.43	0.62	0.80
SubInner, with BC	0.42	0.62	0.80

Table 5: The average correlations of the fit parameters of the 10 fits presented in fig. 66, and fig. 67, with $\rho_{X,Y}$ being the correlation coefficient between the parameters X and Y. The error on the correlation coefficients are negligible.

detectors and the MC sample not being generated for small enough values of $|t|$. Due to the divergence, some protons, with very small scattering angles, are not expected to be observed in ALFA, but end up in the detectors anyway, while some events that are expected to be seen do not hit the detectors. Thus, some of the events with $|t| < 4 \cdot 10^{-5}\,\mathrm{GeV}^2$, that could have been observed in the detectors due to the divergence, are not seen as the MC sample are generated in the range of $4 \cdot 10^{-5}\,\mathrm{GeV}^2 \leq |t| \leq 6 \cdot 10^{-2}\,\mathrm{GeV}^2$. This results in a deficit of events in the low $|t|$-range, where ρ is sensitive. These events would have contributed a lot to the value of the LLH as they correspond to very large values of $d\sigma$, and as they are not seen in the detectors the fit to ρ is penalized. This can possibly be made up for by expanding the $|t|$-range of the MC simulation.

Using the maximum log-likelihood fit routine to fit events, which are not run through the detector and therefore not subject to the acceptance of ALFA, with an MC sample created in the same way, yields a fit result of ρ well within 1σ of the true value. This indicates, that the offset in ρ could be due to the acceptance of ALFA, as the fit routine works well when the events of the MC samples are not dependent of the acceptance.

It can, however, be inferred that the SubInner reconstruction method with the bias correction is performing very well, as the fits in fig. 68b shows close to identical results as to the fits done with $|t|_{\mathrm{true}}$.

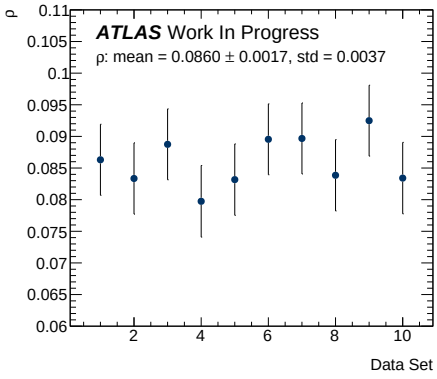

(a) ρ.

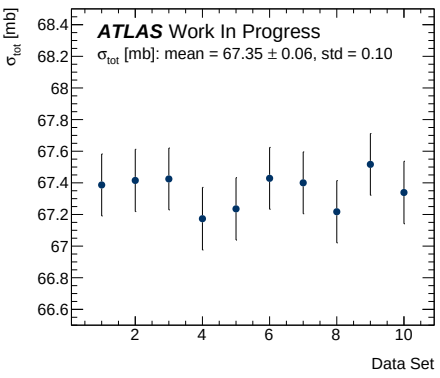

(b) σ_{tot}.

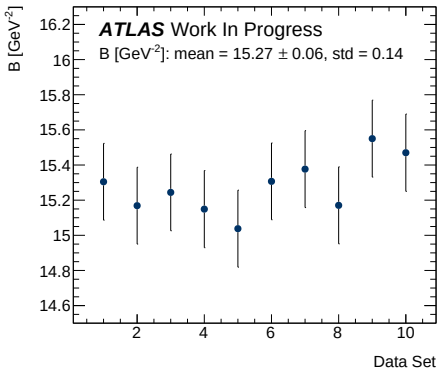

(c) B.

Figure 65: Fit results for the 10 MC data samples, fitted with the combined HC and SubInner t-reconstruction. On the x-axis is Data Set number, where the original MC data sample is number 1 and the rest are the samples made from bootstrapping. The mean and standard deviation (std) of the 10 fit results are printed on the plots. The true values of the MC data sample are: $\rho = 0.1$, $\sigma_{\mathrm{tot}} = 68\,\mathrm{mb}$, $B = 16\,\mathrm{GeV}^{-2}$.

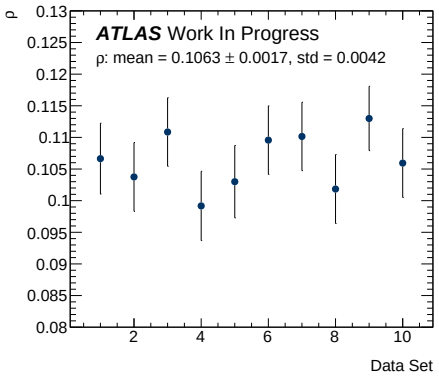

(a) ρ.

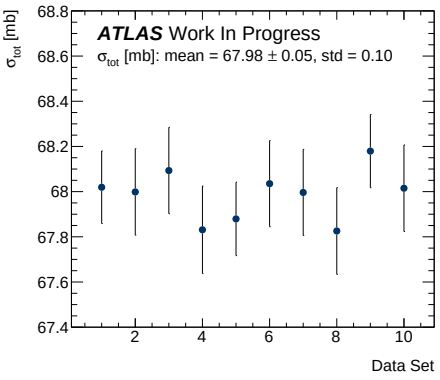

(b) σ_{tot}.

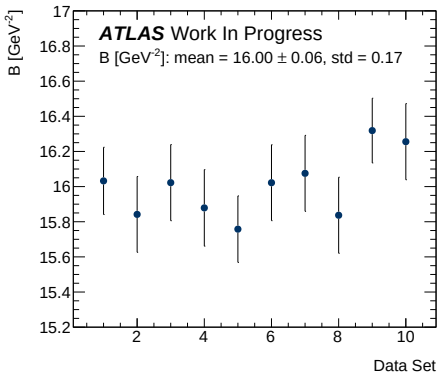

(c) B.

Figure 66: Fit results for the 10 MC data samples fitted with the combined HC and SubInner t-reconstruction and bias correction applied. On the x-axis is Data Set number, where the original MC data sample is number 1 and the rest are the samples made from bootstrapping. The mean and standard deviation (std) of the 10 fit results are printed on the plots. The true values of the MC data sample are: $\rho = 0.1$, $\sigma_{\mathrm{tot}} = 68\,\mathrm{mb}$, $B = 16\,\mathrm{GeV}^{-2}$.

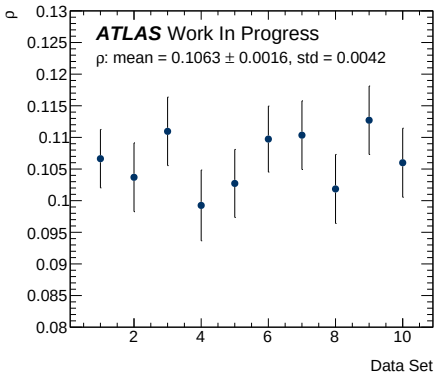

(a) ρ.

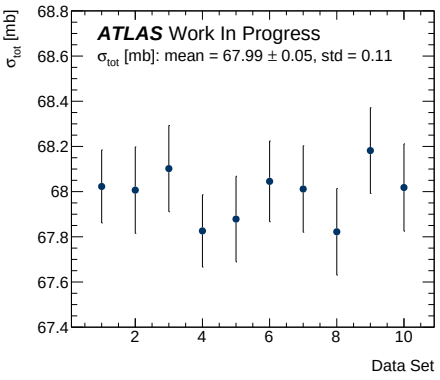

(b) σ_{tot}.

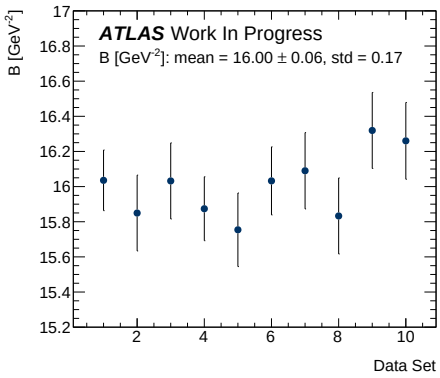

(c) B.

Figure 67: Fit results for the 10 MC data samples fitted with SubInner t-reconstruction and bias correction applied. On the x-axis is Data Set number, where the original MC data sample is number 1 and the rest are the samples made from bootstrapping. The mean and standard deviation (std) of the 10 fit results are printed on the plots. The true values of the MC data sample are: $\rho = 0.1$, $\sigma_{\mathrm{tot}} = 68\,\mathrm{mb}$, $B = 16\,\mathrm{GeV}^{-2}$.

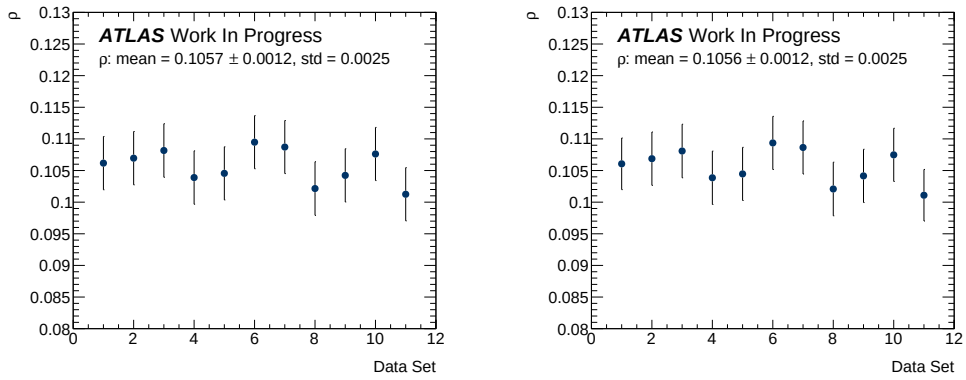

(a) $|t|_{\text{true}}$. (b) SubInner and BC.

Figure 68: Fit results for 11 MC data samples fitted with (a) $|t|_{true}$ and (b) SubInner t-reconstruction and bias correction applied. On the x-axis is Data Set number, where the original MC data sample is number 1 and the rest are the samples made from bootstrapping. The mean and standard deviation (std) of the 11 fit results are printed on the plots. The true values of the MC data sample are: $\rho = 0.1$.

4 Discussion

The primary focus of the thesis has been on developing a MC simulation for ALFA, and to study the 900 GeV elastic signal generated with the MC simulation. The simulated elastic signal has been studied through the elastic correlation distributions, where the affect of the beam spot width, divergence, detectors smearing, and transport matrices, was analysed. Then followed a test of the t-reconstruction methods together the development and testing of the new HC reconstruction method. At last a new fit routine was developed using the reconstructed t-values to fit a MC data sample.

Elastic Selection

For the elastic selection cuts a new fitting function with two ellipses instead of one was used to fit the elastic correlation distributions. Looking at these fits it is clear that adding another ellipse does not help saving a lot of events that would have otherwise been discarded, as the width of the two ellipses often are very similar. However, fitting with two ellipses discloses information about the optics of ALFA and in the future the elastic selection fits could be used to determine the values of the transport matrix elements. The widths of the ellipsis of the fitted $x^A_{i/o}$ vs. $x^C_{i/o}$ and $x_i^{A/C}$ vs. $\theta_x^{A/C}$ distributions could in the future be used to determine the beam spot width., while the width of the $y^A_{i/o} vs. y^C_{i/o}$ could help determine the divergence. A lot of other combinations of elastic selection distributions could be studied to get an even more thorough understanding of the data.

Background

For now no background simulation has been made for the 900 GeV elastic run. Hence, a model of both the single diffractive background events and the DPE background events will have to be developed in order to get a real sense of how it influences the signal at 900 GeV, and how it affects the reconstruction efficiency and fit performance.

t-reconstruction

For this thesis the HC reconstruction method was developed. The HC reconstruction is a very cumbersome way to estimate t for data events, as each data point has to calculate the distance weights to the surrounding MC points, and this takes a long time. Unfortunately the HC reconstruction does not provide an improved t-reconstruction techniques, however there is room for improvement. First and foremost stratified sampling should be used in order for the HC reconstruction to be able to estimate t for all events. The stratified sampling could also make sure to generate MC points closer to the data points than what is currently done and by then enhancing the reconstruction resolution. Another thing that may improve the HC reconstruction is to do the estimation with more MC events, although this would increase the, already long, run time of the reconstruction algorithm. If the HC reconstruction cannot be improved, one should just use the SubInner reconstruction method as this performed just as well as the HC reconstruction, and it is a lot faster and more simple to use.

Fits

In the end the best performing fits were the ones done with the HC and the SubInner reconstruction combined with the bias correction applied, and the fits done with only SubInner t-reconstruction also with bias correction. The fitting tests showed the importance of the bias correction, so this is certainly a feature that should be kept for future analysis.

The advantage of the SubInner reconstruction method is that it is a fast way to estimate t, whereas the HC reconstruction is very slow and cumbersome. By now the SubInner t-reconstruction, with bias correction, achieves fit results which are as good as the fits done with the true values of $|t|$, which is close to optimal. Thus, as the SubInner reconstruction method has the advantage of being very fast and easy to use, it should be used for further analysis unless the HC reconstruction method is improved a lot.

The fits with the bias correction has a tendency to fit ρ to a slightly larger

value than the true value. When fitting with the $|t|_{\text{true}}$ values of the events, the offsets in the ρ-fits are still present, meaning that the offset cannot be due to the bias correction or t-reconstruction being inadequate. The reason for the offset in ρ might be due to the acceptance of ALFA and the fact that the MC samples are not generated at small enough $|t|$-values. This means that some events at very low $|t|$, which has the possibility of ending up in the detector, are not generated, resulting in a deficit of events in the low $|t|$-range where ρ is sensitive. This may be tested by fitting an MC data sample generated for a $|t|$-range going well below $4 \cdot 10^{-5}\,\text{GeV}$.

5 Conclusion

This thesis presents a thorough study of the simulation of the ALFA experiment conducted at an center-of-mass energy of 900 GeV and $\beta^* = 100\,\text{m}$. The main focus has been on understanding how the elastic signal is affected by the various aspects of the ALFA experiment, and to build a data analysis software to analyse the elastic signal from ALFA in the best way possible.

The elastic signal was studied with the elastic correlation distributions, which are mostly diagonal due to the symmetric nature of elastic scattering. In that signal was however seen another perpendicular signal, which is likely due to the width of the beam spot. Both signals were fitted with ellipses, and this fit routine could possibly be used for future estimation of the beam spot width and detector optics, by fitting real data. It was seen that the smearing of the signal in the vertical direction is mostly due to the divergence. Hence, measuring the width of the real data signal in y, could help estimate the divergence. The resolution of the detectors only has a noticeable smearing effect for the distributions of the local angle in y because of the large resolution of the outer detectors. The resolution of an armlet is measured to be 100 µm and a plausible reason is that multiple scattering of the protons in the inner detectors results in poor resolutions in the outer detectors.

It can be concluded that the Hyper Cube estimation method still needs improvement. By now it is not able to estimate all events, and therefore the SubInner method is used for the events the HC method is not able to reconstruct. This should be fixed with stratified sampling. The SubInner reconstruction has a better resolution, but the HC estimation method shows promise when it comes to reconstructing events for $|t|$-values below the range of the SubInner technique. However, both the HC estimation and SubInner reconstruction has bias towards overestimating $|t|$ for low values of $|t|_{\text{true}}$, that has to be corrected for when fitting.

For this analysis a new maximum log-likelihood fit has been developed. The LLH fit shows promising results, when the bias is corrected for. Still, the fits are only tested on simulated data without background, thus further testing is needed. With the bias correction the combined method of HC estimation and SubInner reconstruction performs just as well as the SubInner does on its own. This could be due to the SubInner having a dominant effect in the combined method, or the reason could be that the HC estimation is on the same level as the SubInner reconstruction. If it is not possible to improve the HC estimation method by stratified sampling, the SubInner method should be preferred as it is much faster and easier to use.

When fitting an MC data distribution created at the values $\rho = 0.1$, $\sigma_{\text{tot}} = 68\,\text{mb}$, and $B = 16\,\text{GeV}^{-2}$, we are able to obtain a fit of $\rho = 0.1063 \pm 0.0042$, $\sigma_{\text{tot}} = 67.99 \pm 0.11\,\text{mb}$, and $B = 16.00 \pm 0.17\,\text{GeV}^{-2}$. As the offset of the ρ fits, is also seen when fitting with $|t|_{\text{true}}$, it might be due to the acceptance of ALFA, and that the MC samples used for this analysis is not generated at $|t|$ low enough for all measurable elastic events to be detected.

The performance of the fits using SubInner t-reconstruction and bias correction seems to be very promising moving forward, as the fits obtains nearly identical results as to the fits done with $|t|_{\text{true}}$.

Appendices

A Partial wave expansion

A wave function can be expanded in a series of Legendre polynomials, essentially splitting the wave into multiple waves of different total spin J [31].

$$A^F(s, \cos(\theta_s)) = \frac{\sqrt{s}}{\pi q_s} \sum_{J=0}^{\infty} (2J+1) P_J(\cos(\theta_s)) a_J^F(s) \tag{68}$$

Each partial wave has an amplitude that depends on J. These amplitudes are essential for calculating the transition amplitudes in scattering theory. Using Regge theory we are able to write the partial wave amplitudes as functions of the spin and mass of the reggeons [31].

B The Optical Theorem

The optical theorem is a theorem that relates the forward scattering amplitude of elastic scattered particles to the total cross section based on unity.

Given a trasition matrix S, taking an initial state i to a final state f, the sum of probabilities of going from the initial state to all possible final states should be unity. This is written as

$$\sum_f p_{i\to f} = \sum_f |\langle f|\, S\, |i\rangle|^2 = \sum_f \langle i|\, S^\dagger\, |f\rangle\, \langle f|\, S\, |i\rangle = \langle i|\, S^\dagger S\, |i\rangle = \mathbb{1} \tag{69}$$

We now write the scattering matrix as $S = 1 + iT$, with T being the transition matrix. Having a two body initial state with four momenta p_1 and p_2 and a final state with an arbitrary number of particles n, we can write:

$$\langle f|\, S\, |i\rangle = \langle p_1' p_2' ... p_n'|\, S\, |p_1 p_2\rangle \tag{70}$$

$$= \delta_{if} - i(2\pi)^4 \delta^4(P^f - P^i)\, \langle f|\, T\, |i\rangle \tag{71}$$

with $P^f = p_1' + p_2' + ... + p_n'$ and $P^i = p_1 + p_2$. The transition rate is then

$$R_{fi} = (2\pi)^4 \delta^4(P^f - P^i) |\langle f|\, T\, |i\rangle|^2 \tag{72}$$

and it relates to the total cross section as

$$\sigma_{12\to n} = \frac{1}{4|\mathbf{p}_1|\sqrt{s}} \sum_f R_{fi} \tag{73}$$

Here $|\mathbf{p}_1|$ is the three-momentum of the initial particle 1 in the center-of-mass frame.

As the scattering matrix is unitary it follows that

$$S^\dagger S = (1 - iT)^\dagger (1 - iT) = \mathbb{1} \tag{74}$$

$$\Rightarrow -i(T - T^\dagger) = T^\dagger T \tag{75}$$

Now we look at two states l and i and write

$$\langle l|\, T\, |i\rangle - \langle l|\, T^\dagger\, |i\rangle = \sum_f (2\pi)^4 \delta^4(P^f - P^i)\, \langle l|\, T^\dagger\, |f\rangle\, \langle f|\, T\, |i\rangle \tag{76}$$

Now we require $l = i$ we have

$$2\mathrm{Im}\, \langle i|\, T\, |i\rangle = (2\pi)^4 \delta^4(P^f - P^i) |\langle f|\, T\, |i\rangle|^2 \tag{77}$$

The right hand side in is exactly the transition rate, and $\mathrm{Im}\, \langle i|\, T\, |i\rangle$ corresponds to the imaginary part of the forward scattering amplitude in the limit where no momentum is exchanged. We are now able to relate the forward scattering amplitude to the total cross-section by combining eq. (72) and eq. (73) and eq. (77). [8]

$$\sigma_{\mathrm{tot}} = \frac{1}{4|\mathbf{p}_1|\sqrt{s}} \mathrm{Im}\, \langle i|\, T\, |i\rangle = \frac{1}{4|\mathbf{p}_1|\sqrt{s}} \mathrm{Im}(A(s, t=0)) \tag{78}$$

At last we introduce F such that

$$\frac{d\sigma}{dt} = |F|^2 \tag{79}$$

$$\sigma_{\mathrm{tot}} = 4\sqrt{\pi}\mathrm{Im}(F(t=0)) \tag{80}$$

Thus we have a relation relating the total cross section and the forward scattering amplitude. [10]

C Elastic Selection Fits

C.1 Selection Cuts for Arm 2 and the C-side

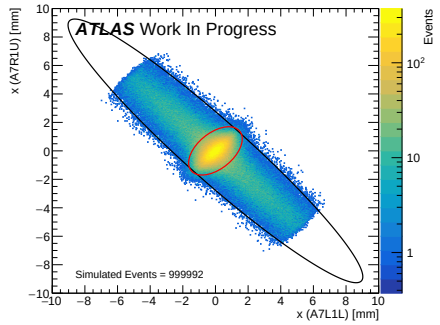

(a) x_i^A vs. x_i^C.

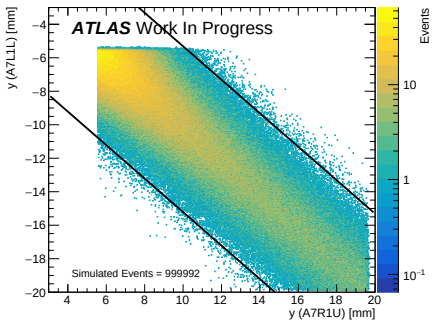

(b) y_i^A vs. y_i^C.

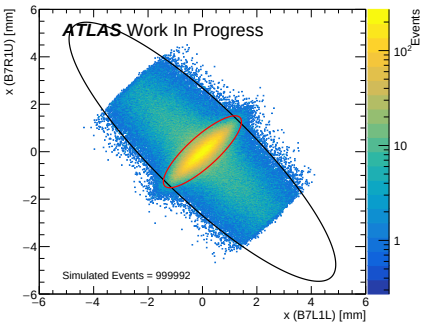

(c) x_o^A vs. x_o^C.

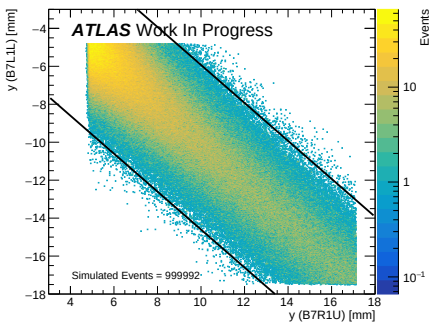

(d) y_o^A vs. y_o^C.

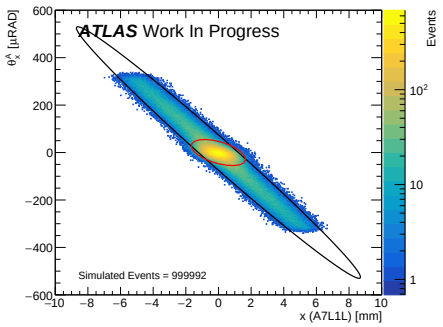

(e) x_i^A vs. θ_x^A.

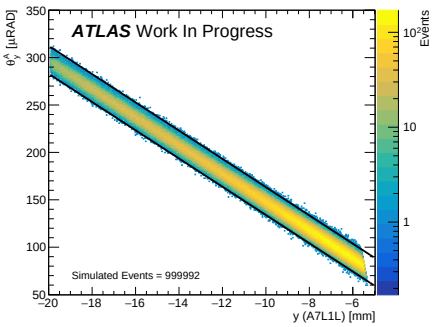

(f) y_i^A vs. θ_y^A.

Figure 69: Elastic selection correlation fits. The x-plots are fitted with a double ellipse. The y-plots are fitted with straight lines, and the width is fitted by projection the points to a plane, orthogonal to the line, and then fitted with a Gaussian. All plots are signal from arm 2.

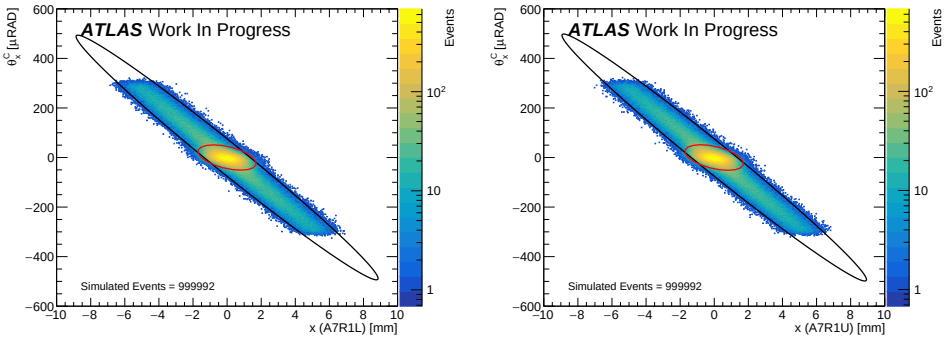

(a) x_i^C vs. θ_x^C of arm 1.

(b) x_i^C vs. θ_x^C of arm 2.

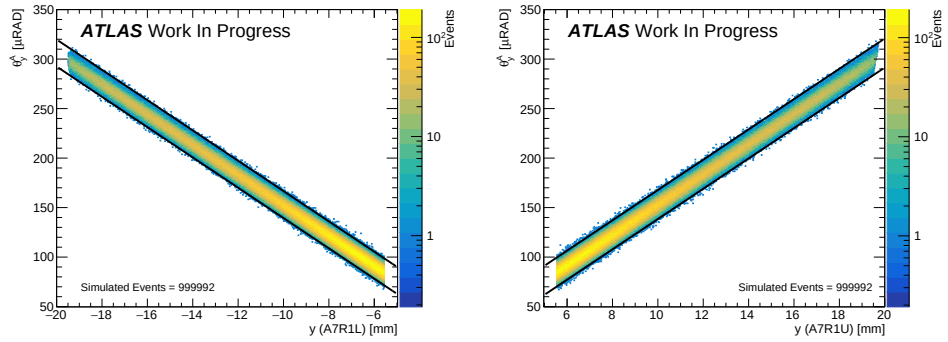

(c) y_i^C vs. θ_y^C of arm 1.

(d) y_i^C vs. θ_y^C of arm 2.

Figure 70: Elastic correlation selection fits of y_i^C vs. θ_y^C and y_i^C vs. θ_y^C in arm 1 and 2.

C.2 Elastic Selection Fits: BSW

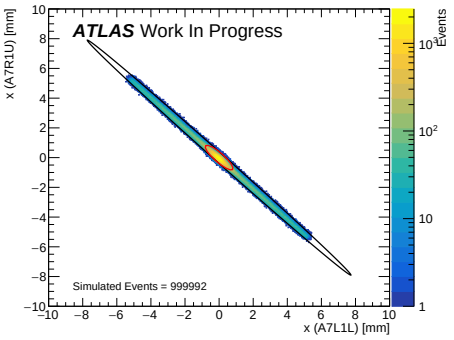

(a) No BSW.

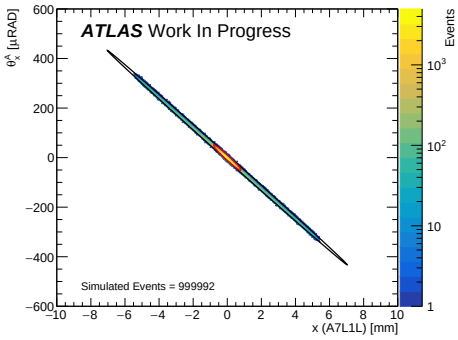

(b) No BSW.

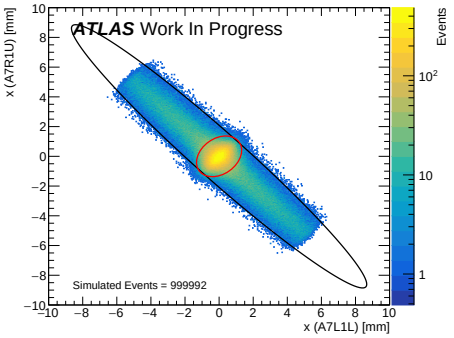

(c) 3/4 of nominal BSW.

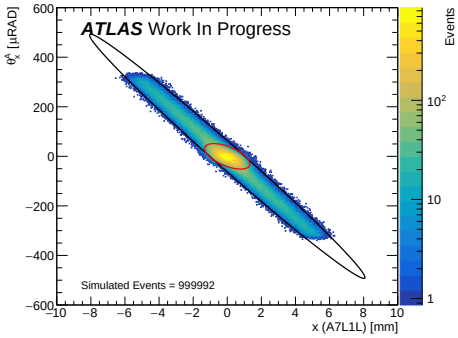

(d) 3/4 of nominal BSW.

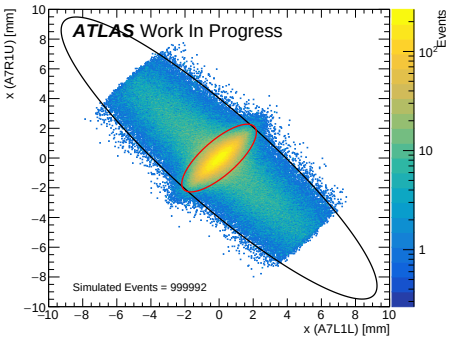

(e) 6/4 of nominal BSW.

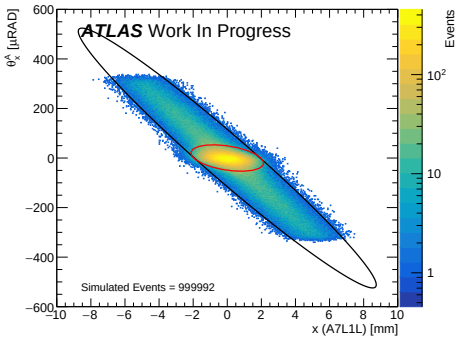

(f) 6/4 of nominal BSW.

Figure 71: Distributions of x_i^A vs. x_i^C and x_i^A vs. θ_x^A distribution of arm 2, plotted with varying the fractions of nominal beam spot width. With nominal divergence and detector smearing.

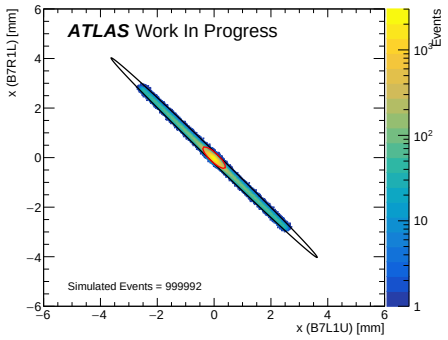

(a) Arm1: No BSW.

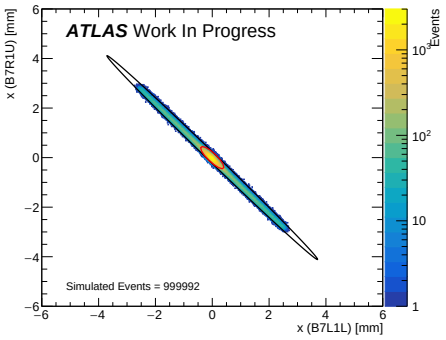

(b) Arm2: No BSW.

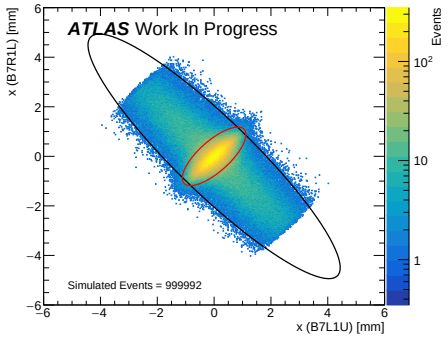

(c) Arm1: 3/4 of nominal BSW.

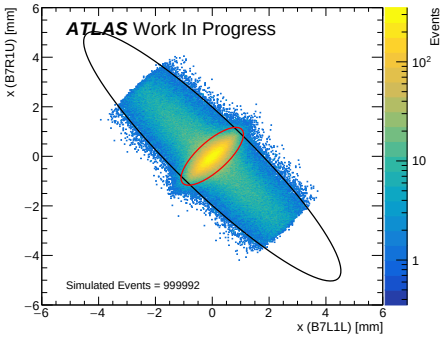

(d) Arm2: 3/4 of nominal BSW.

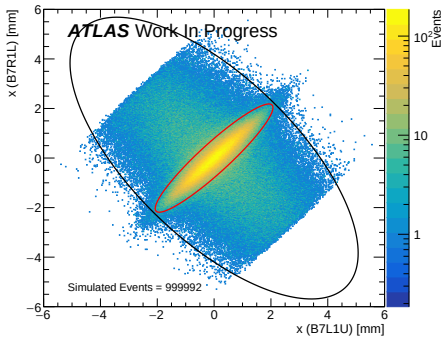

(e) Arm1: 6/4 of nominal BSW.

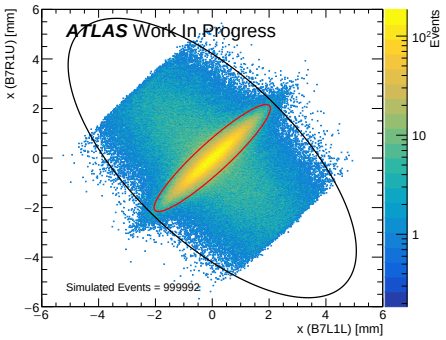

(f) Arm2: 6/4 of nominal BSW.

Figure 72: Distributions of x_o^A vs. x_o^C distribution of arm 1 and 2, plotted with varying the fractions of nominal beam spot width. With nominal divergence and detector smearing.

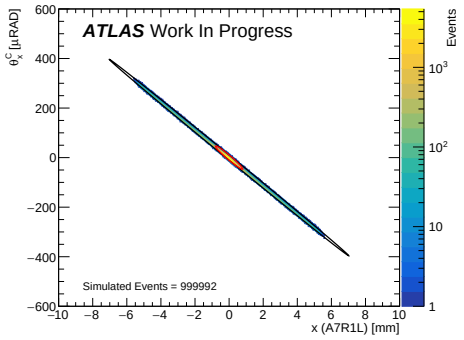

(a) Arm1: No BSW.

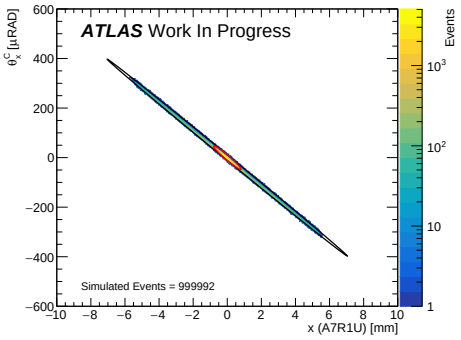

(b) Arm2: No BSW.

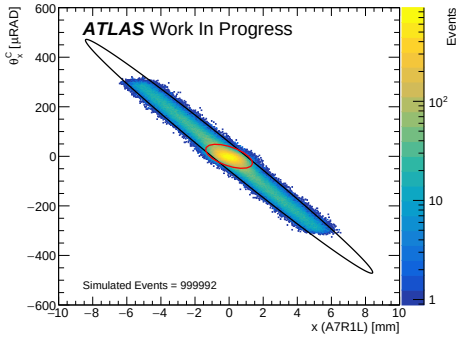

(c) Arm1: 3/4 of nominal BSW.

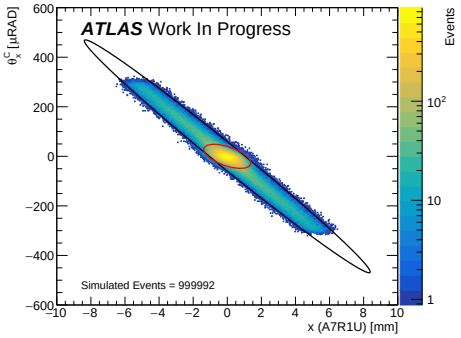

(d) Arm2: 3/4 of nominal BSW.

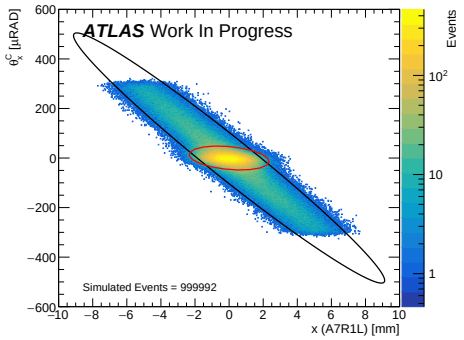

(e) Arm1: 6/4 of nominal BSW.

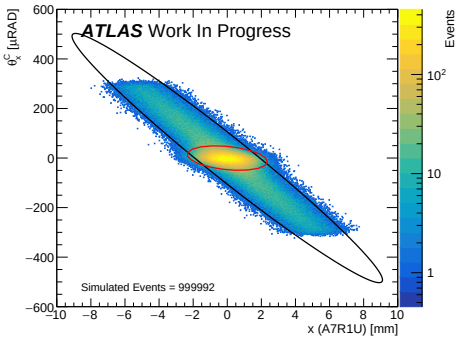

(f) Arm2: 6/4 of nominal BSW.

Figure 73: Distributions of x_i^C vs. θ_x^C distribution of arm 1 and 2, plotted with varying the fractions of nominal beam spot width. With nominal divergence and detector smearing.

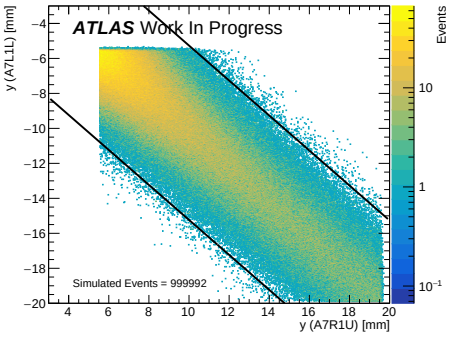

(a) y_i^A vs. y_i^C. 2/4 of nominal BSW.

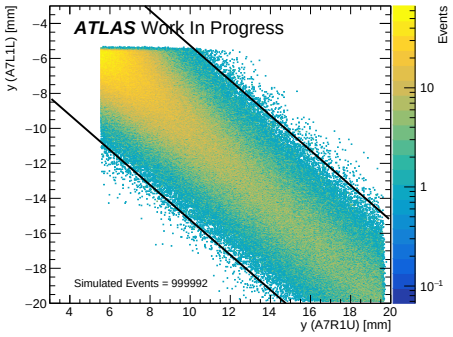

(b) y_i^A vs. y_i^C. 6/4 of nominal BSW.

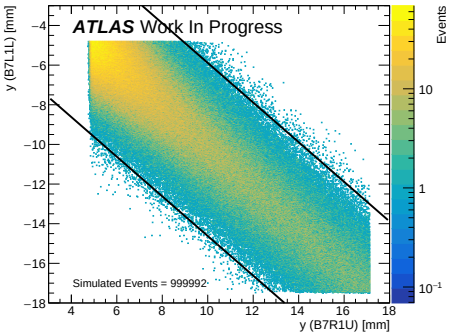

(c) y_o^A vs. y_o^C. 2/4 of nominal BSW.

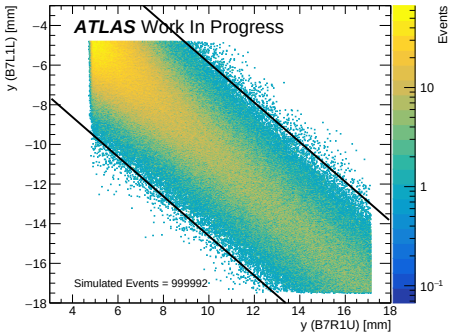

(d) y_o^A vs. y_o^C. 6/4 of nominal BSW.

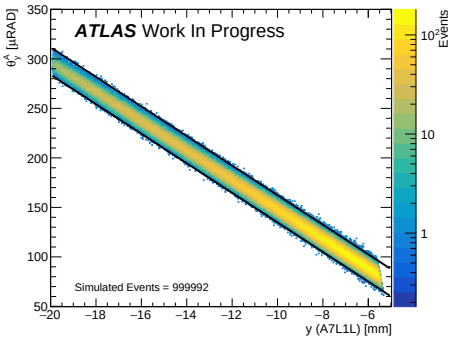

(e) y_i^A vs. θ_y^A. 2/4 of nominal BSW.

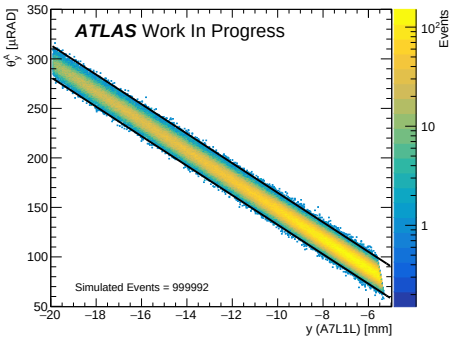

(f) y_i^A vs. θ_y^A. 6/4 of nominal BSW.

Figure 74: Distributions of y_i^A vs. y_i^C, y_o^A vs. y_o^C, and y_i^A vs. θ_y^A, with 2/4 and 6/4 of nominal beam spot width. With nominal divergence and detector smearing in all plots. All distributions are from arm 2

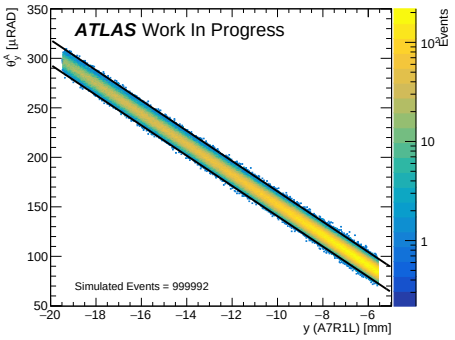

(a) y_i^C vs. θ_y^C of arm 1. 2/4 of nominal BSW.

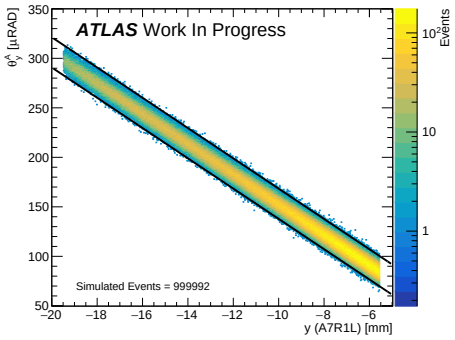

(b) y_i^C vs. θ_y^C of arm 1. 6/4 of nominal BSW.

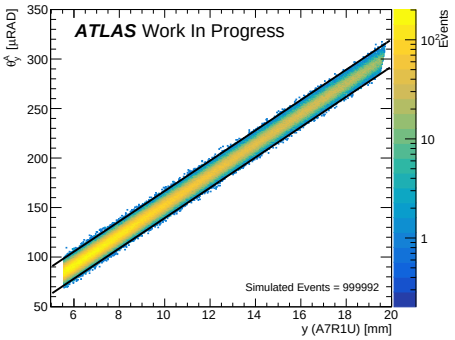

(c) y_i^C vs. θ_y^C of arm 2. 2/4 of nominal BSW.

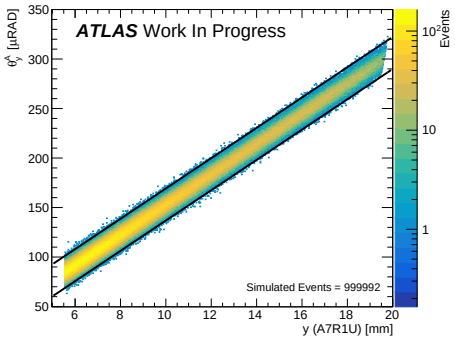

(d) y_i^C vs. θ_y^C of arm 2. 6/4 of nominal BSW.

Figure 75: Distributions of y_i^C vs. θ_y^C, with 2/4 and 6/4 of nominal beam spot width for arm 1 and 2. With nominal divergence and detector smearing in all plots

C.3 Elastic Selection Fits: Divergence

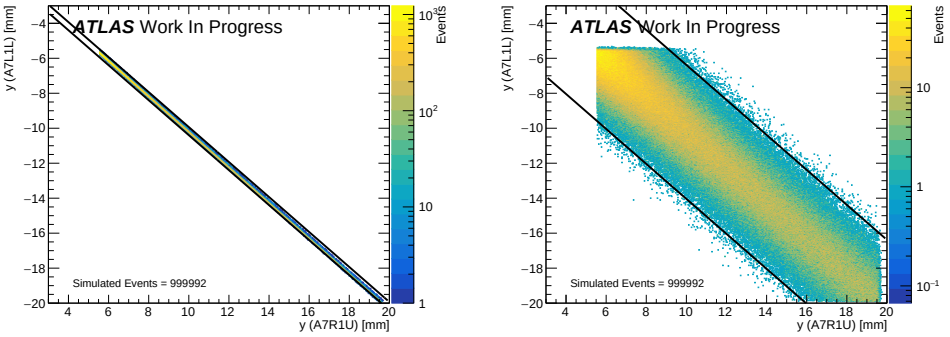

(a) No divergence.

(b) 3/4 div.

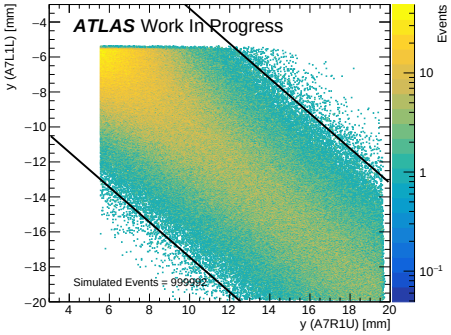

(c) 6/4 div.

Figure 76: Distributions of y_i^A vs. y_i^C with 2/4 and 6/4 of nominal beam spot width. With nominal divergence and detector smearing in all plots. All distributions are from arm 2

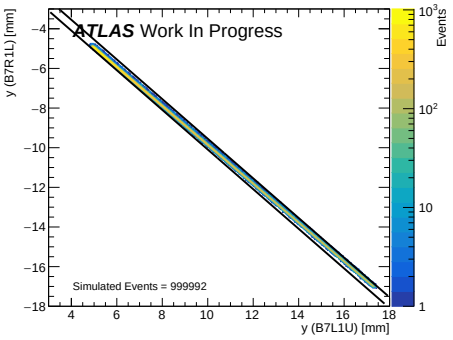

(a) Arm 1. No div.

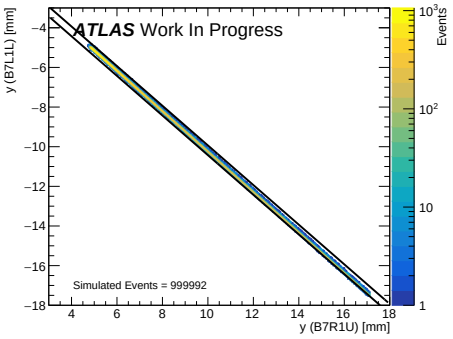

(b) Arm 2. No div.

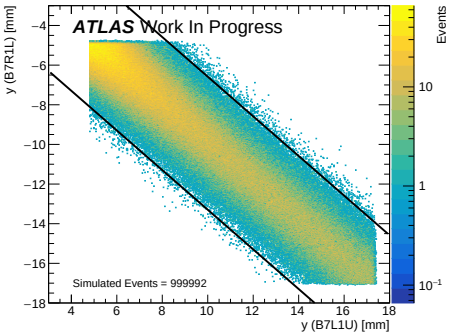

(c) Arm 1. 3/4 div.

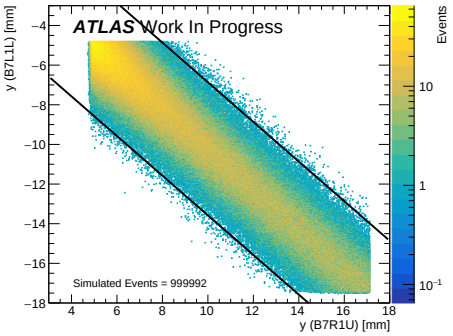

(d) Arm 2. 3/4 div.

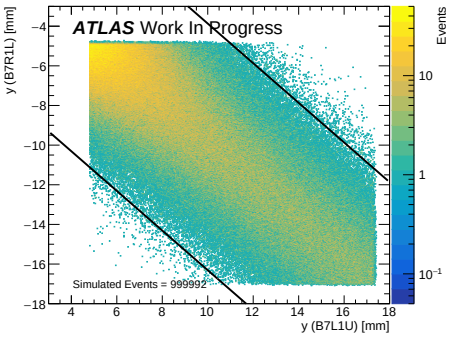

(e) Arm 1. 6/4 div.

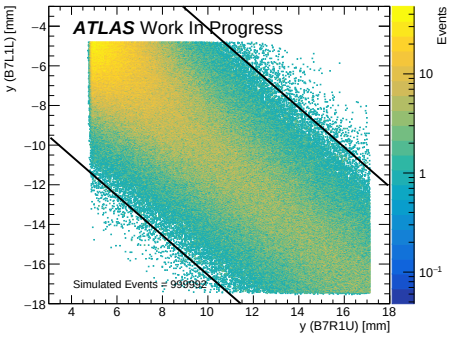

(f) Arm 2. 6/4 div.

Figure 77: Distributions in arm 1 and 2 of y_o^A vs. y_o^C with no divergence and with 2/4 and 6/4 of nominal divergence of arm 1 and 2. With nominal divergence and detector smearing in all plots.

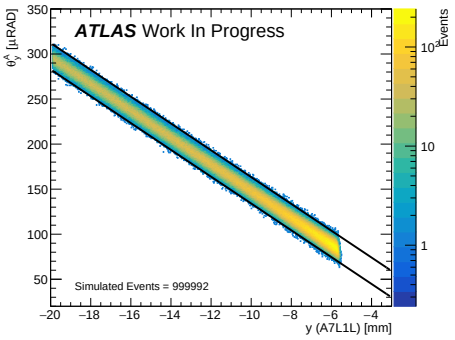

(a) A-side, arm 2. No div.

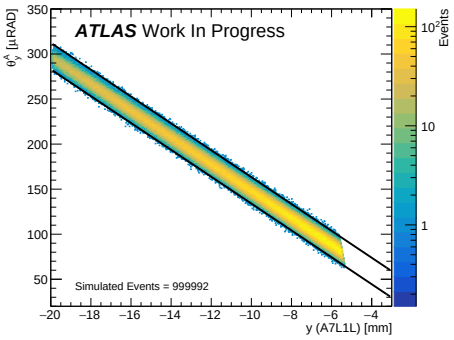

(b) A-side, arm 2. 6/4 div.

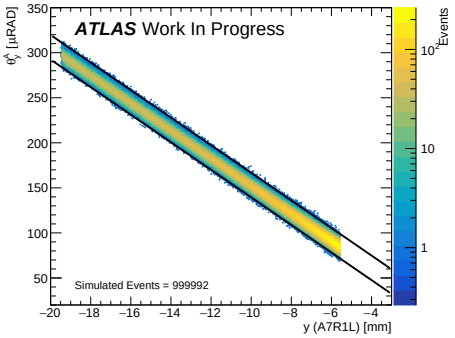

(c) C-side, arm 1. No div.

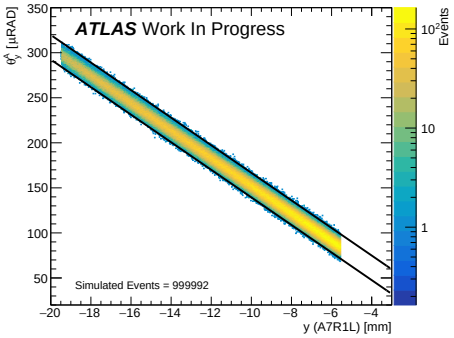

(d) C-Side, arm 1. 6/4 div.

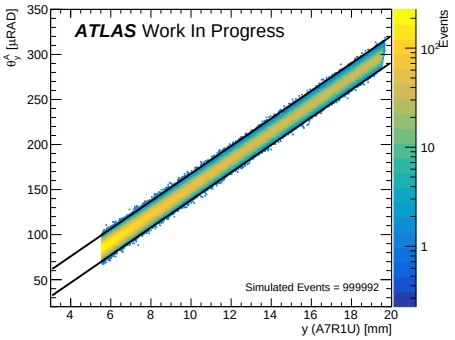

(e) C-side, arm 2. No div.

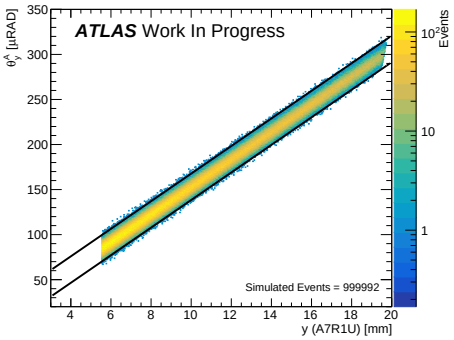

(f) C-Side, arm 2. 6/4 div.

Figure 78: Distributions in arm 1 and 2 of $y_i^{A/C}$ vs. $\theta_y^{A/C}$ with no divergence and with 6/4 of nominal divergence width of arm 1 and 2. With nominal divergence and detector smearing in all plots.

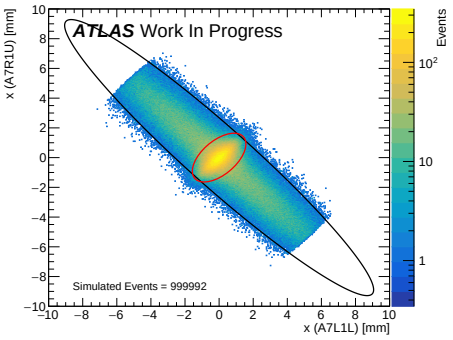

(a) Arm 2. No div.

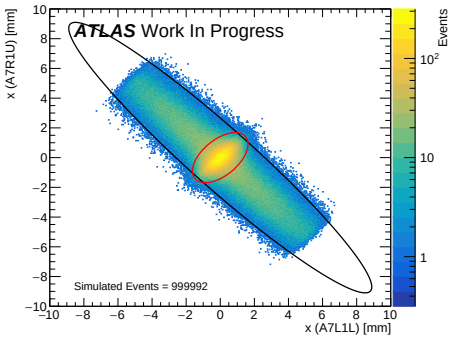

(b) Arm 2. 6/4 div.

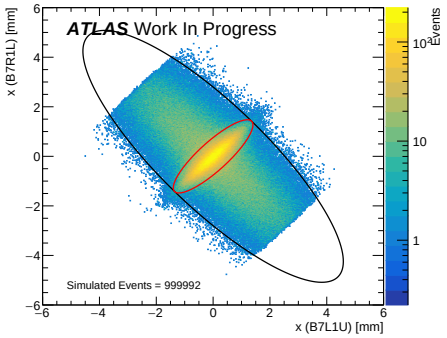

(c) Arm 1. No div.

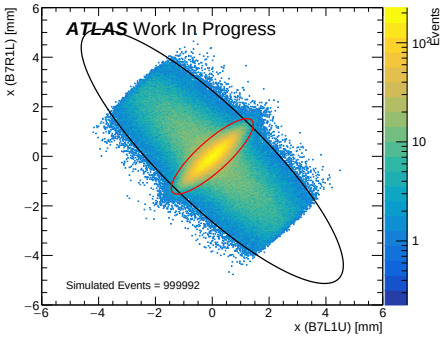

(d) Arm 1. 6/4 div.

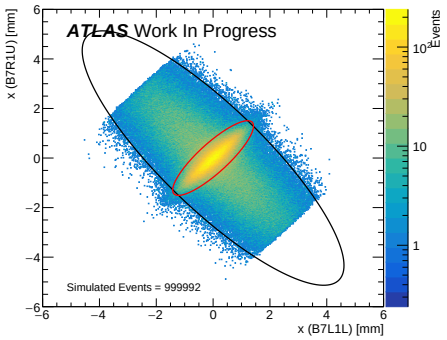

(e) Arm 2. No div.

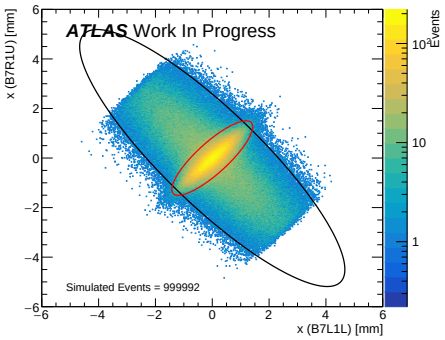

(f) Arm 2. 6/4 div.

Figure 79: Distributions in arm 1 and 2 of $x^A_{i/o}$ vs. $x^C_{i/o}$ with no divergence and with 6/4 of nominal divergence. With nominal divergence and detector smearing in all plots.

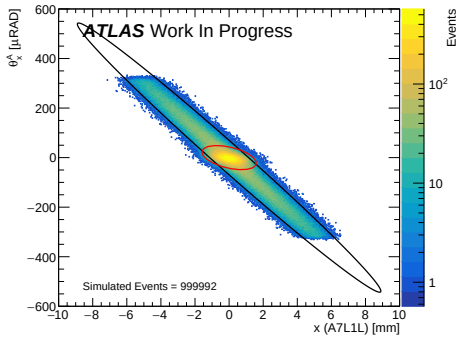

(a) A-side, arm 2. No div.

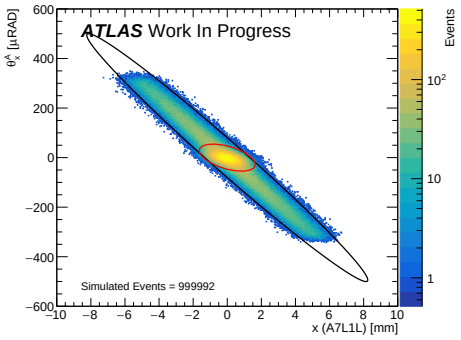

(b) A-side, arm 2. 6/4 div.

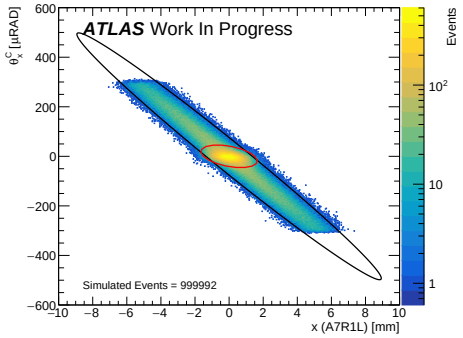

(c) C-side, arm 1. No div.

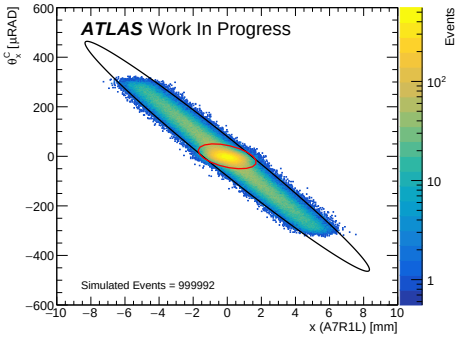

(d) C-Side, arm 1. 6/4 div.

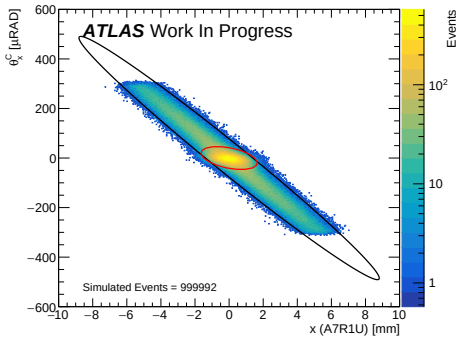

(e) C-side, arm 2. No div.

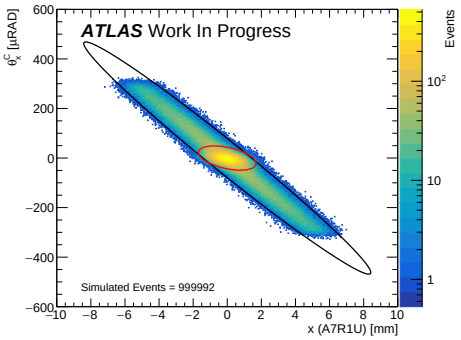

(f) C-Side, arm 2. 6/4 div.

Figure 80: Distributions of $x_i^{A/C}$ vs. $\theta_x^{A/C}$ with no divergence and with 6/4 of nominal divergence width of arm 1 and 2. With nominal divergence and detector smearing in all plots.

References

[1] Mark Thompson. *Modern Particle Physics*. Cambridge University Press, 2013.

[2] MJ Cush. Standard model of elementary particles. `https://commons.wikimedia.org/w/index.php?curid=4286964`. Accessed 27 June 2020.

[3] Alexandre Deur, Stanley J. Brodsky, and Guy F. de Teramond. The QCD Running Coupling. *Prog. Part. Nucl. Phys.*, 90:1–74, 2016.

[4] P. Achard et al. Measurement of the running of the electromagnetic coupling at large momentum-transfer at LEP. *Phys. Lett. B*, 623:26–36, 2005.

[5] Georges Aad et al. Measurement of the total cross section from elastic scattering in pp collisions at $\sqrt{s} = 7$ TeV with the ATLAS detector. *Nucl. Phys. B*, 889:486–548, 2014.

[6] Jens Lyng Petersen. Elementarpartikelfysik. Lecture Notes `https://www.nbi.ku.dk/bibliotek/noter-og-undervisningsmateriale-i-fysik/elementarpartikelfysik---forelaesningsnoter/ElementarpartikelFysik_Noter_Jens_Lyng_Petersen.pdf`. Accessed 1 July 2020.

[7] Martin Poghosyan. An introduction to regge field theory. Wilhelm und Else Heraeus Physics Summer School `https://indico.cern.ch/event/682912/contributions/2798633/attachments/1561845/2459257/Poghosyan.pdf`. Accessed 1 July 2020.

[8] Lauren Alexandra Tompkins. *A Measurement of the proton-proton inelastic scattering cross-section at $\sqrt{s}$ =7 TeV with the ATLAS detector at the LHC*. PhD thesis, UC, Berkeley, 2011.

[9] V. M. Abazov et al. Comparison of pp and $p\bar{p}$ differential elastic cross sections and observation of the exchange of a colorless C-odd gluonic compound. 12 2020.

[10] Martin M. Block. Hadronic forward scattering: Predictions for the Large Hadron Collider and cosmic rays. *Phys. Rept.*, 436:71–215, 2006.

[11] J.C. Bernauer et al. Electric and magnetic form factors of the proton. *Phys. Rev. C*, 90(1):015206, 2014.

[12] G. Antchev et al. Measurement of elastic pp scattering at $\sqrt{\mathrm{s}} = 8$ TeV in the Coulomb–nuclear interference region: determination of the ρ -parameter and the total cross-section. *Eur. Phys. J. C*, 76(12):661, 2016.

[13] O.V. Selyugin. Problems of determination of σ_{tot} at the LHC. In *15th conference on Elastic and Diffractive Scattering*, 10 2013.

[14] R. Cahn. Coulombic - Hadronic Interference in an Eikonal Model. *Z. Phys. C*, 15:253, 1982.

[15] P.A. Zyla et al. Review of Particle Physics. *PTEP*, 2020(8):083C01, 2020.

[16] ATLAS Collaboration. Measurement of the total cross section from elastic scattering in pp collisions at s=8 tev with the atlas detector. *Physics Letters B*, 761:158 – 178, 2016.

[17] Esma Mobs. The CERN accelerator complex. Complexe des accélérateurs du CERN. Jul 2016. General Photo.

[18] Lyndon R Evans. The Large Hadron Collider Project. (LHC-Project-Report-53. CERN-LHC-Project-Report-53):10 p, Sep 1996.

[19] Peter W. Rasmussen. Elastic pp Scattering at ALFA with $\sqrt{s} = 13$ TeV and $\beta^\star = 2.5$ km. Master thesis, University of Copenhagen, 2018.

[20] Peter Hansen. Particle detectors and accelerators. Lecture Notes (2. Edition), University of Copenhagen, September 28th, 2015.

[21] Ramon Cid Manzano Xabier Cid Vidal. LHC Parameters. URL: `http://lhc-closer.es/taking_a_closer_look_at_lhc/1.lhc_parameters`. Accessed: January 5th, 2021.

[22] Simon Holm Stark. *Study of forward elastic pp scattering at* $\sqrt{s} = 8$ *TeV with the ALFA detector*. PhD thesis, University of Copenhagen, Jan 2017. Presented 24 Feb 2017.

[23] Peter Jenni, Markus Nordberg, Marzio Nessi, and Kerstin Jon-And. *ATLAS Forward Detectors for Measurement of Elastic Scattering and Luminosity*. Technical Design Report ATLAS. CERN, Geneva, 2008.

[24] Jan de Boer. Forward Physics and Scintillating Fibre Trackers at the Large Hadron Collider. Master thesis, University of Copenhagen, 2020.

[25] The ATLAS Collaboration. The ATLAS experiment at the CERN large hadron collider. *Journal of Instrumentation*, 3(08):S08003–S08003, Aug 2008.

[26] ATLAS Collaboration. Measurement of beam background in special high-β^* LHC runs at $\sqrt{s} = 900$ GeV using the ATLAS–ALFA detectors. (ATL-FWD-PUB-2020-001), May 2020.

[27] Sune Jakobsen. *Commissioning of the Absolute Luminosity For ATLAS detector at the LHC*. PhD thesis, University of Copenhagen, Dec 2013. Presented 31 Jan 2014.

[28] Daniele Mirarchi. *Vol. 31 - Crystal Collimation for LHC. Crystal collimation for LHC*. PhD thesis, Aug 2015. Presented 18 Jun 2015.

[29] Maria Kuhn. Emittance Preservation at the LHC, Mar 2013. Presented 05 Apr 2013.

[30] CERN BE/ABP Accelerator Beam Physics Group. MAD - Methodical Accelerator Design. URL: `http://madx.web.cern.ch/madx/`. Accessed: January 14th, 2021.

[31] Giulia Pancheri and Y.N. Srivastava. Introduction to the physics of the total cross-section at LHC: A Review of Data and Models. *Eur. Phys. J. C*, 77(3):150, 2017.